2 Acquisition of seismic reflection data

W. Frei

Between 1986 and 1993 some 500 km of seismic reflection and refraction data have been acquired and (re-)processed by the National Research Program NRP 20. Table 2-1 lists the various projects and areas of activities in chronological order.

Table 2-1
Data Acquisiton list

Year	Working area	Profile (names) profile location	Recording time (seconds) (HR = High Resolution)	Source type E = Explosives V = Vibroseis® T = Thumper	Length (km)	Remarks/ Objectives/ Partners
1986	**Eastern Switzerland**	**Eastern Traverse**				
	Wildhaus – Val Madris	E1 or 86-NF-01	60	E & V	110	jointly with European
	Prättigau Valley	E7–E10	60	E	15	Geotraverse (EGT)
	Stein a. Rh.–Wildhaus	3 lines (E4–E6)	4	V	24	re-processing Swisspetrol data
1987	**Western Switzerland**	**Canton of Geneva**				
	2 shots fired into a spread extending SE-NW south of Geneva		60	E	15	with ECORS and SI de Genève
	Western Alps	**Western Traverse**				
	Zweisimmen – Grône	W1 or 87-NF-01	60	E & V	36	
	Val d'Anniviers	W2 or 87-NF-02	60	E & V	20	with CROP-Italia
	Stalden – Zermatt-Cervinia	W3 or 87-NF-03	60	E & V	37	with CROP-Italia
	Zermatt – S.Giacomo (I)	W4 or 87-NF-04	60	E & V	14	with CROP-Italia
	Savièse VS	ETH-Zürich line	4	E	2.9	
	Sanetsch VS	ETH-Zürich line	4	E	2.6	
	Arolla VS	ETH-Zürich line	4	E	2.5	
	Turtmann / Agarn VS	3 ETH-Zürich lines	HR 1	E & T	1	
	Central Swiss Alps					
	E – W refraction profiling	2 refraction lines	–	E	150	
	Plateau W-Switzerland					
	Biel – Zweisimmen	4 lines (W7 – W10)	4	V	82	re-processing Swisspetrol data
1988	**Southern Switzerland**	**Southern Traverse**				
	Val Calanca – Porlezza	S1 or 88-NF-01	60	E	50	with CROP-Italia
	Val Blenio	S2 or 88-NF-02	4 (V) / 60 (E)	E & V	6	
	Biasca – Lugano	S3 or 88-NF-03	60	E & V	37	
	Mte. Generoso – Seseglio	S4 or 88-NF-04	60	E & V	23	with CROP-Italia
	Valle Muggio – Balerna	S5 or 88-NF-05	60	V	12	
	Chiasso – Stabio	S6 or 88-NF-06	12	E & V	6	Swisspetrol participation
	Stabio	S7 or 88-NF-07	12	E & V	1.5	Swisspetrol participation
	Valle della Motta	ETH-Zürich line	HR 1	T	0.7 }	with Museo cantonale di storia
	Porza – Vezia	ETH-Zürich line	HR 1	T	0.8 }	naturale, Lugano
1989	**Western Switzerland**	**Canton of Neuchâtel**				
	Val de Travers	3 ETH Zürich lines	HR 1	E & T	1.5	
	Rhône Valley	**Canton of Valais**				
		Bramois	HR 1	E & T	3.2 }	with GEOTHERMOVAL:
		Saillon	HR 2	E & T	2.7 }	mapping depth of Quarternary
		Martigny	HR 2	E	3.1 }	fill of the Rhône Valley and
		St. Maurice	HR 1	E & T	1.1 }	delineation of the bedrock
		Evionnaz	HR 0.5	E	0.3 }	surface
1990	**Central/Southern Alps**	**Central Traverse**				
	Brünig Pass – Goms Valley	C1 or 90-NF-01	60	V & E	34	
	Goms – Lago Maggiore	C2 or 90-NF-02	60	V & E	47	
	Lago Maggiore – Tresa	C3 or 90-NF-03	60	E	19	
	Obwalden – Brünig Pass	90-TGK01 and Klein Melchtal	8	V	17	TGK exchange data
	Grisons, Eastern Alps	**Eastern Traverse**				
	Thusis – Flüela Pass	E2 west or 90-NF-04	60	E & V	32	
	Flüela – Scuol / V. Sinestra	E2 east or 90-NF-05	60	E	31	

Year	Region	Sub-region / Line			Source		Notes
	Western Alps	**Western Traverse**					
	Val d'Aosta-Martigny-Illiez	W5 or 90-NF-06		60	E & V	61	with CROP-Italia
	St. Maurice / Rhone Valley	W5 or 90-NF-07		2	V	1.5	with GEOTHERMOVAL
	Le Châble	4 HR lines		1	T & E	2	with GEOTHERMOVAL
1991	**Western Switzerland**	**Canton of Valais**					
	Vétroz	Rhône Valley cross line	HR	1	E	2.8	with GEOTHERMOVAL
	Val d'Illiez (VS)	W6 or PSBR8529		5	V	12	re-processing Swisspetrol data
	Southern Switzerland	**Canton of Ticino**					
	Campo Vallemaggia	2 lines	HR	1	T & E	1.2	
	Mendrisiotto	Seseglio – Ronago (I)	HR	1	T	2.0 ⎱	with Museo cantonale di
	Mendrisiotto	Pizzamiglio	HR	1	T	0.7 ⎰	storia naturale, Lugano
	Eastern Alps	**Eastern Traverse**					with Universities of Munich (D), Münster (D),Clausthal (D), and Leoben (A),
	Val d'Uina / Val Sinestra	E3 or 91-NF-01		12	E	12	
	Switzerland – Germany	Jura – Black Forest					with DEKORP (Universities of Munich, Münster, Clausthal, Karlsruhe)
	Olten – Dinkelberg	J1 or 91-NF-02		30	E	51	
1992	**Southern Switzerland**	**Canton of Ticino**					
	Magadino Plain	92-NF-01	HR	2	T & E	2.9 ⎱	with Museo cantonale di
	Mendrisiotto	Chiasso	HR	1	T	0.7 ⎰	storia naturale, Lugano
	Eastern Switzerland	**Upper Rhine Valley**					
		Chur	HR	1	E	0.8	
		Domat / Ems	HR	1	E & T	1.2	
		Bonaduz	HR	1	E	0.7	
1993	**Southern Switzerland**	**Canton of Ticino**					
	Mendrisiotto	Capolago	HR	1	T	1.0	with Museo cantonale di storia naturale, Lugano

The depth range to be investigated included deep crustal reflection profiling down to a Moho depth of almost 60 km on one hand, and, on the other hand, the detailed mapping of the upper 15 km of the near surface structures of the Alpine nappes. A compromise was found by collecting two independent data sets, one with vibrators and one with explosive charges as seismic sources. Continuous Vibroseis® profiling using a dense VP spacing of 40 m, i. e. half the group spacing (= 80 m), provided sufficient lateral and vertical resolution for the upper 15 km of the crust. A unusually long single 60 s sweep was used in order to overcome the technical difficulties resulting from the field systems' refusal to sum individual shorter sweeps when a critical number of parity errors, which were induced at the road crossings of the more than 26 km long cable, was reached. Tests conducted at the beginning of the programme show the data quality of a single 60 s sweep is at least equal to that of a vertical stack of four 20 s sweeps. The tests carried out involved the dual recording of a 9 km long segment of the Eastern Traverse, once recorded with a vertical stack four 20 s sweeps per VP and once with a single 60 s sweep.

For deeper penetration, explosive charges between of 50 and 300 kg were fired in 30–70 m deep boreholes at 4–5 km intervals. Although the average coverage thus obtained is only 1- to 4-fold, the explosives data set proves to be indispensible for mapping the deeper crustal features, since at most places the less powerful Vibroseis® reflection signals rarely contain any information for depths greater than 30 km.

Prior to 1989 uncorrelated and unsummed records were recorded. This enabled pre-correlation and pre-summation signal-to-noise (S/N) enhancement techniques to be applied in the processing center. The methods thus applied include Vibroseis whitening, pre-correlation AGC and diversity stacking. The availability of the new SERCEL368 field acquisition system in 1989, an instrument equipped with various noise suppression options, allowed the recording of correlated and vertically summed records. This resulted in a significant reduction in the number of field tapes to be processed.

Numerous logistical obstacles have to be overcome when recording seismic reflection data across mountainous areas in the Alps and along densely populated valleys. Within the valleys, source and receiver coupling conditions on unconsolidated Quaternary valley sediments and on cones of landslide debris degrade severely. The high ambient noise level makes recording at night time necessary when trafic intensity and industrial actvities are at a minimum. Although railway authorities and electric power companies went at great length and agreed to turn off some ot the power supply lines during the recording periods, the data quality was still detrimentally affected by power line interference in many localities. In the mountainuous regions, access with vehicles is limited such that helicopter assistance proved to be the most cost-effective

Table 2-2
NRP 20 General recording parameters

| Explosive sources	
Number of channels	240 – 480, symmetrical split spread
Spread length	19 – 48 km
Group spacing	80 – 100 m
Geophones / group	18 – 24
Group array	linear pattern, at regular intervals within the group spacing
Geophone type	10 Hz
Recording time	60 s
Sampling rate	4 ms
Charge size	50 – 300 kg (up to 2000 kg for refraction surveys)
Source spacing	4 – 5 km
Source depth	30 – 70 m
Nominal fold	1 – 4
Vibroseis®	
Number of channels	240, symmetrical split spread
Spread length	19.2 km
Group spacing	80 m
Geophones / group	18 – 24
Group array	linear pattern, at regular intervals within the group spacing
Geophone type	10 Hz
Number of vibrators	5 – 7
Weight per unit	16 tonnes
VP spacing	40 m
Sweep range	10 – 48 Hz
Sweep length	60 sec
Recording time	64 sec
Sampling rate	4 ms
Number of sweeps per VP	1 – 2
Nominal fold	2 x 120
Recording type	unsummed and uncorrelated (1986 – 1988), summed and correlated after 1988
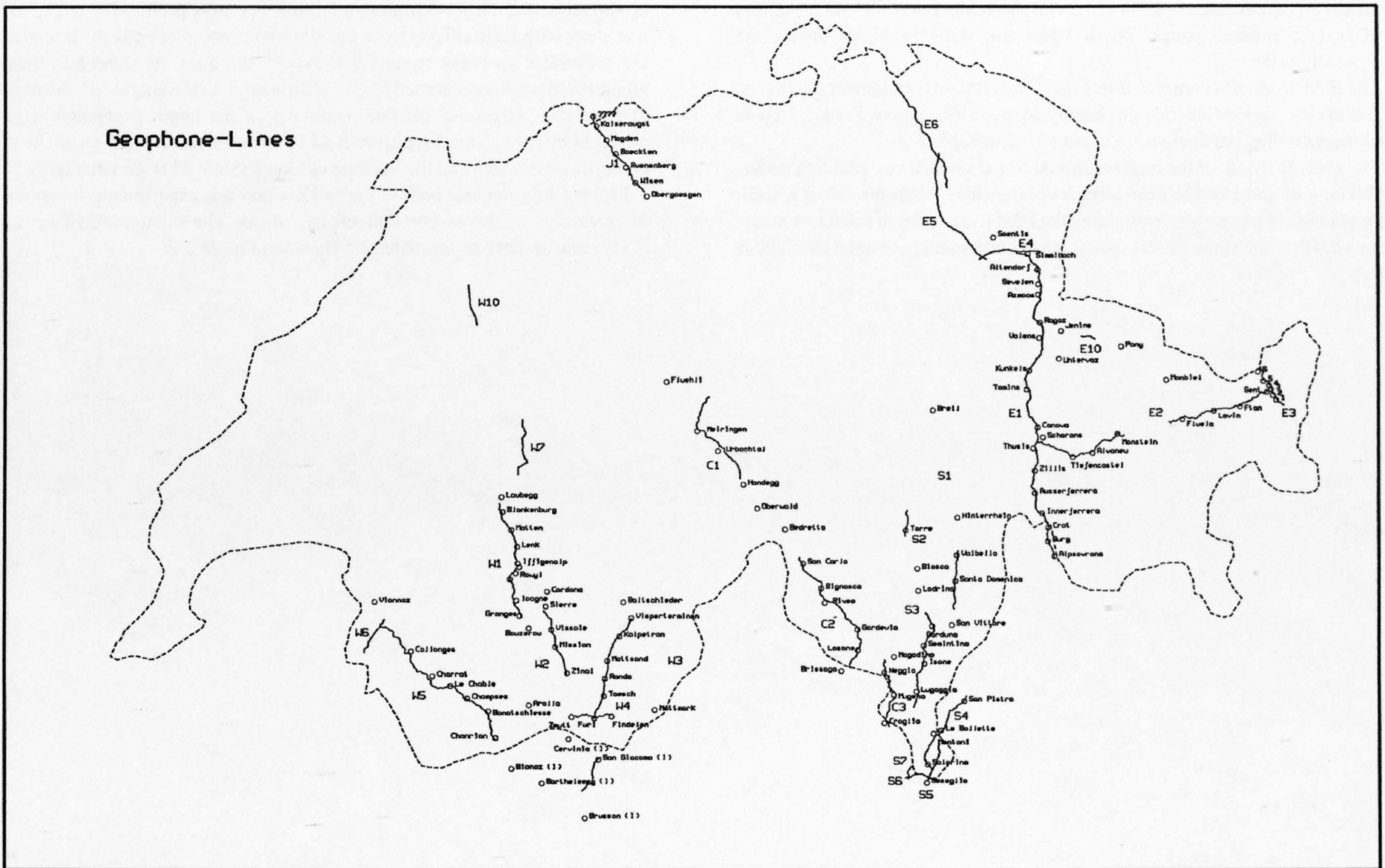
Figure 2-1
Geophone lines of the NRP 20 seismic lines (see also Figure 1-1). Localities indicated are in-line and off-line shot points of the explosion seismic experiments.
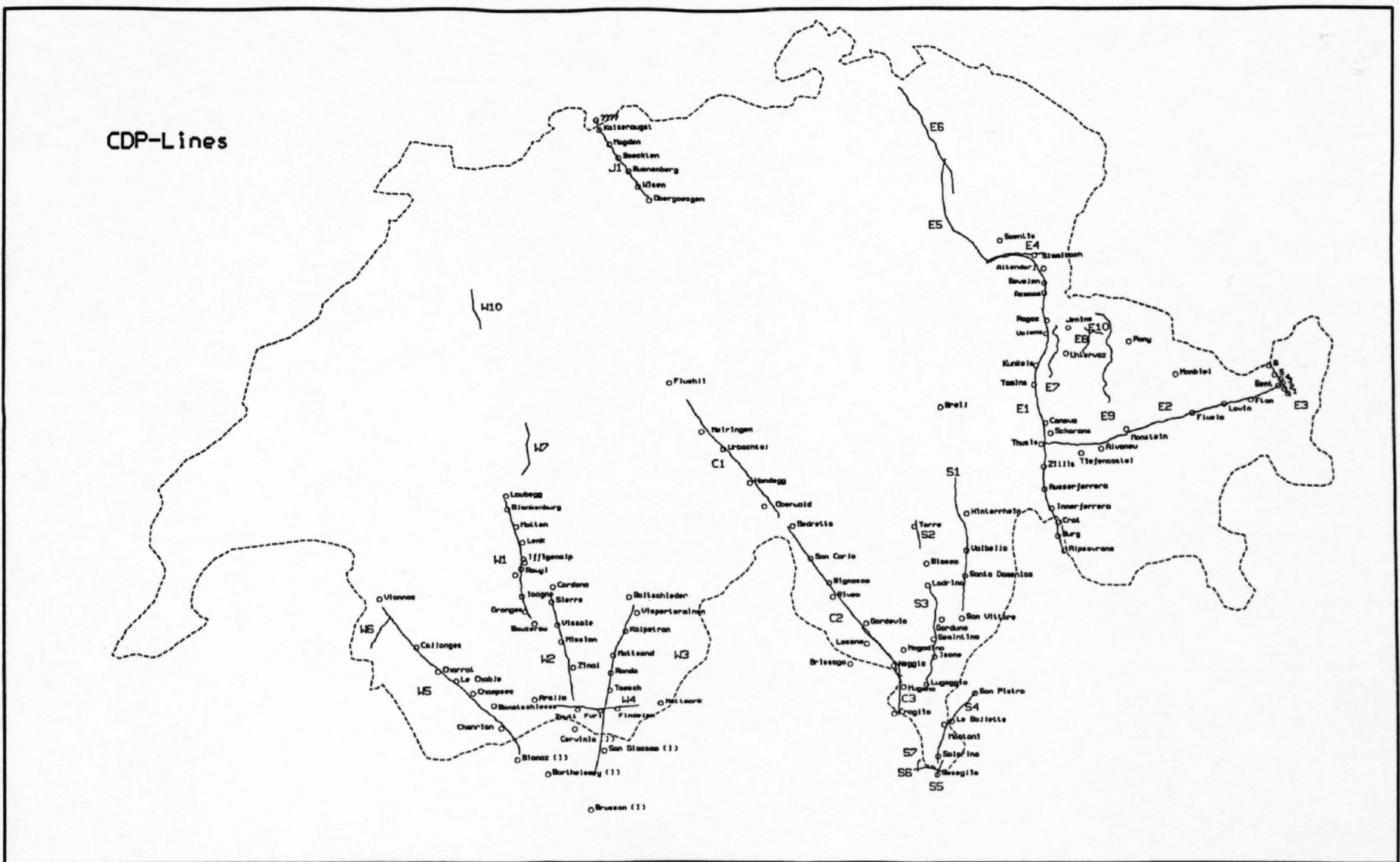

Figure 2-2
Common-depth-point (CDP) lines of the NRP 20 seismic lines. Localities indicated are in-line and off-line shot points of the explosion seismic experiments.

means for conducting a seismic survey of this scale. Large elevation changes of several hundred metres posed significant static problems during the processing stage.

The field work was contracted to Prakla-Seismos AG, Hannover, Germany, and to Compagnie Générale de Géophysique (CGG), Massy, France. Details of the recording parameters are summarized in Table 2-2.

The average length of the receiver spread was almost 20 km, enabling under-shooting of some of the near-surface complexities while providing a sufficient range of offsets for determining the NMO-velocities of reflectors at various depths. The symmetrical split spread configurations ensured continuous up-dip recording across complex structures. For most profiles the use of in-line shots with large offsets from the recording spread effectively extended the subsurface coverage beyond the ends of the lines. At some localities, broadside shots were recorded to give information on the lateral continuation of structures. Additional off-line recordings of the larger explosions were provided by up to 5 km long spreads (48 channels) operated by teams from domestic contractors and the Institute of Geophysics, ETH Zürich. Figure 2-1 displays the geophone lines of the various seis- mic experiments, including the localities of the in-line and off-line shots. The common-depth-point (CDP) line of these experiments are shown in Figure 2-2.

3 Processing of seismic reflection data

W. Frei, L. Levato & P. Valasek

Contents

3.1 Introduction

W. Frei

The data processing was carried out at the two NRP 20 seismic processing centres at the Institutes of Geophysics at the University of Lausanne and at the Swiss Federal Institute of Technology (ETH) Zürich. From the outset, one of the declared objectives of the program was to promote Swiss expertise in the fields of reflection seismic data acquisition and processing. Prior to 1986 virtually no domestic know-how in reflection seismic profiling existed in Switzerland. One of the first decisions taken by the experts committee in 1986 was to install processing facilities rather than entrusting the data processing to foreign seismic contractors. The task of setting up a seismic processing centre in a university environment, where no previous activities in reflection seismic data processing existed, proved to be an enormous one. Many political pitfalls, but also technical problems and the difficulties of finding and keeping experienced and result-oriented personnel had to be tackled in order to remain operational and competitive throughout the duration of the programme. Now, at the final stage of the NRP 20, both processing centres are firmly established institutions capable of handling seismic data as a routine task and featuring their own teaching and training courses.

In hindsight, the goal of raising Switzerland from the status of an underdeveloped country to an internationally recognized expert site with regard to seismic data acquisition and processing has been fully achieved.

The hardware and software systems acquired at Zürich were a VAX-780 (later replaced by a VAX-8650) and the PHOENIX-seismic processing package by Seismograph Service Ltd., Holwood, England. At Lausanne the GEOVECTEUR-package of Compagnie Générale de Géophysique (CGG), Massy, France was installed on a Cray-1 supercomputer.

Both systems provide a comprehensive range of modules for processing industry data. A few minor adaptations were however necessary to handle the up to 60 seconds long crustal data sets. Usually several combinations of standard procedures were tried. The sequence of steps finally applied is outlined in the individual processing history given on the side labels of the seismic sections included in this atlas.

3.2 Normal-incidence data processing

P. Valasek

In the following a brief outline of the (partly standard) processing operations is given. The processing approach undertaken and the amount of effort required depends primarily on four factors:
a) The type of data (high or low multiple coverage)
b) The quality of the data (i. e. the S/N-ratio)
c) The geologic environment investigated
d) The objectives and the type of information sought from the data
With regard to the type of data collected by the NRP 20 two basic sets exist: high-fold Vibroseis for imaging the upper crust and low-coverage dynamite data for deeper targets (see Frei, chapter 2). Complementing the high-fold Vibroseis data are the shallow high resolution profiles recorded with either weight droppers or pop-shot explosive charges for imaging the Quarternary

valley fills (see Pfiffner et al., chapter 21 for details about the acquisition and processing parameters).

The second factor, the quality of the data or its signal-to-noise (S/N) ratio has a significant impact on what takes place in the processing centre, particularly for the deeper penetrating low-fold dynamite data. The quality of the NRP 20 data varies considerably with most sections exhibiting areas of low S/N ratio. In these cases, the effort required to produce a interpretable seismic image was significantly increased.

The third factor which influences the processing scheme is the type of geologic environment investigated. In the Alps, the geologic units exhibit an extreme complexity documenting the protracted tectonic history, which led to the development of this continental collision zone. This is manifested in the data by chaotic reflection phases composed of steep dips, diffractions and discontinuous events. In addition, the extreme topographic and near-surface velocity variations associated with this geologic setting introduce significant static shifts. Reconciling these time delays and unraveling this wealth of information into a coherent representation involves a great deal of analysis and testing throughout the processing flow.

The final factor governing the processing format is the overall objective or the type of information sought. For the NRP 20 data this meant to provide a general representation of the crustal-scale reflectivity across the Alps. In doing so, specialized industry procedures such as wavelet processing and full pre-stack migration were overlooked and portions of the data sets exhibiting good S/N ratio were given less attention compared to areas plagued with poor data quality. This, however, does not mean that the processing was streamlined – on the contrary, it was an extremely challenging and demanding task to arrive at a stage when one was convinced that any additional effort would no longer yield even marginal data improvements. In the Alps one of the most compelling issues is the present geometry of the crustal plates involved in the collision. Exploring for this, as well as for other key interfaces such as the shallower, steep fault zones, pushes the seismic method to its limits. On occasion, spectacular reflections from these features fueled the motivation to look for them elsewhere. However, more often, the images are much more elusive, and recovering them required a great deal of persistance to find the optimum processing flow and parameters. By processing the NRP 20 data with these objectives in mind, the resulting images correctly represent well over 90% of the information which can be obtained from the data.

In summary, the data processing carried out in this study set out to construct crustal scale images across the Alpine collision zone. The procedures undertaken were dictated by the two different data types (Vibroseis and dynamite), the variable data quality and the complexity of the Alpine geology. In general the two different processing formats summarized in Figure 3.2-1 were implemented for the two different data types. Each profile demonstrated some degree of uniqueness requiring certain variations in this general format. The procedures used are all standard steps employed throughout the data processing, however, the method of obtaining the parameters did vary in some cases and the parameters themselves are quite unique to the data and worth describing. In other words, a "cook book" approach to processing these deep crustal data was certainly not adequate. Instead, the processing strategy had to be adapted to address the unique characteristics of each data set. In the following sections, we have highlighted various "adapted" aspects of the processing which we felt were important for the Alpine data sets. It is hoped that these approaches will assist those faced with similar data sets and objectives to successfully produce optimal crustal images.

3.2.1 Bandwidth optimization

One of the key processing steps which was instrumental in improving the S/N ratio of the NRP 20 data was bandwidth optimization. The application of time series operations such as digital filtering and deconvolution to achieve this is quite common and well understood; thus the emphasis here is on the degree to which this needs to be done for certain deep-crustal data sets.

Generally, deep reflections are characterized by a low and narrow frequency spectrum which is usually also occupied by a strong component of background noise. The nature of this bandwidth is dependent on the source wavelet characteristics and the depth of the reflective interface. For the dynamite data, the source wavelet varied considerably and in all cases, the attenuation of the higher frequencies with increasing depth was evident.

For the NRP 20 data, an improvement in the quality of the deeper events was
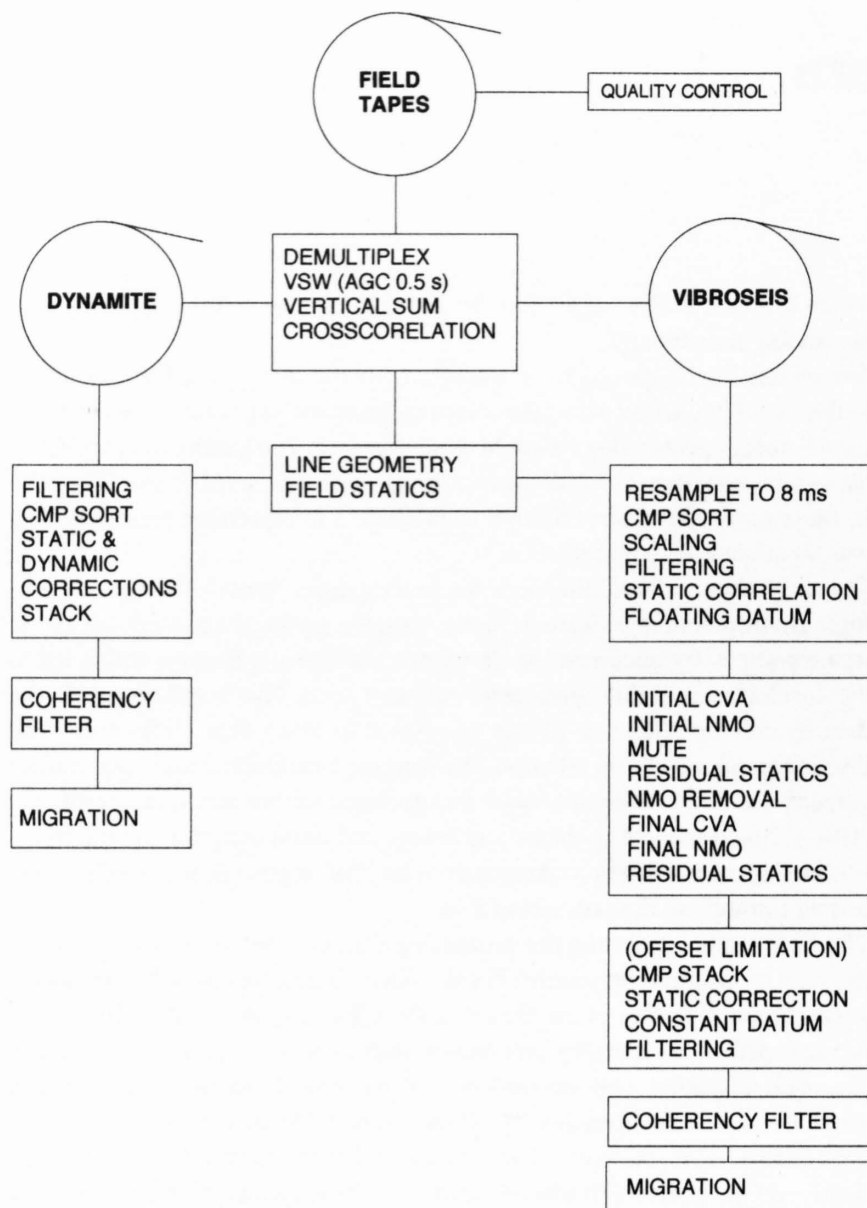
FIELD TAPES ——— QUALITY CONTROL

DYNAMITE ——— DEMULTIPLEX / VSW (AGC 0.5 s) / VERTICAL SUM / CROSSCORELATION ——— **VIBROSEIS**

LINE GEOMETRY / FIELD STATICS

FILTERING
CMP SORT
STATIC &
DYNAMIC
CORRECTIONS
STACK

COHERENCY
FILTER

MIGRATION

RESAMPLE TO 8 ms
CMP SORT
SCALING
FILTERING
STATIC CORRELATION
FLOATING DATUM

INITIAL CVA
INITIAL NMO
MUTE
RESIDUAL STATICS
NMO REMOVAL
FINAL CVA
FINAL NMO
RESIDUAL STATICS

(OFFSET LIMITATION)
CMP STACK
STATIC CORRECTION
CONSTANT DATUM
FILTERING

COHERENCY FILTER

MIGRATION

Figure 3.2-1
General processing sequence for the NRP 20 Vibroseis and explosion seismic data.

usually realized by first balancing the spectra (primarily using gap-deconvolution) within a wide window centered around the dominant signal frequency and then isolating just the signal with a narrow bandpass filter (see Valasek et al., 1991). To account for the general attenuation of the higher frequencies with depth, both of these operators were designed to be time-variant. The determination of the final bandpass filter parameters was carried out by applying a series of filters to the data and then carefully examining the filtered data to define the time-varying frequencies which best represented the overall reflectivity. In general, the bandwidth varied from 16–32 Hz near the surface and continually decreased to as low as 4–12 Hz at two-way travel times of 16 to 20 s. This effort to optimize the signal bandwidth usually led to a significant improvement in the overall data quality and was largely responsible for being able to map the crust-mantle transition to depths of greater than 50 km within the Alpine collision zone.

3.2.2 Effective determination of stacking velocities

As described earlier, the general wavefield recorded across the complex Alpine subsurface was quite scattered and variable. Initial stacked sections revealed considerable lateral changes from zones consisting of dense packages of variably dipping, discontinuous reflections to areas exhibiting little or no reflectivity. The apparent lack of reflection continuity made it difficult to determine stacking velocities by the traditional approach of extrapolating a series of 1D velocity functions obtained from uniformly spaced constant velocity analysis (CVAs). In this situation, this method has the potential of missing important lateral variations in stacking velocities. Instead, CVAs were calculated across a much larger portion of the data and in some cases the entire profile was used. This usually leads to a greater number of "image-based" velocity functions compared to the sparser, more statistically-based functions obtained from the traditional incremental CVA approach. By analyzing an extended spatial window, the rapid lateral changes in the stacking velocities could be more readily determined which generally led to stacked images with improved lateral continuity.

3.2.3 Single-fold sections

The dynamite sections recorded by NRP 20 generally had a multiplicity which varied from 1 to 5 fold. Initial sections obtained by stacking the full fold of traces generally showed a significant reduction in the data quality when compared to the individual shot gathers. This result most likely arose from the combined effect of variable source wavelets and unresolvable statics which led to destructive interference during stacking. To avoid these problems, single-fold sections were formed by selecting only the optimum trace from each midpoint gather. Klemperer et al. (1986) successfully implemented a similar approach for COCORP deep crustal data recorded across the Basin and Range which was plagued with problems of statics. In these situations, it is still worthwhile to record multiple coverage to improve the odds of obtaining a continuous range of high-quality data.

3.2.4 Optimal post-stack scaling

The importance of post-stack scaling is often overlooked throughout the processing of deep crustal data. Its usage is critical, however, for effectively communicating the content of the data. According to the general objectives outlined earlier, scaling was designed to express the amplitude contrast of reflections rather than on preserving their original magnitudes. Thus, statistical, trace-dependent scaling functions such as automatic gain control (AGC) and time-variant trace equalization were applied to the data. In general, trace equalization was used for data which exhibited good S/N ratio, whereas AGC was applied in cases where the data quality was poor.

The key parameter for scaling is the window design. It is often tempting to use a constant, small window (usually < 1000 ms) because of the extreme amplitude decay which occurs at the shallow portions of the long records. However, for the NRP 20 data, particularly the deeper sections, this type of amplitude balancing was found to be too severe and degraded the weaker amplitude contrasts. At this stage in post-stack processing, any surviving differences in amplitude between the signal and noise need to be carefully preserved and if possible emphasized. To achieve this, time-variant windows were designed with lengths increasing from a few hundred milliseconds near the surface to over 5 s at the deeper levels (> 10 s two-way travel time TWTT). Additionally, the trace equalization windows were set to overlap in order to provide a smoother scaling function. This type of scaling emphasizes the large-scale relative amplitude variations at the expense of obtaining true amplitudes or of illuminating the finer details of individual reflection packages.

3.3 Processing and 3-D effects of the NRP 20 seismic data: effectiveness of single reconnaissance lines

L. Levato

In a complex tectonic context, such as the Alps, seismic processing is affected by specific problems. In particular, the reflections are generated by interfaces that are rarely horizontal and parallel. Moreover the presence of reflectors with a dip component perpendicular to the plane of the seismic section may generate out-of-plane reflections. Among the seismic lines processed by GRANSIR (Groupe Romand d'Analyse Numérique de Sismique Réflexion), two will be discussed to illustrate these problems. To allow the stacking of both dipping and horizontal reflections with their correct velocities, dip move out (DMO) corrections were applied to the profile E1. Local improvements were obtained in the seismic image, however the effectiveness of this processing step is limited by the occurrence of 3D effects. Although the problem of cross-line dips can be completely addressed only with a 3D survey, the application of pseudo-3D processing with lateral dip corrections on slalom line W2, improved the seismic section and brought valuable information on the 3D structure of the area under consideration.

3.3.1 Introduction

As in most of the deep seismic profiling projects, direct ties to geology by well data are missing in the analysis of the seismic profiles of the Swiss Alps. However, the particular geologic structures, characterised by good exposures with steep dips, has allowed down-plunge projections useful to interpret the observed reflections (e. g. Pfiffner et al., 1990 a and b, and Marchant et al., 1993). This technique is particularly valuable when associated to seismic modelling, possibly 3D, where the model itself is modified until it generates a seismic response close to the seismic section (e. g. Litak et al., 1993, and Levato et al., 1994). These modelling studies have clearly shown the importance of three-dimensional effects on the 2D seismic sections. It is therefore interesting to analyse the limitations of 2D seismic surveys in the context of the seismic processing. In particular, DMO corrections and lateral dip corrections (pseudo 3D) were applied to two seismic lines in order to improve the coherence of the reflections. Results of these processing sequences are dis-

cussed after a short presentation of other processing which notably improved the signal to noise ratio or produced complementary seismic sections useful for the interpretation.

3.3.2 Processing

The processing sequences applied by GRANSIR to the NRP 20 data are described in du Bois et al. (1990a) and Levato et al. (1993). Among the processing steps that enhance considerably the quality of the seismic image are spectral balancing and surface consistent residual static corrections. Spectral balancing is effective in attenuating strong, low-frequency noise, while surface consistent residual static corrections are required to resolve the time delays observed on the NMO corrected CMP gathers.

The irregularity of the reflecting interfaces may cause scattering and defocusing of the energy and may result in poor quality of the images obtained when stacking the data from the entire recording spread. Due to the large field spread and high folding coverage, it was possible to perform different offset partial stacks which, in some cases, produced improved images and allowed to refine the interpretation of some reflections (Pfiffner et al., 1991).

To overcome the problems related to the migration of deep seismic data (Warner 1987), Marchant et al., 1993, used a program developed by Sénéchal and Thouvenot (1991) which performs a geometrical migration on digitised line-drawings and is based on the principle of the common tangent of two spherical wave fronts. The migration velocity function can vary smoothly in both depth and distance. The digitisation is performed on hand-drawn line-diagrams and the events are distributed in two-to-four classes according to their different strengths.

Dip moveout (DMO)

The moveout is a dynamic correction needed to produce a zero-offset section. For a dipping reflector the moveout is composed of two terms, one associated with the zero-dip normal moveout and the second related to the reflector dip. The latter is null for zero dip and increases with increasing dip

and with decreasing velocity. The effect of the dip on the moveout is therefore generally larger in the shallow part of the seismic section. When dipping reflectors are present, it is possible that two events at the same travel times have different stacking velocities. In standard processing only one event can be selected and the resulting stack is not the zero-offset section, which ideally would be recorded if the source and receiver positions were coincident. As a direct consequence, the post-stack migration which is based on the assumption that the stacked section is a zero-offset section, is not very good. The DMO corrections redistribute the energy of the dipping events to the appropriate CMPs and allow to stack both dipping and horizontal reflections with their correct stacking velocities. DMO corrections on 2D data can give good results if the seismic line, recorded in the dip direction, is a truly 2D seismic section. When out-of-plane reflections and off-line diffractions are absent, the quality of the post stack-migration after DMO processing is generally improved. However when these events occur, DMO corrections and two-dimensional migration are incapable to generate a correct image of the subsurface because the reflections cannot be positioned to their proper locations, and the diffractions cannot be collapsed. In such cases, 3D modelling can be used instead of 2D migration, provided that the knowledge on the structures from the surface geology is sufficient to allow the 3D model to be built (e. g. Litak et al., 1993).

DMO corrections were applied to one of the Alpine seismic lines, E1, located in eastern Switzerland. The processing scheme followed is similar to the one described in Levato et al., 1990. Although out-of-plane reflections are of common occurrence in the Alps, local improvements were obtained for some shallow dipping reflections. The following analysis is based on the geologic descriptions and seismic interpretations given in Pfiffner et al, 1990, Pfiffner et al., 1991, Litak et al., 1993, and Green et al., 1993.

Figures 3.3-1a and b show the northern part of line E1 before and after DMO corrections respectively. The observed reflections arise from weakly deformed layers that have been moved along shallow-dipping thrust faults. Four series of arrows point to north dipping reflections of different strength between the locations Sevelen and Bad Ragaz. After DMO corrections the three shallower events appear stronger and more continuous. These reflections define the geometry of the thrust faults of the region. The deepest and strongest reflection, arising at the contact between Mesozoic carbonates and
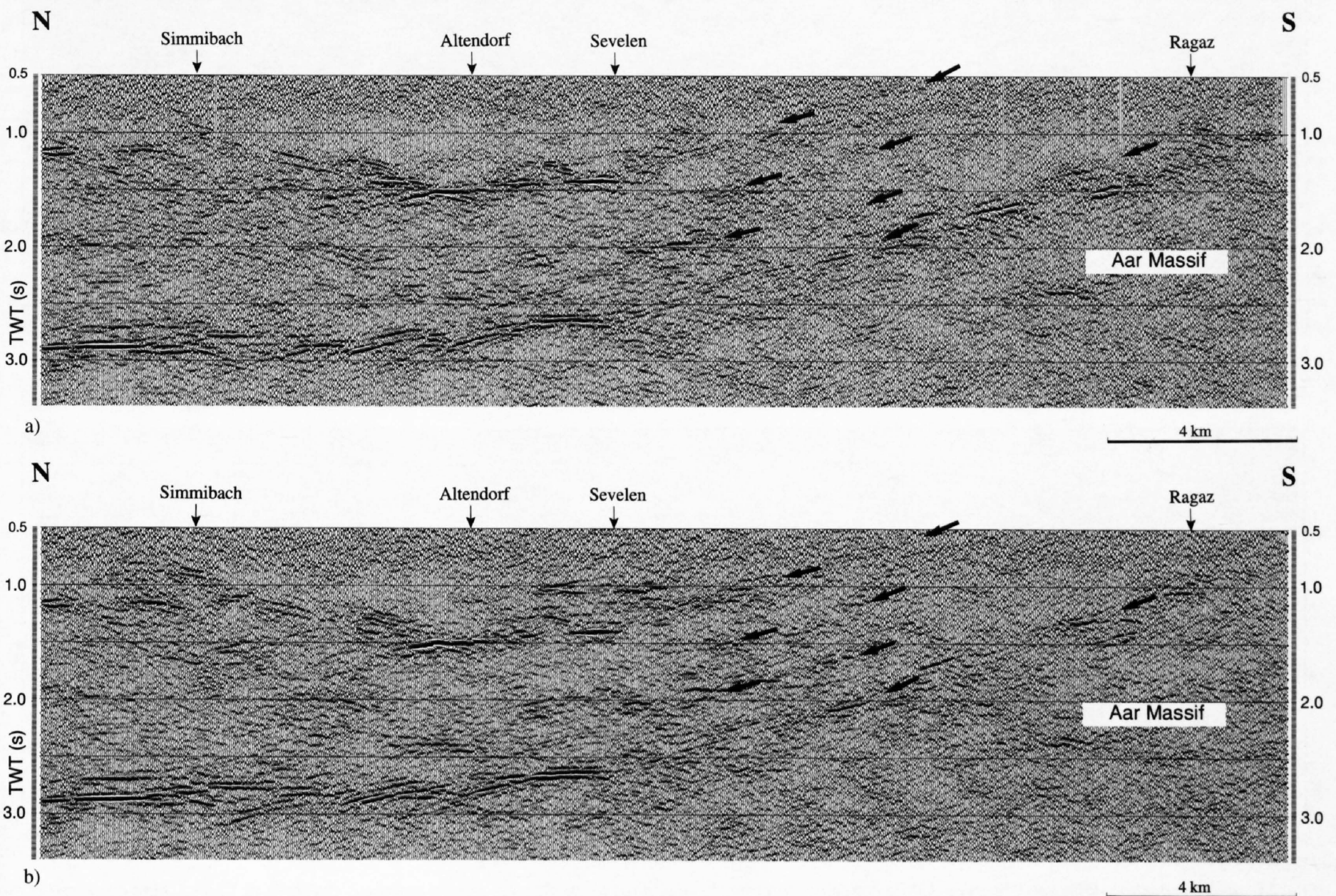

Figure 3.3-1

Northern portion of the Vibroseis™ seismic line E1. A mild coherence filter has been applied to the data for display purposes. Aar massif: crystalline basement uplift.

a) The stack without application of the DMO corrections. To help the comparison, the arrows point to events which are better imaged on Figure 3.3-1b.

b) The stack after application of the DMO corrections. Note the improvement in strength and/or continuity for the four dipping events pointed by the arrows between Sevelen and Bad Ragaz.

the crystalline rocks of the Aar massif, shows the geometry of the top of the massif. Note that after DMO corrections this reflection has a sharper trend. The southern part of the section is characterised by sheets of highly strained rocks which have been thrust in a direction parallel to both the foliation and the lithological contacts within the nappes. These conditions are suitable for the generation of strong and continuous reflections. It is also known that these units have relatively steep dips perpendicular to the recording line, thus out-of-plane reflections and diffractions are expected on the seismic section. Figures 3.3-2a and 3.3-2b show the southern part of the line before and after DMO corrections respectively. Figure 3.3-2c shows the post-stack migration

of the DMO corrected version. Four groups of events, A to D, are analysed going from south to north and from shallow to deeper events. Also one of the possible 3D events is pointed out.

Event A is due to a thin layer of carbonates pinched between two blocks of basement rocks: the Splügen zone. On Figure 3.3-2b beneath Burg, this event is more continuous and the top and the base of the layer can be separated more easily than on Figure 3.3-2a. On the migrated section (Figure 3.3-2c), these interfaces are imaged by continuous reflections and the gap between them increases going from south to north. These features fit with the field observations suggesting a continuous Splügen zone that thickens toward the north.
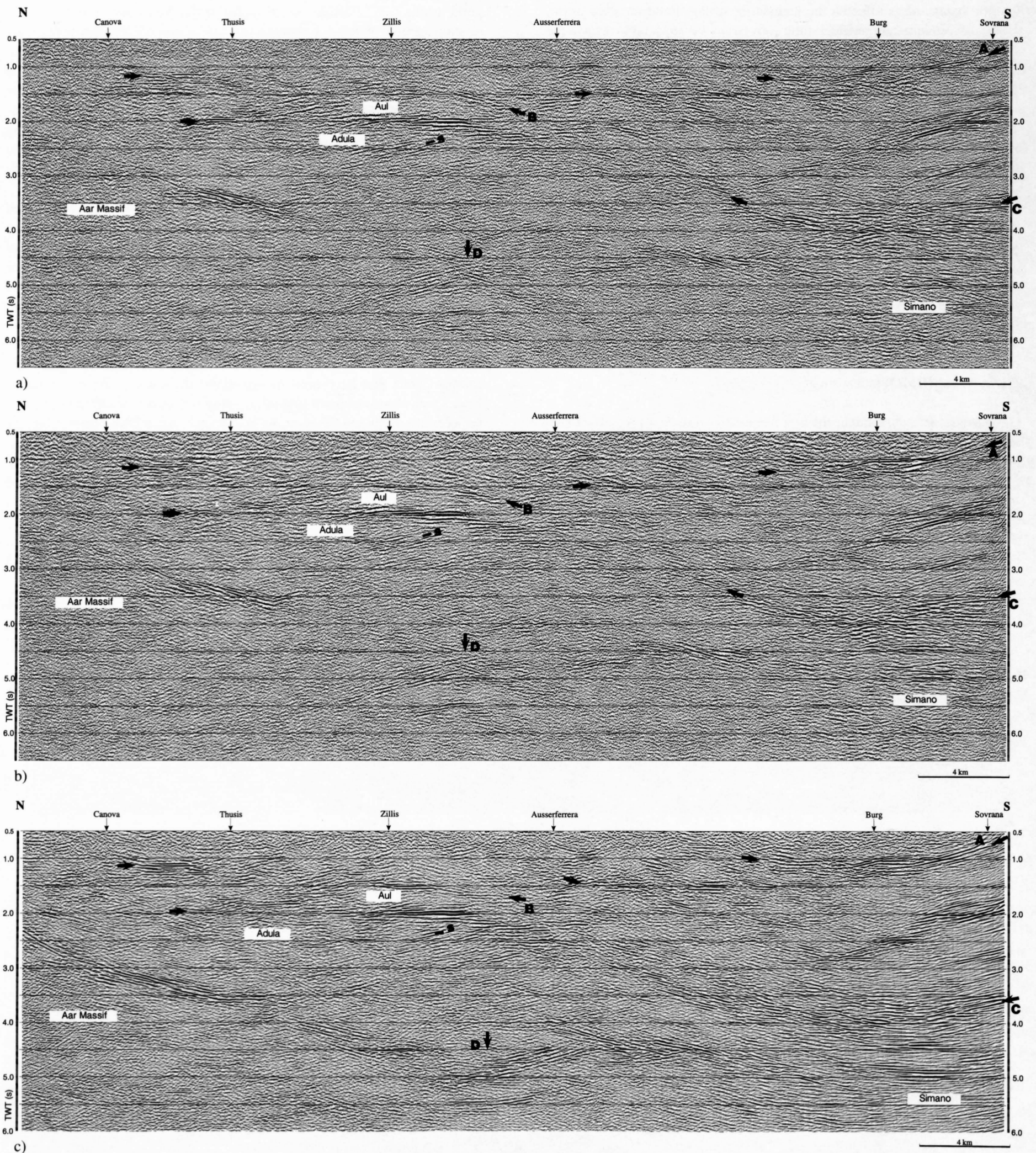

Figure 3.3-2

Line E1, southern portion, Vibroseis™ survey. A mild coherence filter has been applied to the data for display purposes. Events A, B, C, and D are discussed in the text. The arrows pointing to the south delimit the extension of reflections A (top and bottom), B, and C. Event s is a probable 3-D effect. Aul, Adula, and Simano: nappes. Aar Massif: basement massif.

a) Stack without application of DMO corrections.

b) Stack after application of DMO corrections.

c) Post-stack migration after DMO corrections. Criss-cross events confirm that 3-D effects are present. Remarkable the continuity of the top of the Adula nappe, event C.

18

Events B and C show the geometry of the top of two nappes, Aul and Adula. Both reflections are more continuous after DMO corrections, especially the group of events C (top of Adula) which extends over more than 35 km and shows different orientations: north dipping beneath Sovrana, south dipping between Burg and Ausserferrera, and almost horizontal between Ausseferrera and Thusis. The interconnection of the several elements of reflection C is less obvious on the section without DMO corrections (Figure 3.3-2a). The continuity of this event is excellent on the migrated section (C on Figure 3.3-2c) which well images the ramp-anticlinal geometry of the top of the Adula nappe.

The north dipping events "s" are interpreted as diffractions emanating from discontinuities associated with the Aul nappe and located outside the plane of the seismic section. Post-stack migration is unable to collapse them (Figure 3.3-2c).

The last event, D, has a "bow-tie" shape which appears stronger after DMO processing, especially the bottom nearly horizontal portion of the "bow-tie" at 5 s. Subsequent migration (Figure 3.3-2c) partially restores the expected synclinal shape. A plausible interpretation of this event has been successfully tested by 3D modelling. In the final model the syncline is simulated by the top of the Simano nappe terminating against the top of the basement massif. Figure 3.3-2c shows that post-stack migration after DMO corrections is unable to uncross all the criss-cross events even if appropriate velocities are used. Thus the presence of out-of-plane reflections and diffractions is confirmed. Nevertheless, the previous discussion proves that, being aware of the 3D effects, it is still possible to extract some useful information on the shape of the reflectors.

Pseudo-3D applied to slalom line W2

Although the NRP 20 lines were generally recorded in the dip direction, 3D effects due to the complex alpine structures are a contributing factor to the seismic images. In particular, the coherence of the reflections on the final section may not be optimum because of the effect of the lateral dips of the reflectors. These dips may cause a time shift of the signal on the traces of a CMP gather. Static and NMO corrections alone cannot account for these time shifts. In an attempt to extract some information concerning the 3D structure of the studied units, the Slalom Line® technique developed by CGG (1979) was used on line W2, located in western Switzerland, to produce short seismic sections that are perpendicular to the main trend of the profile (du Bois et al., 1990b). From these "cross-lines" stacks, it was possible to evaluate the lateral dips which were automatically corrected before CMP stacking.

The method is based on the management of the seismic traces through a grid of bins which covers the CMP scattergram computed from the source-geophone coordinates. In particular, the bins perpendicular to the main trend of the profile can be selected to view partial stacks across the CMP swath (Figures 3.3-3 and 3.3-4). A compromise between average fold of coverage in each bin and spatial aliasing in the investigated direction has to be made when selecting the width of the bins which corresponds to the distance between the perpendicular CMPs. This is the main constraint on the applicability of the method.
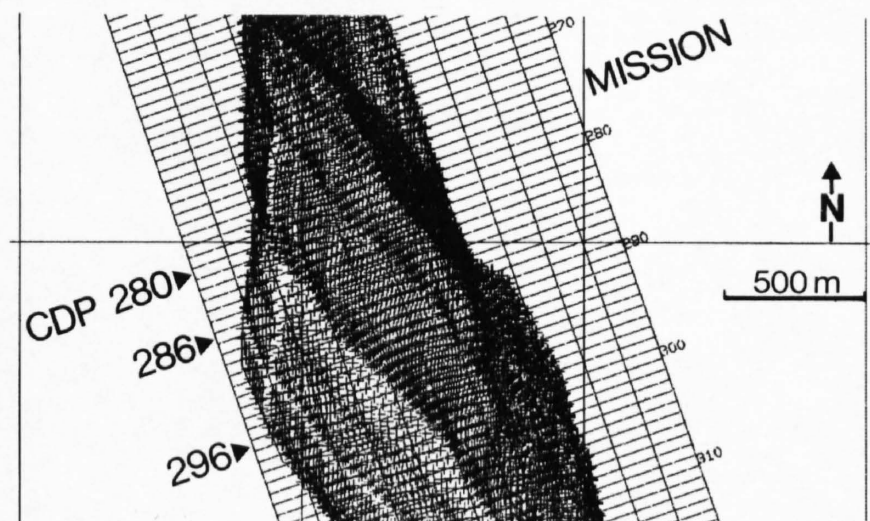

Figure 3.3-3
Line W2, Vibroseis™ survey. Portion of the CMP scattergram and associated grid of bins. Each bin can be addressed individually by two numbers: CMP number along the main trend of the profile and "strip" number in the perpendicular direction. The traces belonging to one bin are added together to form one trace. It is therefore possible to view "cross-line" stacks. "Mission" is a location name. In Figure 3.3-4, the "cross-line" stacks across CMPs 280, 286, and 296 are shown (after du Bois et al., 1990b).
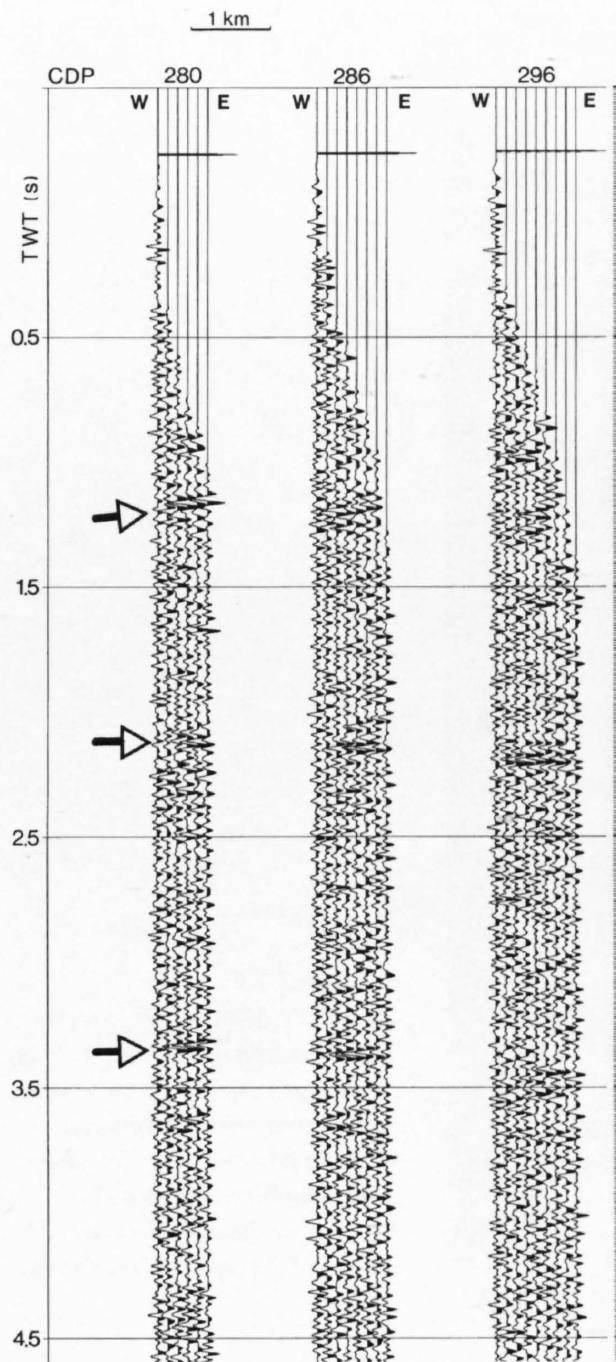

Figure 3.3-4
Line W2, Vibroseis™ survey. "Cross-line" stacks in the W-E directional along the three strips indicated in Figure 3.3-3. The arrows point out different dips along the time axis for three events. We can notice a westward dip for the first event at about 1.2 s, almost no dip for the second one, at about 2.1 s, and a small westward dip for the third event at about 3.3 s (after du Bois et al., 1990b).

The traces of each cross-line correspond to a single CMP gather along the main direction. Note that the lateral dips vary with time (Figure 3.3-4), therefore to attenuate the destructive effects of the lateral dips on the in-line stack, the corrections cannot be constant along a trace but have to be "dynamic" (dynamic stack). The observed lateral dips can also provide information on the 3D structure of the interfaces. In this case, the dip is mainly westward and amounts to about 10°. Figure 3.3-5 shows the improvement of the stacked section after application of the lateral dip corrections.

3.3.3 Conclusions

Both processing and modelling have shown that in the complex Alpine tectonic, three-dimensional effects are common and limit the performance of the 2D migrations. Although only a full 3D survey would provide a comprehensive seismic image of the region, precious information has been extracted by the NRP 20 seismic data. To address the problem of imaging both horizontal and dipping events, GRANSIR applied DMO corrections to line E1. The post-stack migration fails to provide a correct image of the sub-surface because it cannot deal with out-of-plane reflections and diffractions. However, effective improvement in the continuity of dipping layers is obtained. Sometimes it is possible to transform the handicap of laterally dipping layers into the opportunity of extracting information on the 3D geometry of the investigated structures. In some cases the excellent knowledge of the dipping nappe surfaces allows the definition of a 3D model of the region being studied. In other cases, as for the slalom line W2, the acquisition geometry is appropriate to investigate "cross-line" stacks and to deduce information on the cross-dips of the reflectors.
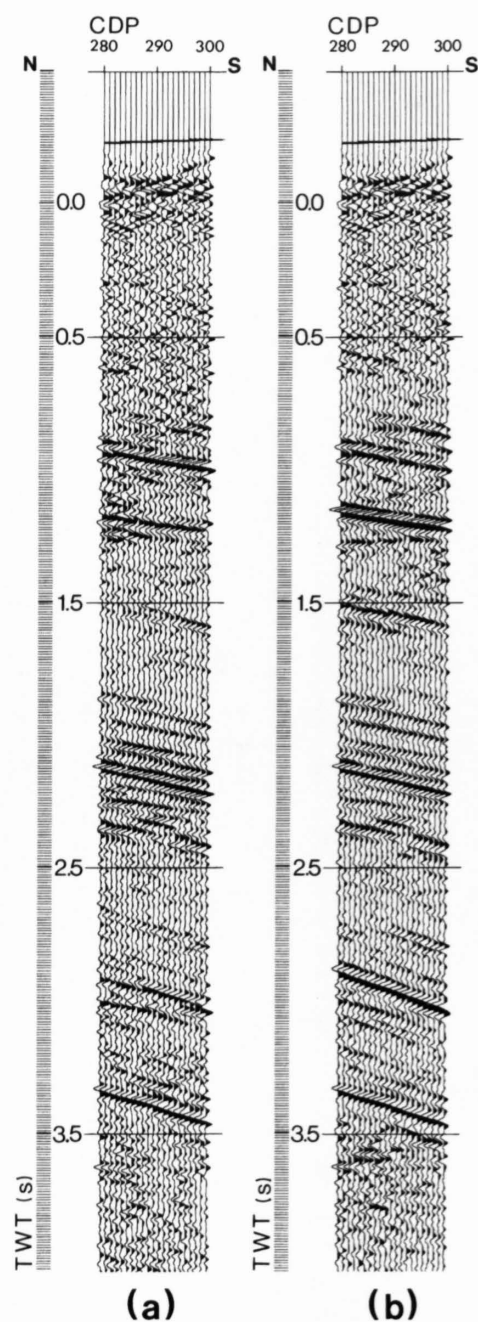
Figure 3.3-5
Line W2, Vibroseis™ survey.
Comparison of normal stack (a)
and stack after dynamic lateral
dip corrections (b) between
CMPs 280 and 300. Note the
improvement obtained espe-
cially for the event located at
about 1.2 s (after du Bois et al.,
1990b).

3.3.4 Appendix

GRANSIR processing centre is based at the Institute of Geophysics of the University of Lausanne and uses Géovecteur™ software (Compagnie Géné-rale de Géophysique) running on the CRAY super computers of the Federal Polytechnic School of Lausanne (EPFL/SIC), and, more recently, on a SUN Sparc10 workstation. GRANSIR was the first academic team to have access to a high technology facility such as the CRAY1S/2300, in 1986. Since then GRANSIR have continued to have access to the most advanced computers as EPFL has followed the hardware evolution to the CRAY 2, and to the CRAY YMP. The CRAY 1S/2300 had 2 Mword (64 bits/word) of central memory, two disk drives DCU-4, eight disks DD-29 (600 Mbytes each), 2 tape drives (1660/6250 bit/inch). The CRAY2 had 2 Gbytes of central memory, 4 pro-cessors, 4 disks DD-49 and 16 disks DD-40 (total capacity of 24.8 Gbytes), 2 manual cartridges units. Since 1989, the EPFL is equipped with a cartridge storage system driven by a robot which allows 6000 cartridges to be accessed automatically through 4 lectors. To accomplish modelling studies, GRAN-SIR uses the SIERRA software by Landmark, running on a SUN Sparc2 workstation.

Acknowledgements

3.4 Wide angle data processing

P. Valasek

The network of refraction profiles recorded across the Alps provided an ex-cellent sampling of the deep structures along sections which extend for seve-ral hundreds of kilometres. Traditionally, the only processing which is ap-plied to these data is bandpass filtering and trace normalization. This minor treatment is intended to preserve as much of the original signal character as possible for identification and correlation of refracted phases. The traveltime behaviour of the various crustal phases is then used as a constraint for deter-mining the velocity structure using ray-based, 2D forward modeling.

The standard format for presenting refraction data is in reduced traveltime (cf. Figure 3.4-1a; Maurer, 1989). While this representation is efficient for modeling purposes, it is not an effective means of expressing the usually high-quality reflection phases. To provide an alternative display, the refrac-tion data were transformed into normal-incidence sections. A total of four single-fold sections were generated using data from ALP75, ALP77, ALP87 and the EGT (European Geo-Traverse). The remaining, primarily older re-flection profiles could not be processed in this manner because they are not available in digital format.

The basic approach undertaken was similar to that employed for the NRP 20 dynamite sections. The reversed refraction observations recorded along the four lines were sorted according to their midpoint locations, shifted to a con-stant datum (700 m), muted to eliminate the refracted and shallow reflected phases, normal-moveout (NMO) corrected and bandpass filtered. By using the average crustal velocity for the NMO correction, the traveltime behaviour of the Moho reflection (PmP phase) can be approximated and removed across the large range of offsets. This operation is inappropriate for intracrus-tal reflectivity, and hence, the resulting profiles are valid only for the PmP re-flections, and any shallower reflectivity which remains is typically under-compensated.

For the EGT profile, the geometric influence of the general Moho topography on the traveltimes was also taken into account. From earlier refraction re-sults, the European Moho was shown to plunge araound 10° southward (Müller et al., 1980). This causes an up-dip or northward shift in the observed reflection hyperbola which can be corrected for by dividing the average ve-locity by the cosine of the angle of dip. This resulted in using a velocity of 6.2 km/s for the NMO correction.

As was the case with the NRP 20 reflection data, bandpass filtering was an important processing step. In this case it was vital to spatially vary the band-pass filters to account for the significant lateral changes in the spectral con-tent ccross the long recording aperture. The combined effects of dispersion and the separation of the head wave from the overcritical reflection leads to a significant drop in high frequencies beyond the critical distances. To account for this, bandpass filters were generally designed with a range of 12–20 Hz at near offsets and gradually decreased to 2–8 Hz beyond the crit-ical offset (> 90 km). This step generally led to recovering a continuous Moho (PmP) reflection extending from the zero-offset range to well beyond the critical distances.

As a final processing step, the envelope function was obtained by calculating the Hilbert transform (Figure 3.4-1c). The effect of this step on the image is to form a more coherent representation of the total reflection strength associ-ated with each instant of time rather than an average over a time interval.
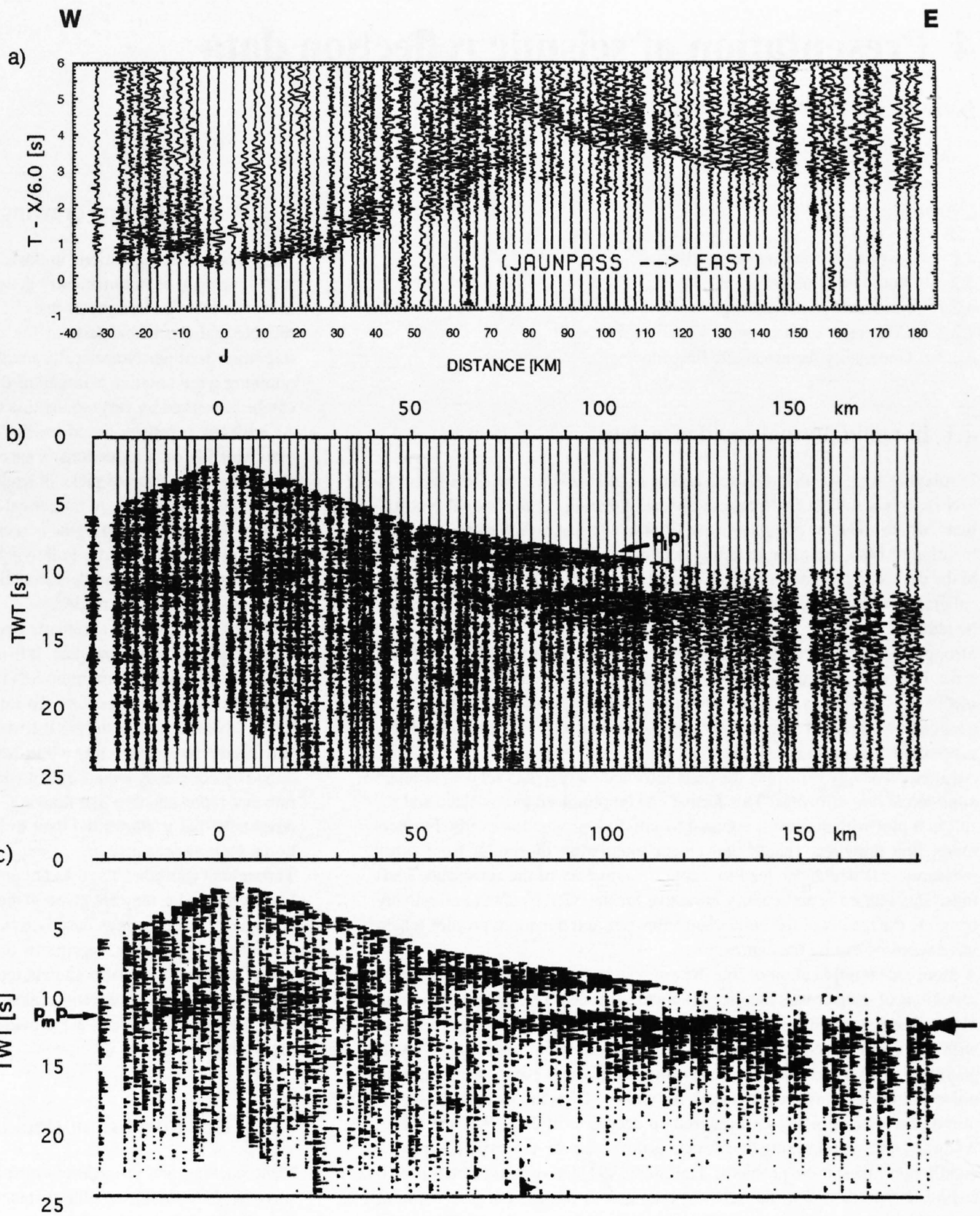
W   E

a)

(JAUNPASS --> EAST)

T - X/6.0 [s]

DISTANCE [KM]

J

b)

0   50   100   150   km

TWT [s]

PₘP

c)

0   50   100   150   km

TWT [s]

PₘP

Figure 3.4-1
Converting seismic refraction data to a normal-incidence section.
a) Reduced traveltime display of the refraction gather recorded from shot point Jaun (J) on line ALP87 (see Fig. 23-1b for location).
b) The same gather after processing was applied to produce a normal-incidence section.
c) The normal-incidence section represented in terms of its reflectivity strength (envelope function).

4 Presentation of seismic reflection data

P. Valasek & W. Frei

Contents

4.1 Imaging normal-incidence data

Displaying large seismic data sets and/or smaller seismic data sets with low S/N ratio is a subject that requires special attention. Conventional plot formats, which show the *complete wave form* as wiggles, variable areas or combination of both, are often to dense to either express adequately the content of the data or to provide sufficient contrast. In addition, the resolution of typical graphical output devices can limt the amount that any seismic image may be reduced.

Strong coherency filtering of the data and a display of only the largest amplitudes has been used to generate *pseudo line drawings* automatically. This method has the disadvantage of laterally smearing events. Although the contrast can be increased significantly, the plotter resolution is still limited, because there is no data reduction.

An alternative way to display the main information of a data set is to produce *hand-made line drawings*. This format can be produced at any scale and result in a plot with sufficient contrast to satisfy reproduction needs. Furthermore, line drawings enable convenient integration of results from other measurements which can lead to a concise summary of the subsurface findings. This feature is particularly attractive for the NRP 20 data to effectively combine the results of the coincident Vibroseis and dynamite profiles which were acquired during the campaigns.

A more recent application of line drawings is to provide high-quality representations of deep crustal data for ray-theoretical depth migration (Raynaud, 1988). Deep crustal data often exhibit extremely variable data characteristics with an overall low S/N ratio. The use of wave equation based migration algorithms can lead to poor results by obscuring weak events with smeared noise and introducing artefacts such as "smiles" from the isolated high-amplitude events commonly encountered on deep crustal data (Warner, 1987). As an alternative, migrating line drawings through a ray-theoretical approach greatly minimizes these problems. Holliger (1991) has expanded on this procedure and applied it to the NRP 20 data across the eastern and southern Swiss Alps. He demonstrated that migrating line drawings provides a satisfactory repositioning of the data which originally exhibited a wide range of S/N characteristics.

The traditional method of obtaining line drawings is to manually trace visually correlatable events which are determined to be geologically relevant reflectors. The foremost disadvantage of this representation is the loss of amplitude and phase information. However, a portion of this information can be qualitatively preserved by constructing the drawing with line thicknesses corresponding to the observed variations in reflection strength. Other drawbacks are related to the potential introduction of human bias and error and because of the time and effort required. Comparisons of such line drawings with the seismic sections are discussed by Pfiffner & Hitz in Chapter 9 in the context of the Eastern Traverse. In the application to the NRP 20 data along the Eastern and Southern Traverses, Holliger (1991) reduced some of the subjectivity and error by taking into account line drawings from several workers which tends to average out the influence of these factors. Nevertheless, it is nearly impossible to completely eliminate biased input and errors, some of which may have significant impact on subsequent procedures such as migration and interpretation. Migration becomes more important as the data complexity and depth increases. In these situations, any errors in representing the data are further magnified by migration. Furthermore, migration performs best when the S/N ratio is high and the complete wavefield is available. While the noise reduction obtained by line drawings works in favour of improving the S/N ratio, the potential exists for neglecting or missing events which are important for migration (i. e. weak diffractions). Another problem arises because the ray-theoretical migration routine operates on linear segments which makes it difficult and tedious to represent curved reflections with linear segments by hand.

4.2 Automatic line drawings

To overcome the limitations imposed by hand line drawings, a new method was developed to automatically generate the information. The goal was to automate what an interpreter does by visual correlation in a more objective, reliable and repeatable fashion for subsequent input into the line drawing migration routine. Numerically extracting lines also has the advantage of retaining a quantitative estimate of the relative reflection amplitudes which can be preserved by varying the line thicknesses accordingly.

As with any computer-based prediction method, the algorithm developed to automatically pick reflections is susceptible to errors. In this case, they are primarily in the form of picks of irrelevant information (i. e. coherent noise) and to some degree due to numerical artifacts. However, the information determined for the primary signal is accurate, complete and objective and leads to an improved migration. Following migration, the discrimination against the picked noise and the determination of which components are geologically significant can be made.

The performance of the automatic line drawing routine is strongly dependent on the quality of the input data. It is demonstrated that this procedure works well for data having a minimum S/N ratio of 1.0 which is usually not realized in deep-crustal investigations. To improve the quality of data exhibiting a lower S/N ratio such as the NRP 20 data, the stacked images were coherency-enhanced prior to extracting a line drawing. The increase in the S/N ratio obtained by coherency enhancement enables the automatic picking of an accurate and representative line drawing. This preconditioning step also has the advantage that it allows the data to be effectively displayed using conventional plotting formats.

Throughout this atlas, the data are presented in two formats: In the Plates to Chapters 8 to 12, they are given in the form of a coherency-enhanced image. Automatic line drawings based on the enhanced image are used in the Figures to these Chapters, serving as base for identifying and labeling reflections. The generation of both data representations relies on the use of localized slant stacks to obtain and evaluate spatial and temporal reflection coherency. Sections 4.2.1 and 4.2.2 provide the background behind this important data transformation.

4.2.1 Localized slant stacking

Slant stacking is a procedure which has been applied to transform seismic wave fields in the travel-time-distance (t, x) domain into the tau – ray parameter (τ, p) domain where τ represents the intercept time or zero-offset TWT and p can be related to either the apparent slowness (inverse velocity) or apparent dip depending on the application (Schultz & Claerbout, 1978; McMechan & Ottolini, 1980; Phinney et al., 1981; Chapman, 1981). This transformation results in a focusing of linear events into points and a mapping of reflection hyperbola into ellipses. In the (τ, p) plane, these components are clearly separated and can be effectively isolated and inverse transformed back to the (t, x) domain with minimum distortion.

Most of the earliest applications of slant stacking have been designed to obtain velocity information as a function of depth by inverting τ-p transformed seismic array data either from refraction recordings (McMechan et al., 1982; Clayton & McMechan, 1981; Milkereit et al., 1985) or near-vertical incidence shot (Schultz & Claerbout 1978; Stoffa et al., 1981; Schultz, 1982) or common depth-point (CDP) gathers (Diebold & Stoffa, 1981). Other common applications are carried out on offset gathers to remove coherent noise such as ground roll or multiples (e. g. Treitel et al., 1982). In all of these cases the transformed data are calculated by summing samples across the entire offset section along different ray parameters to produce a gather composed of traces representing each of the slopes considered (Figure 4-1). In the applications introduced above, the distribution of elliptical and concentric trends are then either used in a variety of inversion schemes to obtain average or interval 1D apparent velocity functions or they are attenuated prior to inverse transformation back to the (t, x) domain.

Localized slant stacking was first implemented by McMechan (1983) to map 2D velocity variations and involves a slight variation of the τ-p transform described above. Instead of transforming the entire record to produce a single τ-p gather, he calculated several localized gathers by slant stacking across overlapping windows of finite offset or aperture. The resulting set of τ-p gathers served to distinguish slight variations in the apparent phase velocity
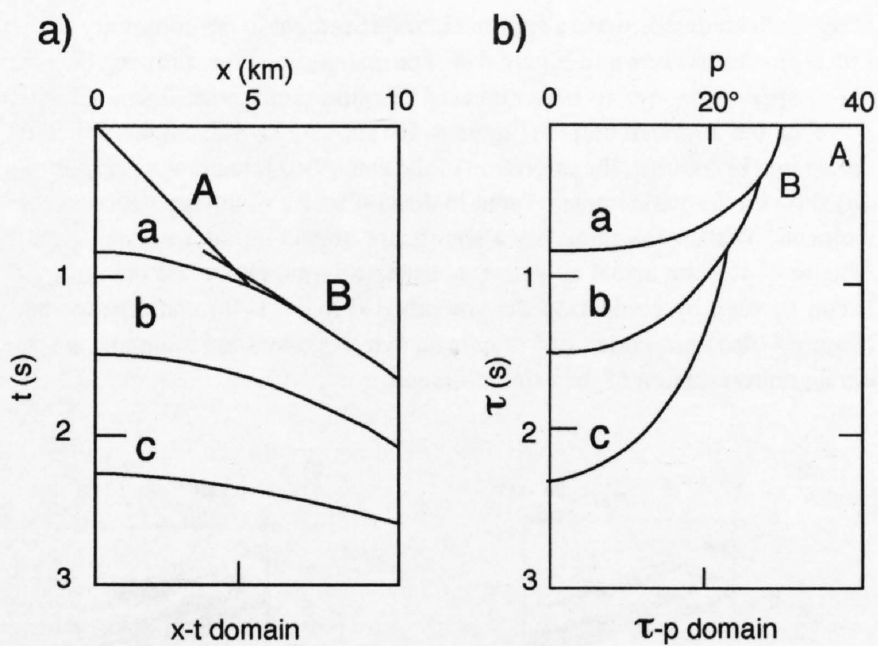
Figure 4-1:
Schematic representation and comparison between an offset gather in the (t, x) domain (shown in a) and its corresponding transformation into the (τ, p) domain (shown in b). The linear traveltime branches (A,B) are focused into points while the hyperbolic reflections (a,b,c) map into ellipses.

Figure 4-2:
Synthetic example illustrating the difference between a), the Phoenix software's method of clipping low amplitudes and b), the program WAVECLIP's technique . In both cases, the threshold was set to 50% of the maximum trace amplitude. In a) only the area-filled amplitudes are used, which tends to give a false, higher-frequency aspect to the data (wiggle lines included only for display). As an alternative, the program WAVECLIP preserves the entire positive cycle of the strong wavelets and is therefore a more accurate representation.

with distance which McMechan attributed to spatial phase shifting. Localized slant stacks can also be used to obtain 1D apparent velocity functions with the added advantage of improving the resolution (McMechan, 1984; Milkereit, 1987a; Hawman et al., 1990). This is achieved by summing together the array of localized slant stacks to produce an average τ-p gather which significantly reduces the non-coherent background noise and leads to a more precise determination of an average velocity model.

The use of localized slant stacking to reduce noise has found extensive applications on stacked seismic reflection sections as well. In one case, Harlan et al. (1984) have used localized slant stacking to filter out both random noise and subhorizontal coherent events in order to obtain a clearer representation of diffraction hyperbola for determining migration velocities. Perhaps the most wide-spread usage of localized slant stacking on stacked sections is for coherency enhancement. Kong et al. (1985) have demonstrated this on a COCORP deep-crustal profile by inverse transforming only the components of localized slant stacks which exhibit spatial coherence. Milkereit (1987b) developed a method of noise-free migration that avoids the inverse transformation by designing a filter in the τ-p domain which is used to weight a diffraction migration operator resulting in the attenuation of incoherent noise.

The separation of incoherent noise from coherent signal on stacked sections is achieved during localized slant stacking by using small enough windows to linearly approximate the observed reflectivity. This is implemented by subdividing the data into overlapping windows, each containing linear components of the reflectivity. The ensuing transformation results in a focusing of these linear reflection elements into points which then enables them to be effectively isolated.

4.2.2 Coherency enhancement

As mentioned earlier, coherency enhancement was used on the NRP 20 data for both effective presentation and for input into the automatic line drawing routine. The Phoenix algorithm COFILT was used for this purpose and is based on a modified form of the slant stacking procedure outlined in the preceding section. In general, the program operates by determining a pilot trace based on maximum coherencies measured from time windows t_w superimposed on the transformed τ-p gathers. This pilot p (t, x) trace is then weighted and added back to the original seismic trace to enhance the coherent events. Mathematically this operator p (t, x) can be expressed as:

$$p\,(t, x) = \max\,[F\,(\tau, p_j)\,_{xc})]$$

In practice, an aperture width of D = 1 km was used with t_w = 200 ms and the increment between slant stacks d is automatically set to 1. The ray parameters (p_j) were defined symmetrically to cover the maximum dip observed on the stacked profiles. To achieve a line drawing appearance, the pilot trace was added to the original seismic trace with a weight of 4:1 and then the lower amplitudes of the coherency-enhanced trace were truncated. Rather than using the basic clipping threshold offered by the Phoenix software, a program WAVECLIP was developed to remove waveforms having peak amplitudes falling below the threshold while preserving the complete wavelet of the stronger events (Figure 4-2). By imposing a threshold, the less-coherent energy represented by weaker amplitudes is suppressed. This has the advantage
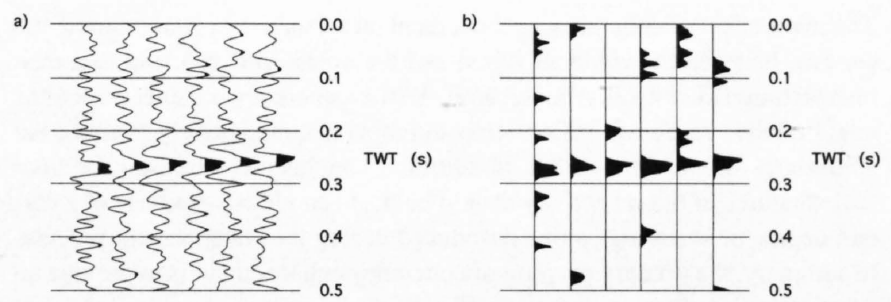
of providing a larger dynamic range for displaying the remaining contrasts as well as for providing more complete information for the line drawing routine. For the NRP 20 data the threshold was typically set between 50-60% of the average trace amplitude.

Figure 4-3 shows an example of coherency enhancement applied to the northern end of line E1 which is displayed to produce an apparent line drawing. The reflectivity shown on the standard section (Figure 4-3a) is difficult to recognize because of the condensed size of the display. An improved representation of the various reflections, particularly the weak deep events, is obtained following coherency enhancement (Figure 4-3b). The enhanced image reproduces the main reflection components in an apparent line drawing format with a minimum distortion of the original wavefield. This procedure is incapable of removing all of the noise components as evidenced by the various randomly distributed linear segments and the point scatters comprising the greyish background. The distinction between this remaining noise and signal can be made through a comparison with the original section.
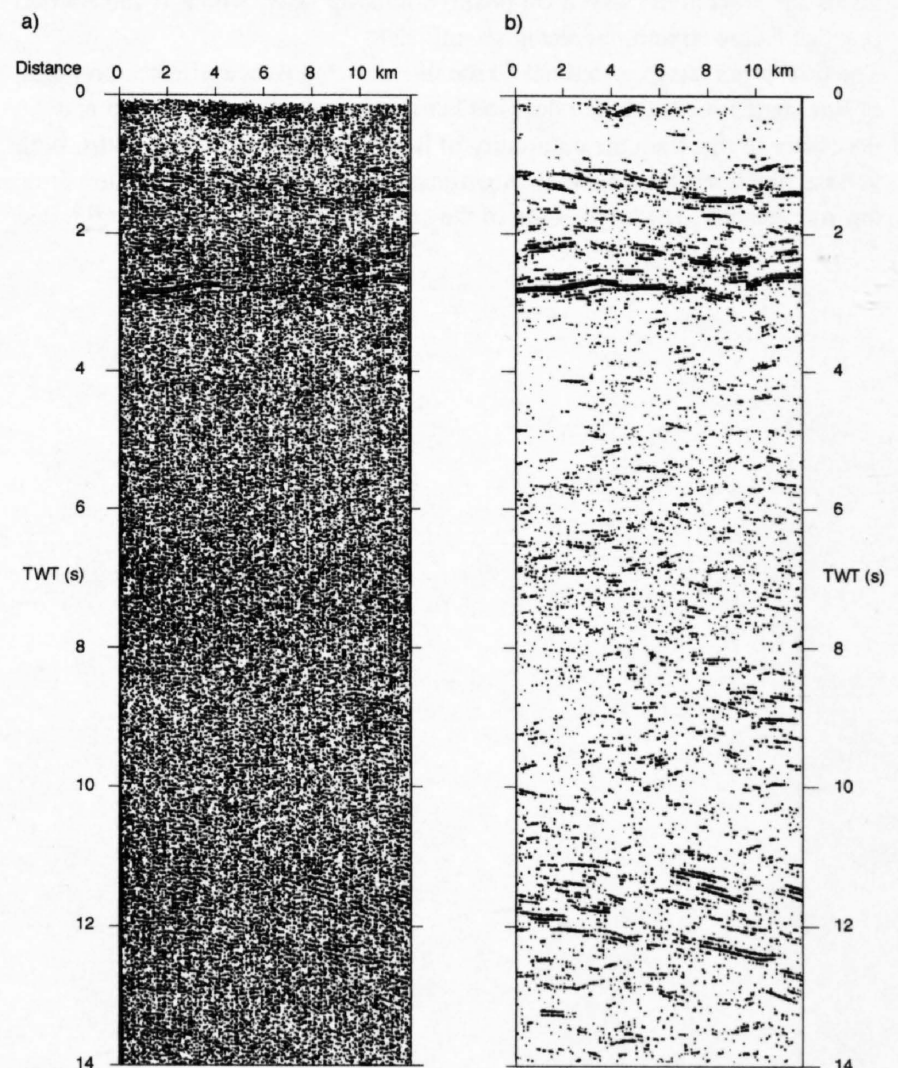

Figure 4-3:
Example of the application of coherency enhancement to produce an apparent line drawing. a) The original section is displayed in the standard area-only format resulting in a lack of sufficient contrast between the signal and noise. b) An improved image is obtained through coherency enhancement followed by the removal of the weaker, incoherent amplitudes. The program WAVECLIP was used to remove wavelets with peak amplitudes falling below 60% of the average trace amplitude.

The main effect of coherency enhancement on seismic data is to increase the contrast between the coherent signal and the noise. This can lead to a mis-interpretation if not fully understood. While coherency-enhanced sections retain relative amplitude information, attempts to quantitatively evaluate the amplitudes should be avoided. In addition, conclusions based on the fine-scale features of the reflectivity should be made cautiously because of a certain degree of smearing can be introduced during the enhancement process. In summary, the primary purpose of coherency enhancement is to provide an adequate representation of the overall reflectivity.

4.2.3 Generating the automatic line drawings

The new technique developed for automatically generating a line drawing from a stacked section (Valasek, 1992) consists of two main stages. The first involves representing the stacked data in a form which yields information on its coherence (continuity) as a function of geometry (i. e. temporal and spatial distribution). This is followed by a procedure which attempts to extract the reflections and represent them as line-segment end points. The first step is *coherency estimation* which performs a data transformation using localized slant stacks to obtain coherency measures along a symmetric range of slopes or slant lines centered across a localized group of stacked seismic traces. The second stage is referred to as *line detection* and involves incorporating data characteristics to develop a set of criteria for evaluating the transformed data for components related to the primary reflectivity. After a line drawing has been extracted from the localized slant stacks, several additional processing steps are carried out to optimize the image. These features include: *position refinement, line segment editing* and *line segment smoothing*. A new algo-rithm (AUTODRAW) was developed to carry out these steps involved in gen-erating an automatic line drawing.

The basic information needed to produce a line drawing centeres around the spatial and temporal distribution of the observed reflectivity. As has already been mentioned, localized slant stacking is a transformation which provides a quantitative estimate of these properties. The dip, temporal location, lateral extent and relative amplitudes of linear reflection elements can all be ob-tained from focused energy in this transformed domain. A feature which is unique to the slant stacking phase of AUTODRAW is that only positive am-plitudes are considered. In other words, the automatic line drawing repro-duces the refelctivity based on positive polarity only, which is the normal practice followed in interpreting seismic data.

The final processing carried out on the line drawing is an optional smoothing of line segments. If the line drawing is to be migrated, then this step may be necessary to maintain the continuity of line segments. Migration paths, both vertical and horizontal, increase significantly with increasing reflection time, dip and velocity. The application of the smoothing option results in migrated

images which demonstrate a significant improvement in the continuity of the line segments as shown in Figure 4-4. The unsmoothed line drawing (Figure 4-4a) appears by eye to be comprized of quite continuous line segments; however, the migrated output (Figure 4-4b) shows a significant disruption of the image. In contrast, the migration of the smoothed line drawing (Figure 4-4d) shows a dramatic improvement in the continuity of the repositioned line elements. While smoothing has a significant impact on the migrated output (Figure 4-4d), the actual adjustments to the original image are quite minor. It can be seen by comparing the smoothed (Figure 4-4c) and unsmoothed (Figure 4-4a) unmigrated line drawings, that this operation maintains an ac-curate representation of the original image.
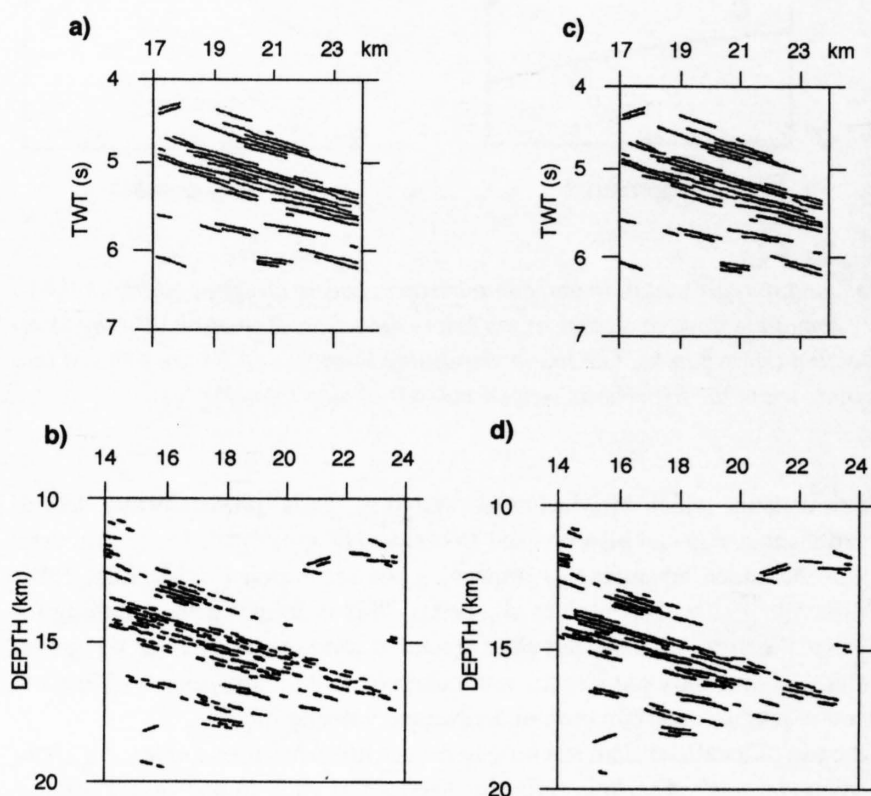
Figure 4-4
Effects of line-segment smoothing and depth migration on the final character of line drawings.
a) Unmigrated line drawing without the application of line-segment smooth-ing.
b) Depth migration of a) results in a discontinuous image due to small vari-ations in the dips of the individual line elements.
c) The same line drawing shown in a) but with line segment smoothing ap-plied.
d) Depth migration of c) results in a significantly more coherent image.

5 Seismic refraction data

5.1   Acquisition of seismic refraction data within NRP 20
5.2   Methodological considerations of 3-D crustal structure modeling by 2-D seismic methods

5.1 Acquisition of seismic refraction data within NRP 20

J. Ansorge & M. Baumann

Contents

Specially designed seismic refraction experiments were carried out as part of the international European Geotraverse Project (EGT) and the Swiss National Research Program 20 (NRP 20) concurrently to the near-vertical reflection transects. The recent measurements complement earlier surveys in the Alps and comprise four separate subprojects: The EGT Alpine section between the northern Molasse basin and the Northern Apennines, the ALP 87 profile along the northern margin of the Swiss Alps, profile AAR 80 along the crest of the Aar Massif, and a cross line AAR 90 between the Helvetic realm in the north and the Penninic domain in the south across the central Aar and Gotthard Massifs. The transects are covered by seismic refraction profiles which range in length from 100 km (AAR 90) to 550 km (EGT). Stations were equipped mostly with three-component 2Hz geophones; intervals between stations vary between 100 m and less than 2.5 km. Borehole shots provided the seismic energy. All data were digitized and are displayed as record sections with reduced time scale.

5.1.1 Data acquisition

Over the last four decades the deep crustal structure under the Alps has been investigated mainly by means of seismic refraction and wide-angle reflection profiles (see e. g. Closs and Labrouste, 1963; Giese and Prodehl, 1976; Alpine Explosion Seismology Group, 1976; Mueller et al., 1980; Deichmann et al., 1986; Thouvenot et al., 1990 and Figure 5.2-2 in Kissling et al., Chapter 5.2). These activities were strongly intensified by the implementation of the two special national and international research projects "Swiss National Research Program 20 (NRP 20)" summarized in this volume (see also Frei et al., 1989) and the "European Geotraverse Project (EGT)" (Blundell et al., 1992), respectively. Both programs began in 1983 and comprise seismic refraction, wide-angle and near-vertical reflection surveys in Switzerland. As important constituents of the EGT Project they are also closely tied to deep seismic reflection programs in the neighbourging countries France (ECORS) (Roure et al., 1990), Italy (CROP) (Roure et al., 1990) and Germany (DEKORP) (Meissner and the DEKORP Research Group, 1991).

The more recent seismic refraction and wide-angle reflection experiments were designed to investigate the lithospheric structure under the Central and Western Alps and the Northern Apennines as part of the EGT Project. This survey began in 1983 and was continued in 1986 with the main north-south profile along the EGT Central Segment parallel to the NRP 20 Eastern Traverse (Figure 5.1-1). In 1987 and 1988 followed two parallel refraction and wide-angle experiments between Jaunpass and Säntis (ALP 87) along the northern margin of the Swiss Alps and along the crest of the Aar Massif (AAR 88) with SW-NE extensions connecting the NRP 20 Eastern and Western Traverses. In addition, the explosive sources along the reflection profile of the NRP 20 Central Traverse were also used to obtain a densely covered
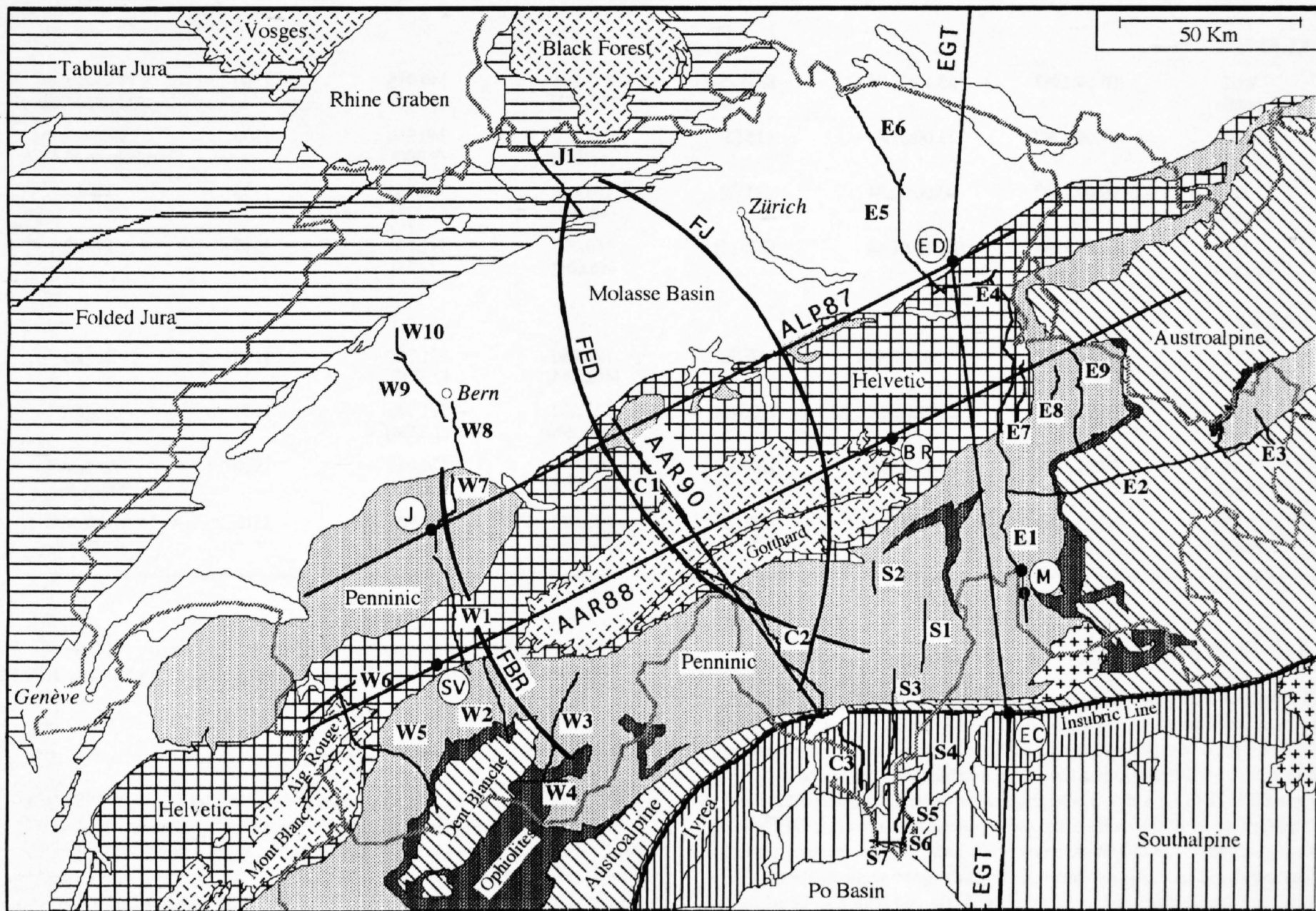

Figure 5.1-1
Tectonic map of Switzerland with locations of EGT and NRP 20 seismic refraction profiles and fans FED, FJ, FBR (thick lines) together with NRP 20 reflection traverses (thin wiggly lines). Circled letters denote shotpoints: ED, Säntis; EC, Delebio; M, Val Madris; J, Jaunpass, SV, Savièse, BR, Brigels. Thin wiggly lines with labeling C1–3, E1–9, J1, S1–7, W1–10 denote NRP 20 reflection lines.

refraction survey (AAR 90) of the uppermost crust between Flühli (Luzern), NNW and Ascona (Ticino), SSE (Figure 5.1-1).

The position and orientation of seismic refraction profiles are primarily determined by the scientific goals, by consideration of the tectonic structure of the investigated area, and – last but not least – by logistic conditions that are quite important in mountainous areas. Refraction profiles are preferably oriented parallel to the tectonic strike, e. g. profiles ALP 87 and AAR 88 in Figure 5.1-1. The lateral heterogeneities along such profiles are less pronounced and the derived structural models, therefore, better constrained (see also Ye et al., 1995). The N-S orientation of the profile across the Central Alps perpendicular to the tectonic strike is determined by the continent-wide layout of the EGT. In this case, the disadvantage of orientation perpendicular to the tectonic strike is compensated by the information derived from the set of older and new parallel-to-strike profiles (see Figure 5.2-2 in Kissling et al., Chapter 5.2). Data obtained along the EGT line provided a unique possibility to control the Alpine crustal structure derived from the large number of profiles parallel or subparallel to the main tectonic strike. The two experiments ALP 87 and AAR 88 included also fans perpendicular to the profiles at appropriate distances to record overcritical reflections from the Moho. Figure 5.1-1 shows the position of all seismic refraction and wide-angle reflection profiles and fans together with the near-vertical reflection lines organized

under the combined umbrella of NRP 20 and EGT on a tectonic map of Switzerland by Pfiffner et al. (Chapter 13.1).

Almost all recording sites were surveyed in advance or were occupied by observers acquainted with the local geology in order to select positions with the lowest possible ambient background noise. Recording equipment was mostly transported by cars. In the high moutain areas, however, many instruments had to be backpacked to the recording sites from the bottom of the valleys or from selected depots on the glaciers where they were deposited by helicopter. Borehole shots provided the seismic energy for long profiles with total charges per shot ranging from 75 kg to 2000 kg and about 200 kg per borehole at depths between 40 m and 50 m. Table 5.1-1 contains the relevant parameters of shotpoints and explosions for all profiles except AAR 90. Note that in most cases the shotpoints were not placed at the ends of the lines (Figure 5.1-1) in order to obtain a large enough reversed segment of the profile at Moho depth level. Whereas P-wave data on all profiles are reasonably good, shear-wave signals vary considerably in quality or are even absent. Shearwaves are in general poorly or often unpredictably generated by borehole shots. Therefore, it is very difficult to separate the influence of source function and crustal structure on our shear-wave data. For a more general discussion of seismic refraction and wide-angle data acquisition and interpretation see Ansorge (1989).

Table 5.1-1

Shotpoint information. Profile codes (Figure 5.1-1): EGT, European Geotraverse; ALP 87, Northern Margin of Helvetic Units; AAR 88, profile along the Aar Massif; for profile AAR 90 see Valasek (Chapter 4).

SHOT	DATE	TIME (CET)	CHARGE (kg), [number of boreholes]	Latitude N (Swiss Coord.) [degree]	Longitude E (Swiss Coord.) [degree]	ELEVATION (m)	SITE GEOLOGY
EGT:							
EC Delebio	23.09.1986	14:59:59.170	400 [2]	122.346 [46.146]	754.916 [9.445]	202	Quaternary sediments
M1 Val Madris	25.09.1986	18:00:04.500	170 [2]	140.910 [46.402]	758.723 [9.504]	1975	Weathered Bündnerschiefer
M2 Val Madris	25.09.1986	18:23:47.300	75 [1]	145.530 [46.444]	756.834 [9.481]	1828	Weathered Bündnerschiefer
ED Säntis	26.09.1986	06:00:07.859	2000 [7]	233.640 [47.240]	740.832 [9.300]	1300	Weathered subalpine Molasse
ALP87:							
ED2 Säntis	08.09.1987	23:15:02.75	1235 [5]	233.795 [47.241]	740.955 [9.300]	1300	Weathered subalpine Molasse
ED1 Säntis	09.09.1987	23:00:01.09	415 [2]	233.810 [47.241]	740.850 [9.300]	1300	Weathered subalpine Molasse
J1 Jaunpass	09.09.1987	00:00:00.94	415 [2]	161.040 [46.601]	592.165 [7.338]	1555	Flysch
J2 Jaunpass	09.09.1987	23:15:01.48	1235 [5]	160.995 [46.601]	592.190 [7.338]	1555	Flysch
AAR88:							
SV1 Savièse	07.09.1988	12:30:012.483	400 [2]	122.980 [46.2594]	591.700 [7.3319]	1100	Dogger
SV2 Savièse	09.09.1988	12:30:02.012	1200 [5]	123.000 [46.2596]	591.740 [7.3324]	1100	Dogger
BR1 Brigels	07.09.1988	13:40:00.551	1200 [5]	183.680 [46.7924]	722.985 [9.0507]	1510	Weathered Verrucano
BR2 Brigels	09.09.1988	12:40:00.000	400 [2]	183.640 [46.7938]	722.985 [9.0507]	1510	Weathered Verrucano

5.1.2 Data processing

All refraction data were recorded in analog frequency-multiplexed format on magnetic tapes mostly with MARS 66 or MARS 72 instruments (Berckhemer, 1970) equipped with Mark L4 vertical or Mark L4-3D three-component geophones with a natural frequency of 2 Hz, together with the coded radio time signal DCF 77 (77.5 kHz). The signals were digitized subsequently with a sampling rate of 400 Hz and after some processing steps (cf. Deichmann, 1984) resampled with 100 Hz. After carefully analyzing the frequency spectra of several signal and noise windows on the seismogram sections, the data were filtered with a bandpass ranging from 1 to 20 Hz and with a slope of 24 db/octave on both flanks. These final plots served then as the basis to determine the crustal structure under the profiles. Most seismogram sections of the refraction lines and fans are displayed with a reduced time scale and trace-normalized amplitudes for all traces within the shown reduced time window. The

reduction velocity is 6.00 km/s for compressional (P) waves (Figures 5.1–3, 5, 6, 8) and 3.46 km/s for shear (S)-waves (see e. g. Maurer and Ansorge, 1992).

5.1.3 Documentation of data

The structure of all EGT seismic data is described by Ansorge (1992) in the EGT Atlas as part of the complete EGT package by Blundell et al. (1992). All refraction and wide-angle data acquired within the EGT Project have been collected in a series of eight Open-File Reports available separately from the EGT Atlas. They contain all technical and logistic information besides the seismograms plotted as record sections in the same format. In addition, all the data is available on magnetic tape from the individual compilation groups at the participating institutions. Three of these reports pertain to the Alpine area traversed by the EGT (Aichroth et al., 1990; Buness, 1990;

Maistrello et al., 1991). Therefore, only those EGT seismic data covering the Central Alps are reproduced in the NRP 20 Atlas. All other seismic refraction and wide-angle reflection data described and shown in this chapter (ALP 87, AAR 88, AAR 90) as well as older digital data (e. g. ALP 75 and SUDALP 77, Figure 5.2-2 in Kissling et al., Chapter 5.2) are included in the Data Bank of the Seismic Refraction Group at the Institute of Geophysics, ETH Zürich (Egger 1991).

Addresses for the Open-File Reports:

Aichroth et al., 1990: C. Prodehl, Geophysical Institute, University of Karlsruhe, Hertzstrasse 16, D-76187 Karlsruhe, Germany

Buness, 1990: P. Giese, Institute of Geology and Geophysics (WE1), Fachbereich Geowissenschaften, Free University of Berlin, Haus B, Malteserstrasse 74-100, D-12249 Berlin, Germany

Maistrello et al., 1991: M. Maistrello, Istituto di Ricerca sul Rischio Sismico CNR-IRRS, Via Bassini 15, I-20133 Milano, Italy.

5.1.4 Individual profiles

EGT Central Alpine Section – NRP 20 Eastern Traverse

From north to south the Alpine segment of the EGT crosses several major teconic units: The Molasse Basin, the Helvetic nappes, the Penninic nappes, the Southern Alps, the Po Basin, the Northern Apennines and the northern
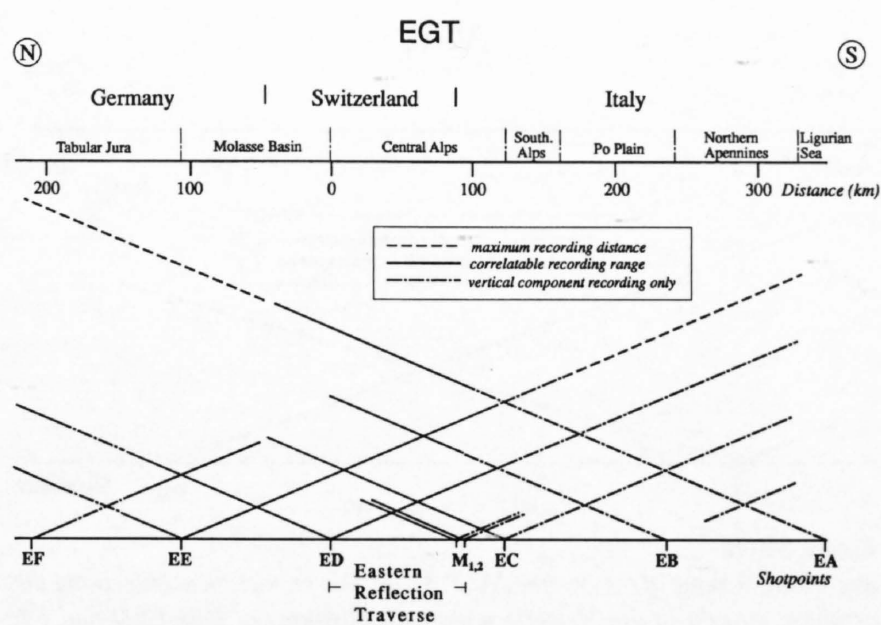
Figure 5.1-2
Recording scheme of the EGT Alpine Section with distance range of seismic refraction profiles. M 1, 2 denote the two smaller shots fired for the seismic reflection survey of NRP 20 (see Figure 5.1-1). EA to EF are shotpoints of the EGT; ED, Säntis; EC, Delebio. See also shotpoint information in Table 5.1-1.
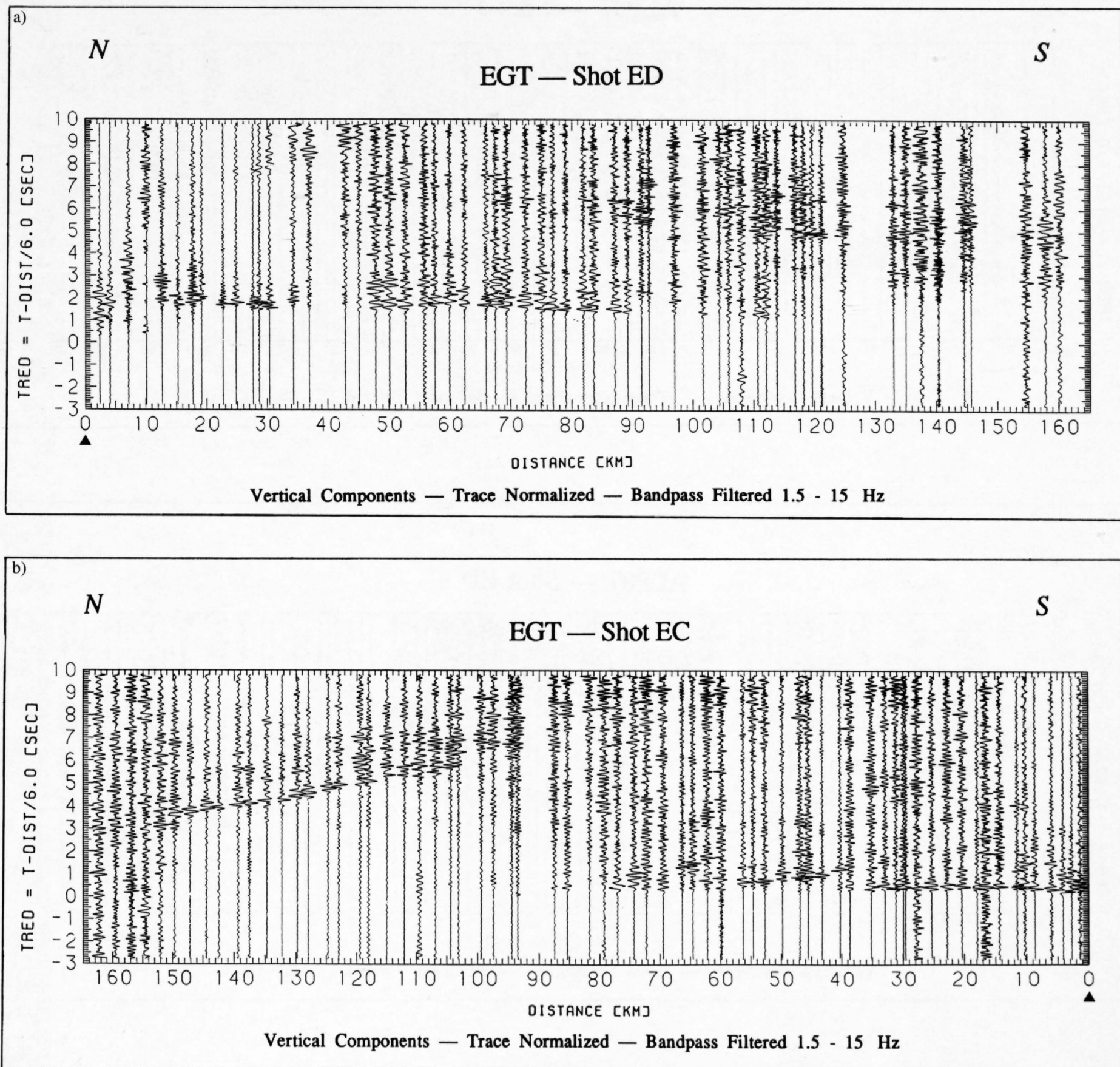
Figure 5.1-3
a) Seismogram section for the vertical component of the EGT profile, shotpoint ED (Säntis) to the south with reduced traveltime (reduction velocity 6 km/s).
b) Seismogram section for the vertical component of the EGT profile, shotpoint EC (Delebio) to the north with reduced traveltime (reduction velocity 6 km/s).
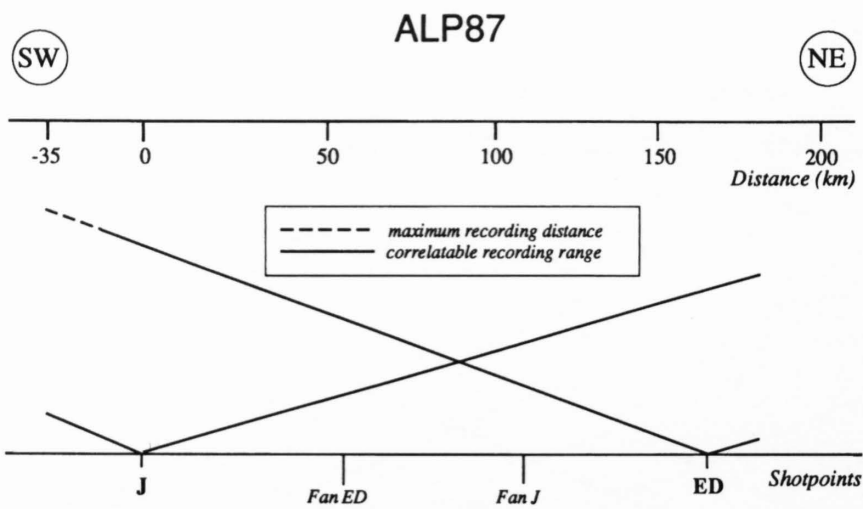
27

ALP87

Figure 5.1-4a
Recording scheme of the reversed ALP 87 seismic refraction profile along the northern margin of the Helvetic units with positions of fans FED and FJ. Shotpoints: J, Jaunpass; ED, Säntis.
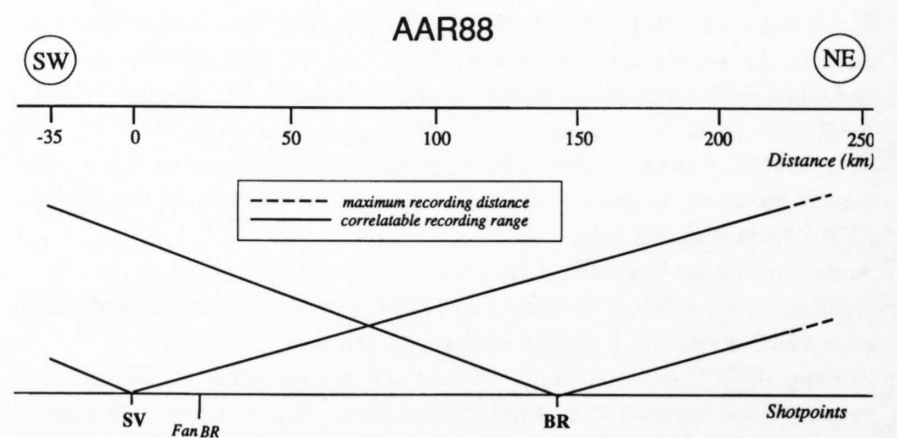
AAR88

Figure 5.1-4b
Recording scheme of the reversed AAR 88 seismic refraction profile along the Aar Massif with position of fan FBR. Shotpoints: SV Savièse; BR Brigels.

a)

SW   **ALP87 — Shot J**   **NE**

Vertical Components — Trace Normalized — Bandpass Filtered 1 - 20 Hz

b)

SW   **ALP87 — Shot ED**   **NE**

Vertical Components — Trace Normalized — Bandpass Filtered 1 - 20 Hz

Figure 5.1-5
a) Seismogram section for the vertical component of the ALP 87 profile along the northern margin of the Helvetic units. Shotpoint J (Jaunpass) to the northeast with reduced traveltime (reduction velocity 6 km/s).
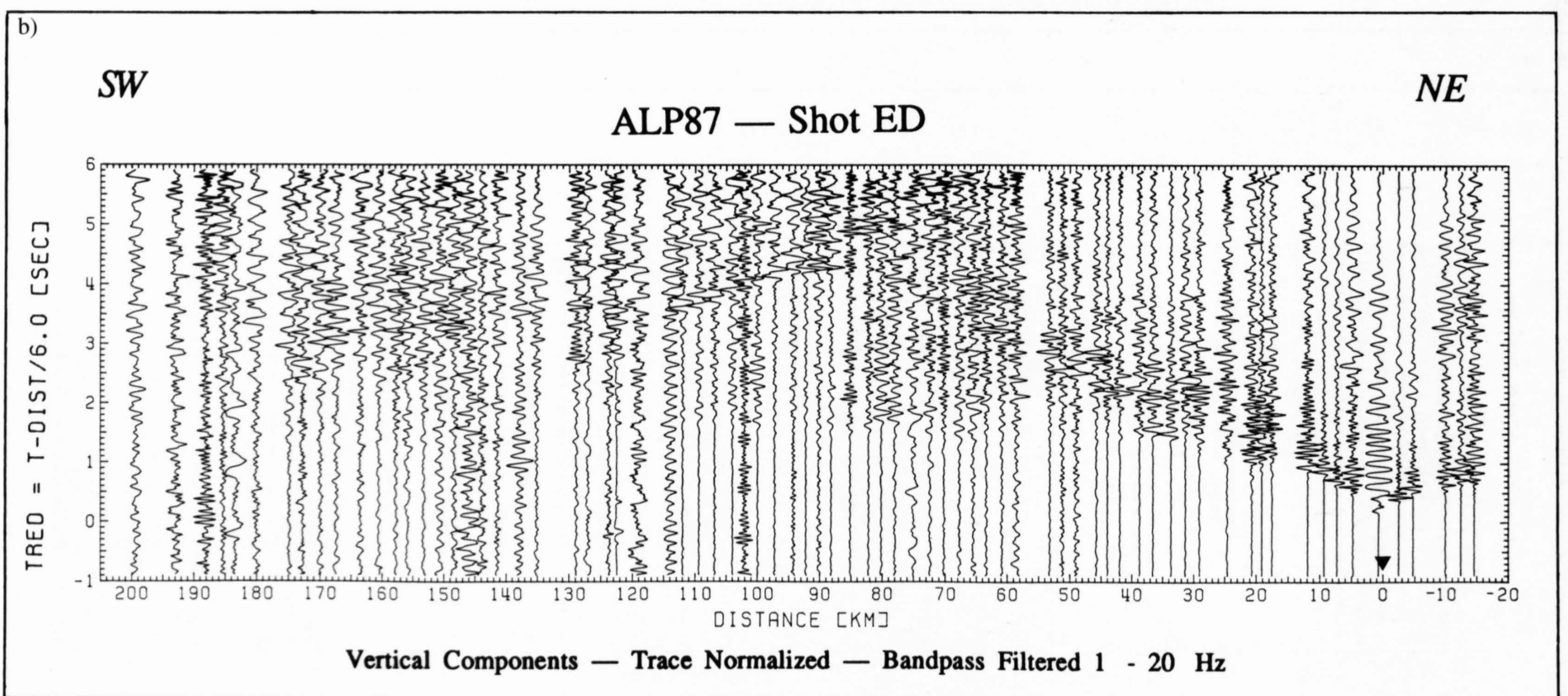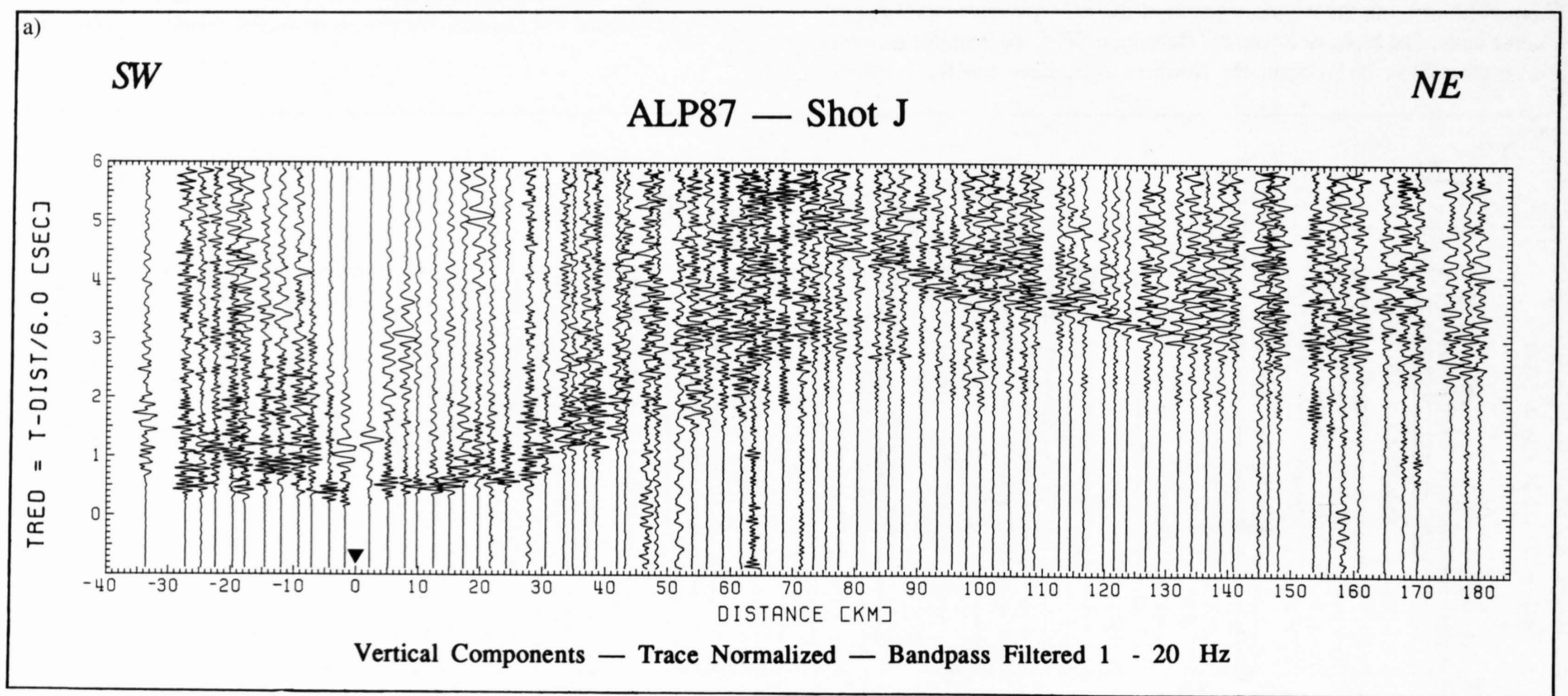b) Seismogram section for the vertical component of the ALP 87 profile along the northern margin of the Helvetic units. Shotpoint ED (Säntis) to the southwest with reduced traveltime (reduction velocity 6 km/s).

Ligurian Sea. Figure 5.1-2 shows the distances over which the individual shots in the N-S oriented Alpine range of the EGT were successfully recorded and which sections are covered with three-component recordings. Shotpoints (Figure 5.1-1) were located at the northern margin of the Helvetic overthrust within weathered Subalpine Molasse (ED, shotpoint Säntis) and in Quaternary sediments of the Adda valley a few hundred meters south of the Insubric Line (EC, shotpoint Delebio). In addition shots M1 and M2 (Figure 5.1-1) of the NRP 20 near-vertical reflection program on the Eastern Traverse located in weathered Bündnerschiefer were recorded on the refraction profile beyond the spread length of the reflection survey. The average spacing between recording stations was 2.5 km. Vertical-component record sections of profiles from shots ED to the south and EC to the north are displayed in Figures 5.1-3a and 5.1-3b. Clear first and later arrivals of phases refracted and reflected in the Alpine crust appear on both sections to distances of 320 km and 160 km, respectively. The different character and number of correlated phases indicates strong lateral variations of structure along the north-south profile. For a full account of the experiment and the complete set of data see EUGEMI Working Group (1990) and Aichroth et al. (1990). For interpretations and further references the reader is referred to ETH Working Group on Deep Seismic Profiling (1991), Holliger and Kissling (1991), Valasek et al. (1991), Aichroth et al. (1992), Buness (1992), Prodehl and Aichroth (1992), Valasek (1992), Ye (1992) and Ye et al. (1995).

ALP 87 – Profile along the Northern Margin of Helvetic Units

Profile ALP 87 connects the Eastern and Western NRP 20 near-vertical reflection profiles between shotpoints Jaunpass (J) and Säntis (ED) (Figure 5.1-1). Shotpoint Säntis has the same location as on the EGT N-S profile. Shotpoint Jaunpass is located in weathered Flysch sediments of the Simmen nappe. The central and eastern part of the profile runs along the northern edge of the Helvetic nappes. The western part lies on the Penninic nappes north of the Helvetic realm (Figure 5.1-1). Figure 5.1-4a shows the recording scheme with distances to about 180 km in both directions and an average station
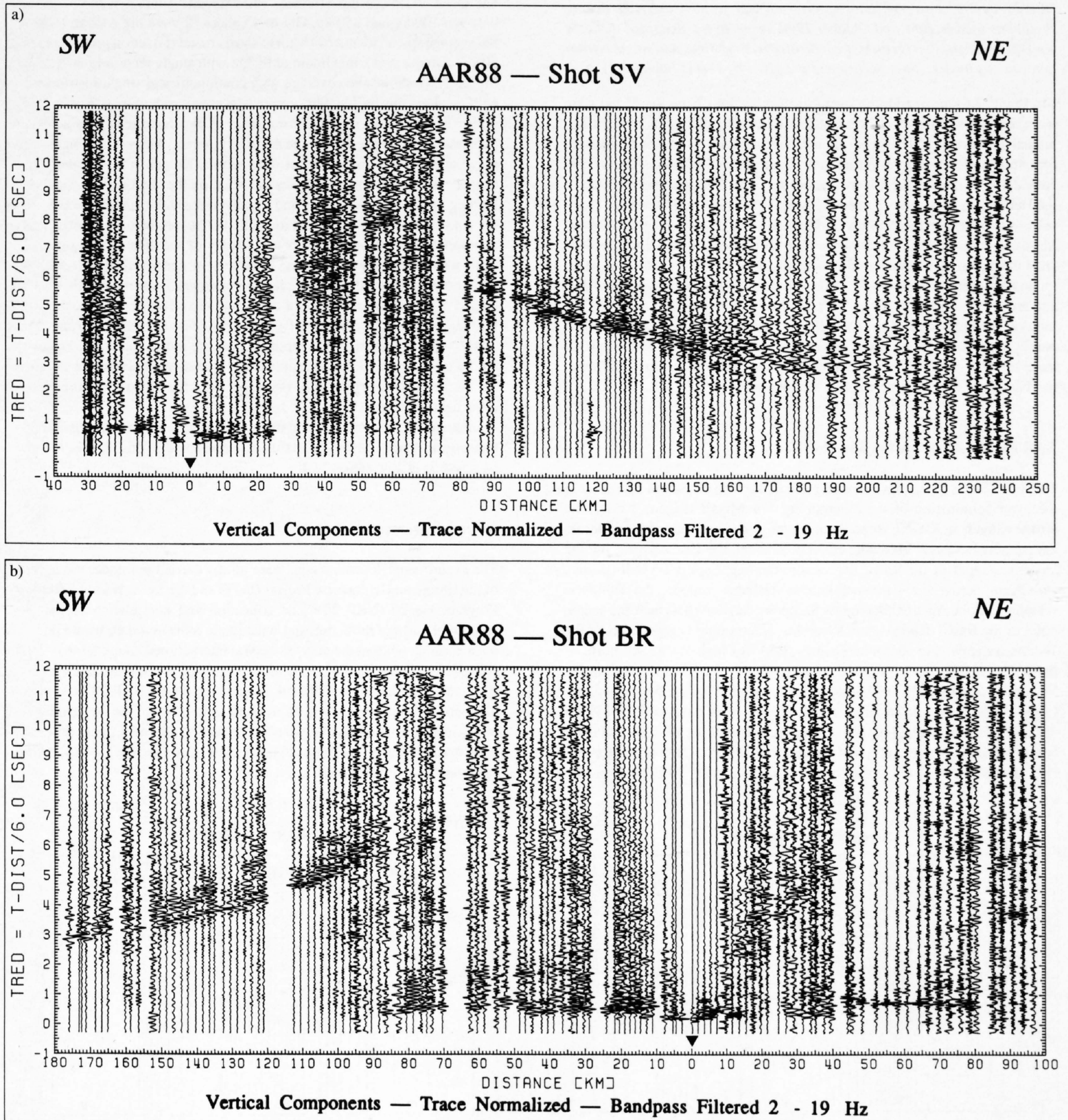

Figure 5.1-6

a) Seismogram section for the vertical component of the AAR 88 profile along the Aar Massif. Shotpoint SV (Savièse) to the northeast with reduced traveltime (reduction velocity 6 km/s).

b) Seismogram section for the vertical component of the AAR 88 profile along the Aar Massif. Shotpoint BR (Brigels) to the southwest with reduced traveltime (reduction velocity 6 km/s).
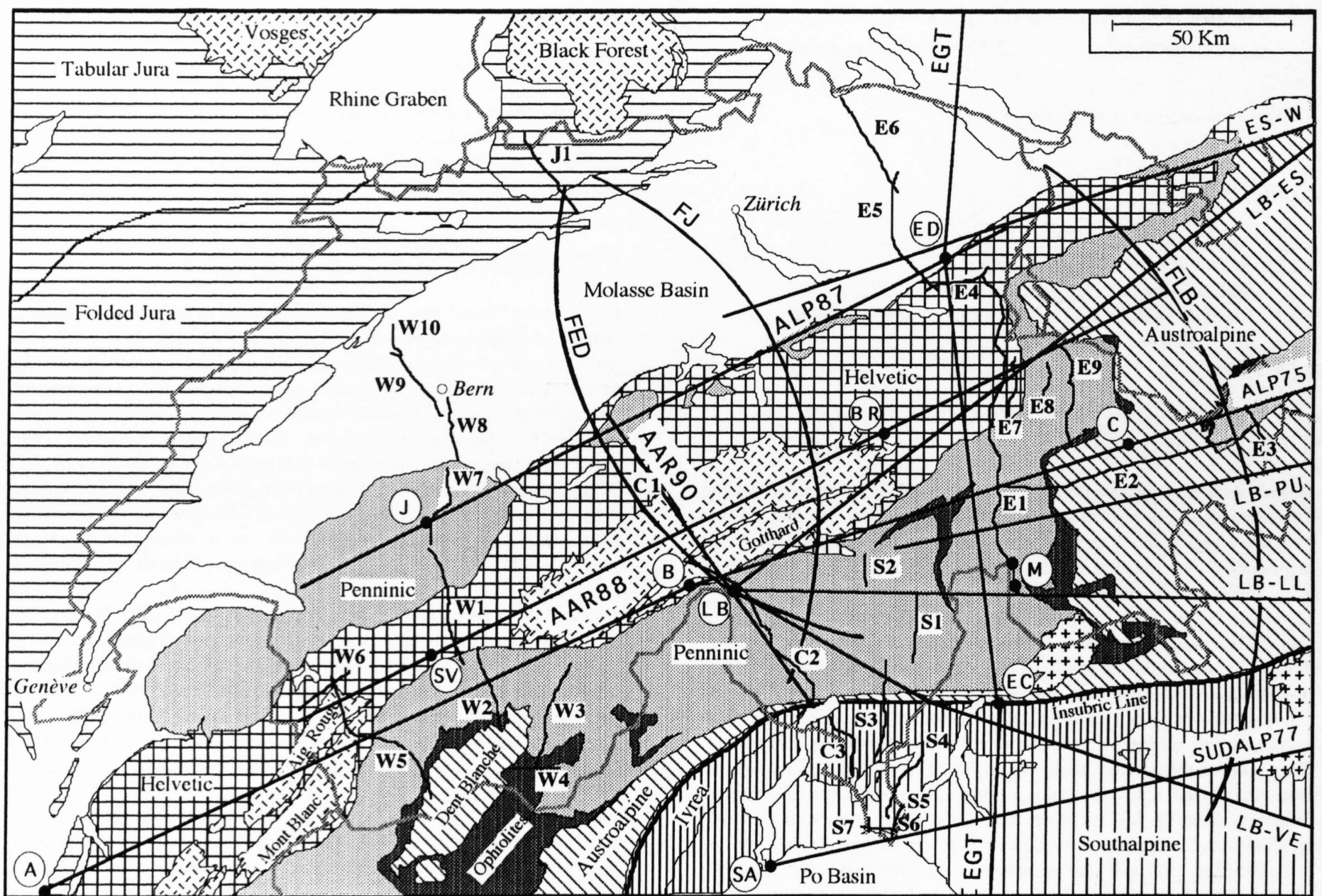
Figure 5.2-2
Generalized tectonic map of the Central and Western Alps (after Pfiffner et al., Chapter 13.1) showing the location of the European Geotraverse (EGT) and the seismic surveys reviewed in this study. Seismic refraction profiles: SUDALP 77, ALP 75, ALP 87, AAR 88, AAR 90, ES-W, LB-ES, LB-PU, LB-LL, LB-VE, EGT; wide-angle reflection fan profiles: FED, FJ, FLB; NRP 20 near-vertical reflection profiles (thin crooked lines): C1 to C3, E1 to E9, J1, S1 to S7, W1 to W10. Circled letters denote shotpoints (solid black dots).

5.2.3 Identification of seismic phases

Modeling of structures based on seismic data requires the identification and correlation of reflected and refracted phases observed on different seismic profiles. In densely networked near-vertical reflection profiles the imaged structural elements geometrically overlap and the correlation of seismic signals along and between profiles is possible for almost any structure. In contrast, for geometrical reasons (necessary length of profiles to reach the deep crust) structural elements imaged by loosely networked refraction and wide-angle reflection profiling are often separated. In this case, the correlation of separate structural elements depends entirely on the identification of seismic signals attributed to specific structural features, such as the Moho. For a thorough discussion of seismic phases most commonly observed in refraction and wide-angle reflection profiles the reader is referred to Giese and Prodehl, (1976). Normally, seismogram sections of refraction lines are displayed with trace-normalized amplitudes and a reduced time scale (Figures 5.2-5 and 5.2-6) (Ansorge, 1989; Ansorge, and Baumann, section 5.1). The reduction velocity is 6.0 km/s for crustal data. Here, we concentrate on the prominent phases observed in Alpine longitudinal refraction profiles, such as the ALP 87 profile in the Northern Calcareous Alps (Maurer and Ansorge, 1992) and the AAR 88 profile in the Aar massif (Baumann, 1994).

The first arrivals in the distance range between the shotpoints and 110 km for the ALP 87 profile (Figure 5.2-5) and 60 km for the AAR 88 profile (Figure 5.2-6) image the sediments and shallow structure of the basement near the shotpoints. These wavelets either belong to seismic phases propagating through the sedimentary cover (shotpoints J and ED in Figure 5.2-5) and/or to the Pg phase (shotpoint BR in Figure 5.2-6) travelling through the crystalline basement. For profiles with short shotpoint spacing, inversion of the Pg travel times by the Wiechert-Herglotz method and 2-D ray tracing (Ye, 1992; Kuhn, 1993; Ye et al., 1995) reveal the detailed velocity structure of the basement to a depth of several kilometers (shown in Figure 5.2-7 for profile AAR 90).

The most prominent seismic phases in all Alpine longitudinal profiles are those coming from the crust-mantle boundary or Moho. Wide-angle reflections from the Moho (PMP) are very well observed along all examples of longitudinal refraction profiles shown in Figures 5.2-5 and 5.2-6. Refracted waves from be-

neath the Moho (Pn) on Alpine longitudinal profiles always have much smaller amplitudes than their corresponding PMP phases but in most cases are still recognizable as first arrivals at distances beyond 130 km to 150 km (see, e. g., Figures 5.2-5 and 5.2-6). As the strongest and clearest seismic phases in all record sections, Pg, PMP, and Pn phases can hardly be mistaken, although Moho topography and velocity variation lead to different appearance (compare shape of PMP and Pn phases from shotpoints J and ED, Figure 5.2-5).

Reflections and refractions from the crust-mantle boundary normally are recorded over distance ranges of 100 km or more (see, e. g., Figures 5.2-5 and 5.2-6) and lead to continuously illuminated reflectors and refractors of considerable length, often well-constrained by cross-profile data (Figure 5.2-2). As a result, the Moho and its topography are the best known deep lithospheric structures in the Alps (Kissling, 1993). Due to their characteristic appearance in all refraction seismic record sections, PMP and Pn phases serve as guidelines for the possible identification and interpretation of other seismic phases corresponding to mid- and deep-crustal structure, such as the $P_I P$ and $P_b P$ phases (Figure 5.2-6). Because of its dominant corresponding seismic phases PMP and Pn, the Moho topography serves as key information for further modeling of internal crustal structure.

If the Moho is known from PMP and Pn phases, a corresponding average crustal velocity and a sub-Moho velocity may also be derived. The former may be used for in-line migration of near-vertical reflection data (Holliger, 1991) and serve as independent constraint for crustal structure modeling when interpreting less pronounced, discontinuous phases such as $P_I P$ (Figure 5.2-6).

5.2.4 Uncertainty estimates for 2-D profiling and 3-D migration

Estimations of uncertainty for a particular structural element or of reliablity for an entire seismic model have been a research topic for a number of years (Ansorge et al., 1982) and are still hard to obtain. This situation is a result of the employed 2-D modeling procedure which is based on several assumptions and approximations that often may not be justified and cannot be checked.
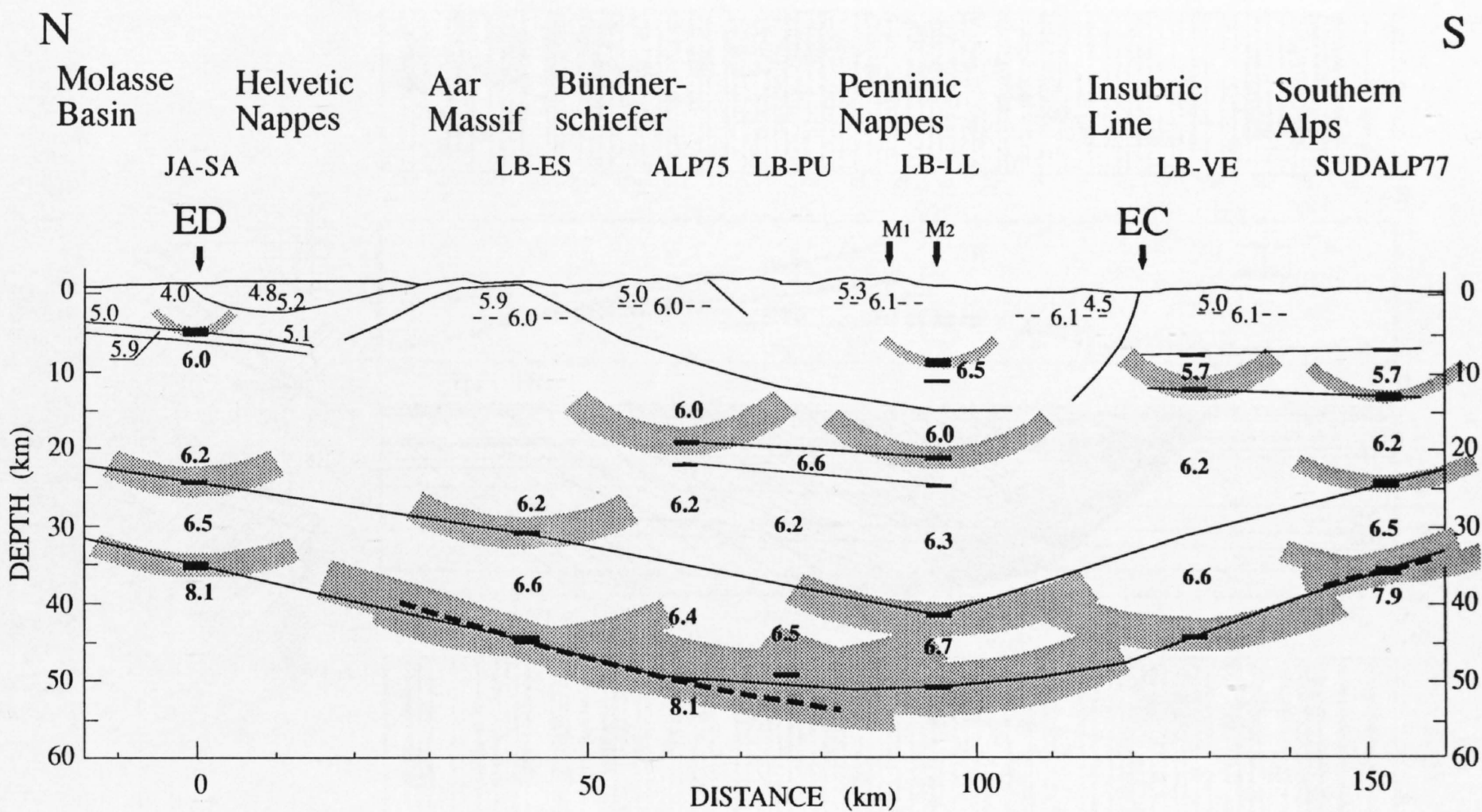
Molasse Basin   Helvetic Nappes   Aar Massif   Bündner-schiefer   Penninic Nappes   Insubric Line   Southern Alps

JA-SA   LB-ES   ALP75   LB-PU   LB-LL   LB-VE   SUDALP77

ED   M1   M2   EC

Figure 5.2-3

Initial crustal cross-section along the EGT Alpine transect based on reliable information extracted from seismic-refraction profiles parallel to the tectonic strike (perpendicular to the cross-section). The shaded areas mark uncertainty of structural elements as a result of interpretation errors and out-of-plane migration (see also Figure 5.2-1). The near-surface structure was determined from seismic data sampled along the EGT by 2-D ray tracing. Velocities are in km/s. Modified from Ye (1992).

Swabian Jura   Molasse Basin   Helvetic Aar Nappes Massif   Penninic Nappes IL   Southern Alps   Po Plain   Northern Apennines   Ligurian Sea

EF   EE   ED   M   EC   EB   EA

EGT

a

N   S

EF   EE   ED   M EC   EB   EA
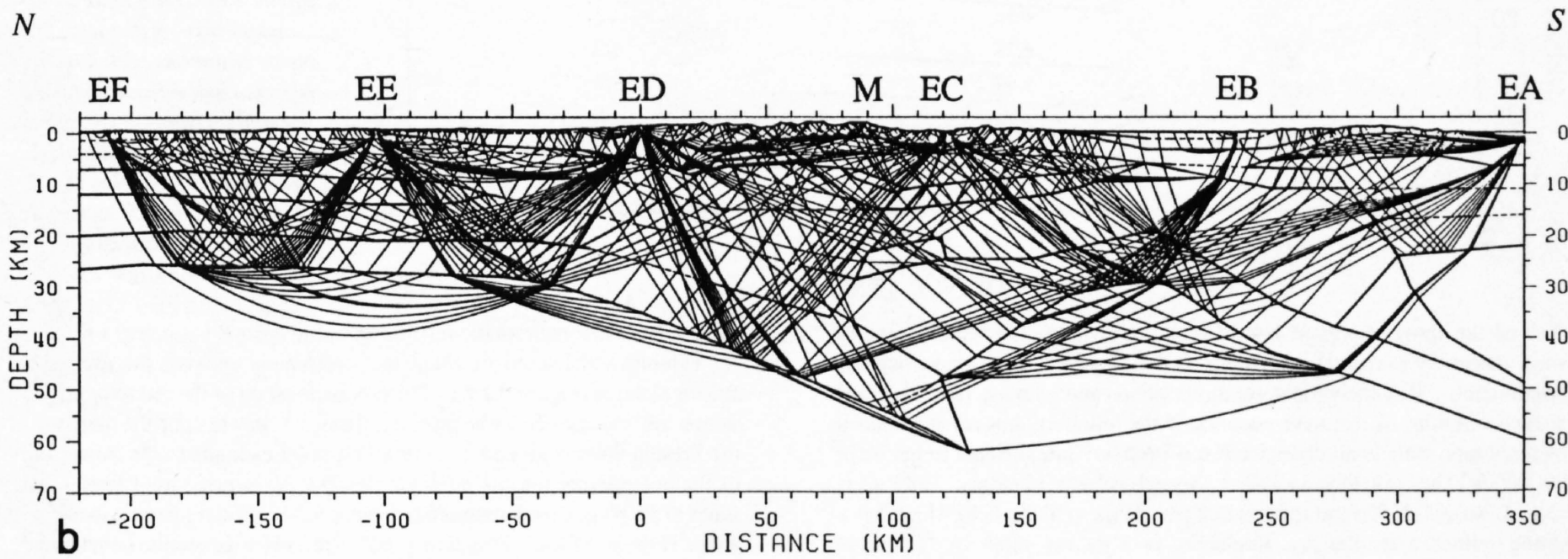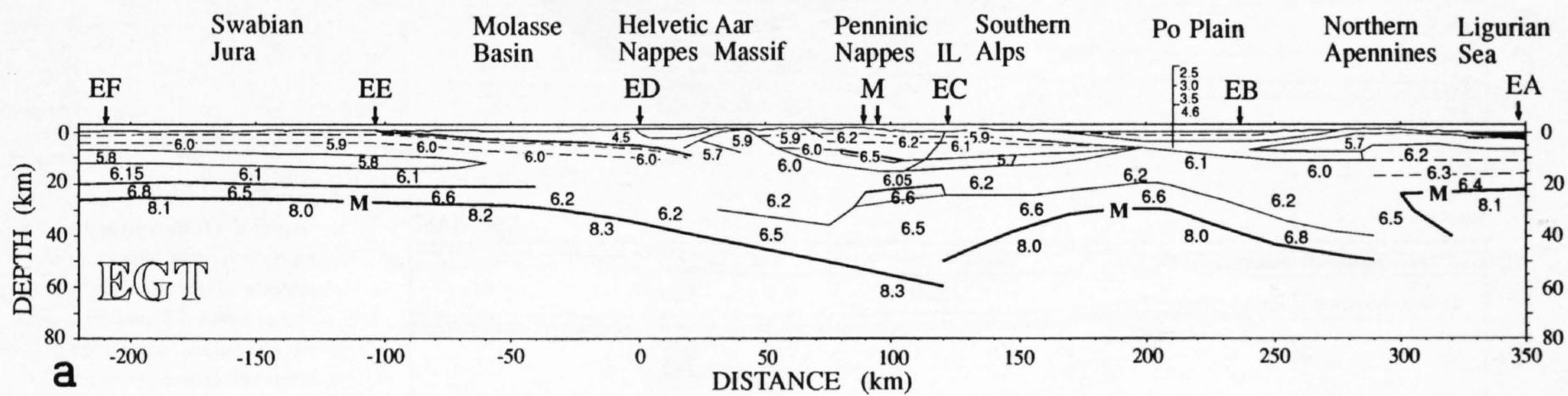
b

Figure 5.2-4

a: Final model of crustal cross-section along the EGT between the Swabian Jura and the Ligurian Sea (Ye et al., 1995) with derived distribution of P-wave velocities in km/s.

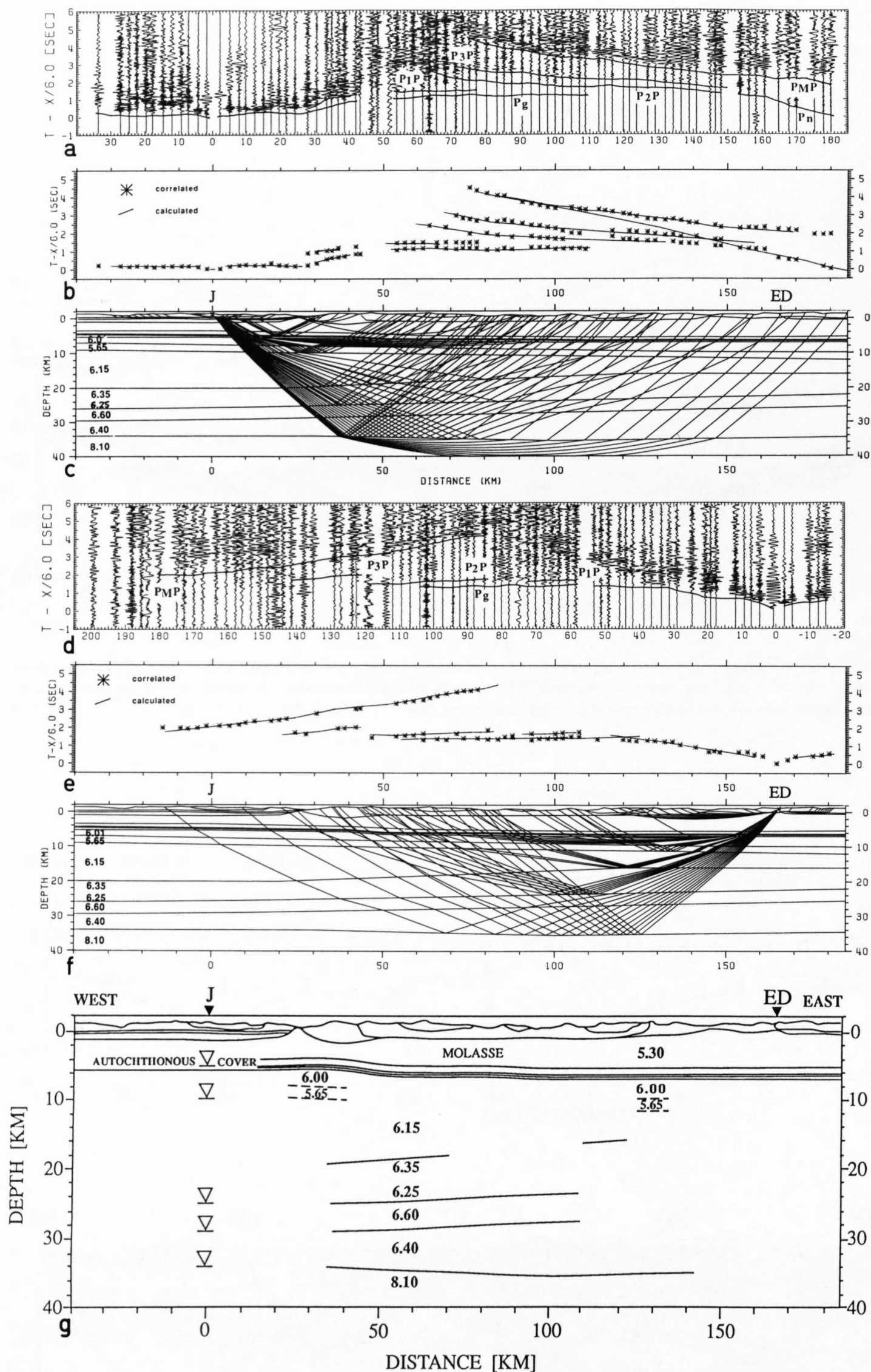b: Crustal cross-section as in (a) with ray coverage.

Figure 5.2-5
a – c and d – f: Record sections with correlated phases, comparison of observed/correlated and computed traveltimes, and ray diagrams through the derived velocity-depth model for the reversed ALP 87 refraction profile J-ED (see Figure 5.2-2).
g: Crustal cross-section with segments of interfaces covered by reflected and refracted phases in c and f. Triangles indicate reflecting horizons identified on a short vertical reflection line close to shotpoint J. Uncertain interfaces are dashed (after Maurer and Ansorge, 1992).

One of the most important approximations involves the replacement of wave theory by (simpler) ray theory as the so-called "high-frequency approximation". Ray-theoretical solutions better approximate true high-frequency solutions of the wave equation if the infinitely thin ray is replaced by a ray tube with small diameter that is inversely proportional to the wave frequency. This ray tube is called Fresnel volume (Lindsey, 1989; Červený & Soares, 1992) and reflects that part of the velocity field which has a strong influence on the ray. Replacing rays by ray tubes or "fat rays" (Woodward, 1989) in seismic refraction modeling results in a reduction of the otherwise unrealistically high theoretical resolution and in smoother velocity models.

Routinely filtered seismic refraction signals (Deichmann et al., 1986) are of limited frequency content. Therefore, Fresnel volume calculations may be restricted to the dominating frequency in the wavelets without much loss of ac-

curacy. For a monochromatic seismic wave the Fresnel volume of a refracted ray exhibits a characteristic shape and completely encloses the imaged refractor element (Figure 5.2-8a). The precise location of the refractor element within this volume cannot be resolved. Thus, we may assume the diameter of the Fresnel volume around a ray as a first-order estimate of the (lower limit of the) uncertainty for this refractor element. A comparison of Fresnel volumes of Pn phases for longitudinal (Figure 5.2-8b) and transverse to tectonic strike (Figure 5.2-8c) refraction profiles reveals a generally larger uncertainty for model elements obtained by transverse profiles (Baumann, 1994). Thus, Fresnel volume calculations allow qualitative uncertainty estimates for specific refractor and reflector elements.

Fresnel volume calculations such as the ones shown in Figure 5.2-8 are, however, no quantitative measure of the uncertainty of particular reflector and refractor elements in a 3-D model mainly for two reasons:
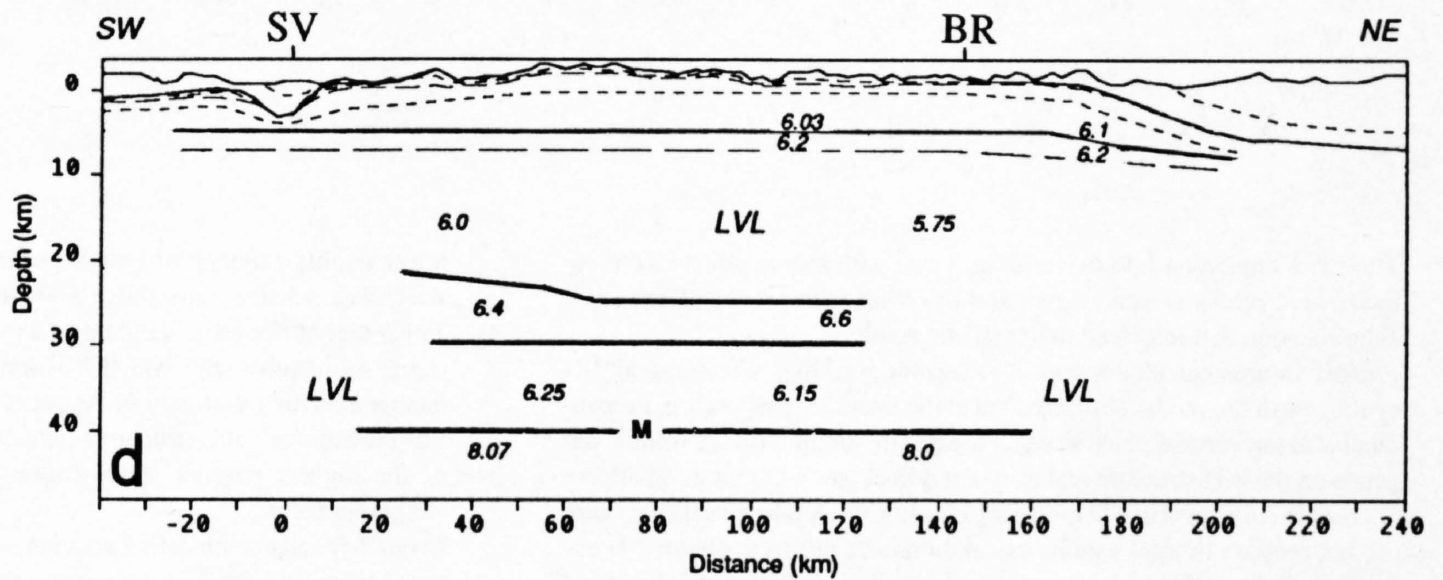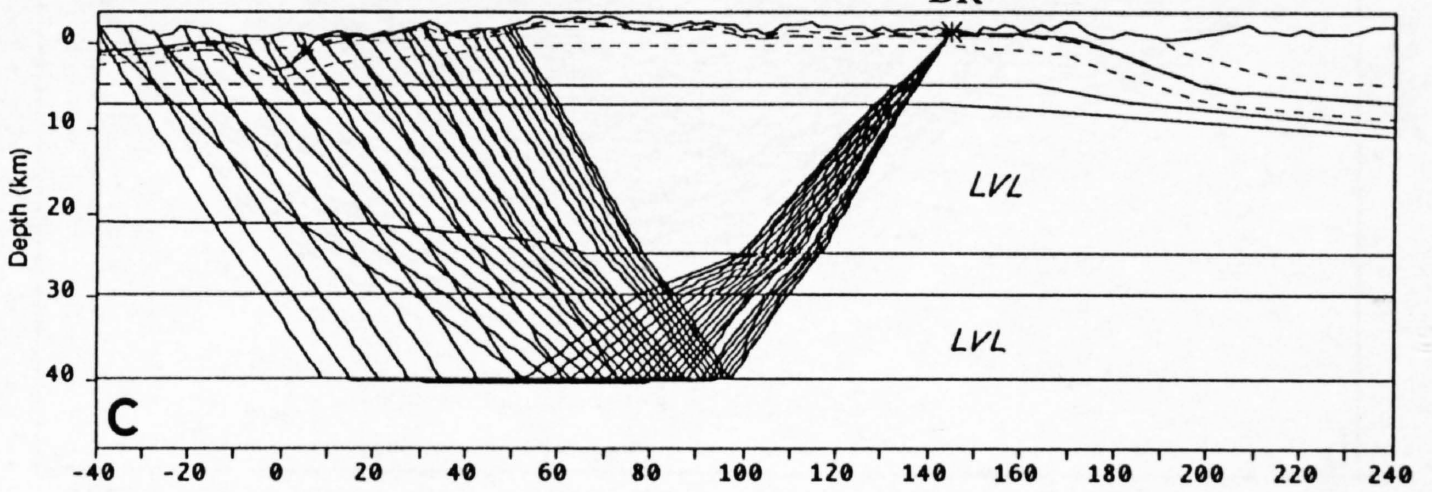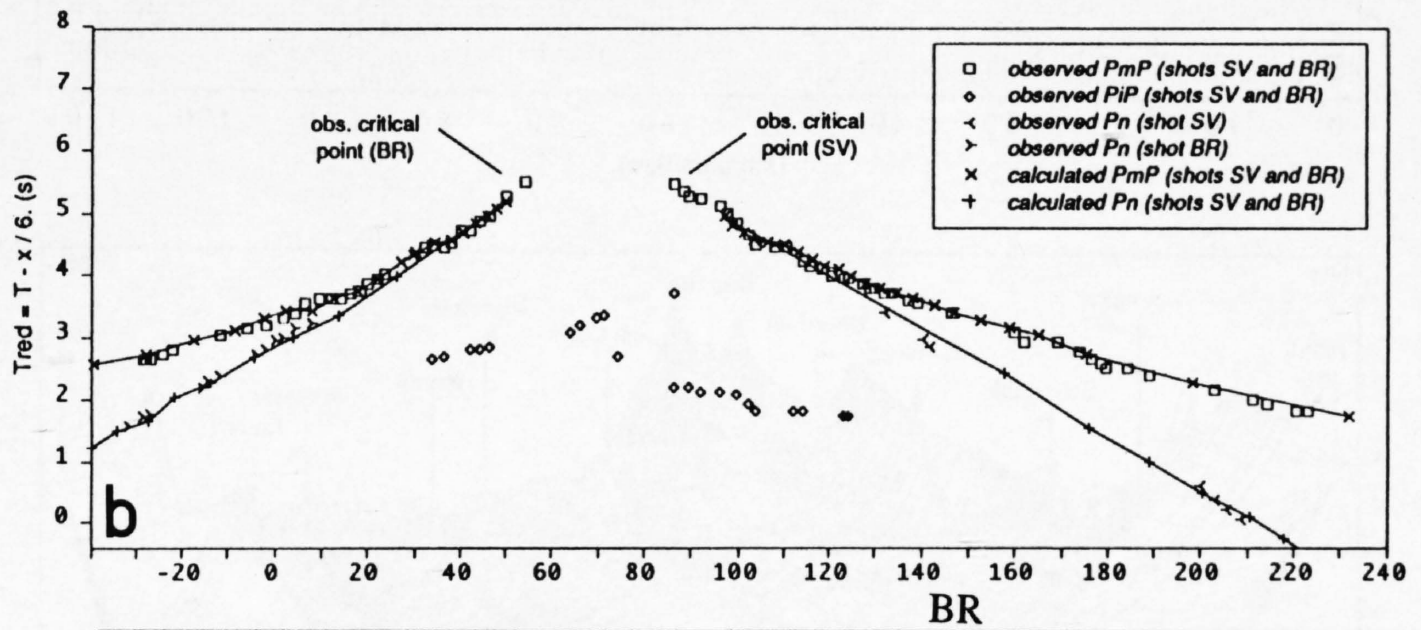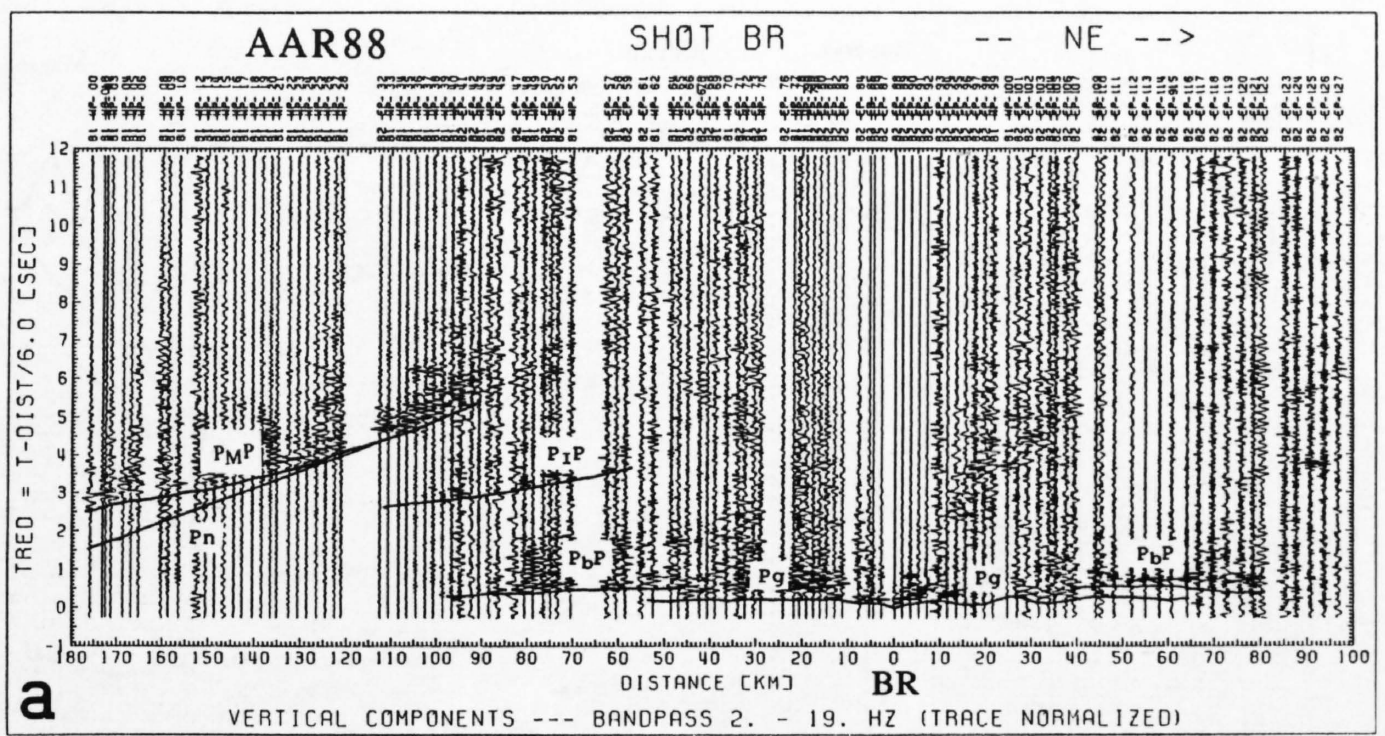
Figure 5.2-6

a – c: Record section with correlated phases for profile BR to the southwest, comparison of observed/correlated and computed traveltimes, and ray diagram through derived velocity-depth model for the reversed AAR 88 profile SV-BR (see Figure 5.2-2); (b) includes observed and calculated traveltimes for shot SV to northeast.

d: Crustal cross-section with segments of interfaces covered by reflected and refracted phases. Short dashed lines indicate change of velocity gradient; long dashed line indicates top of upper crustal low-velocity zone (after Baumann, 1994).

35
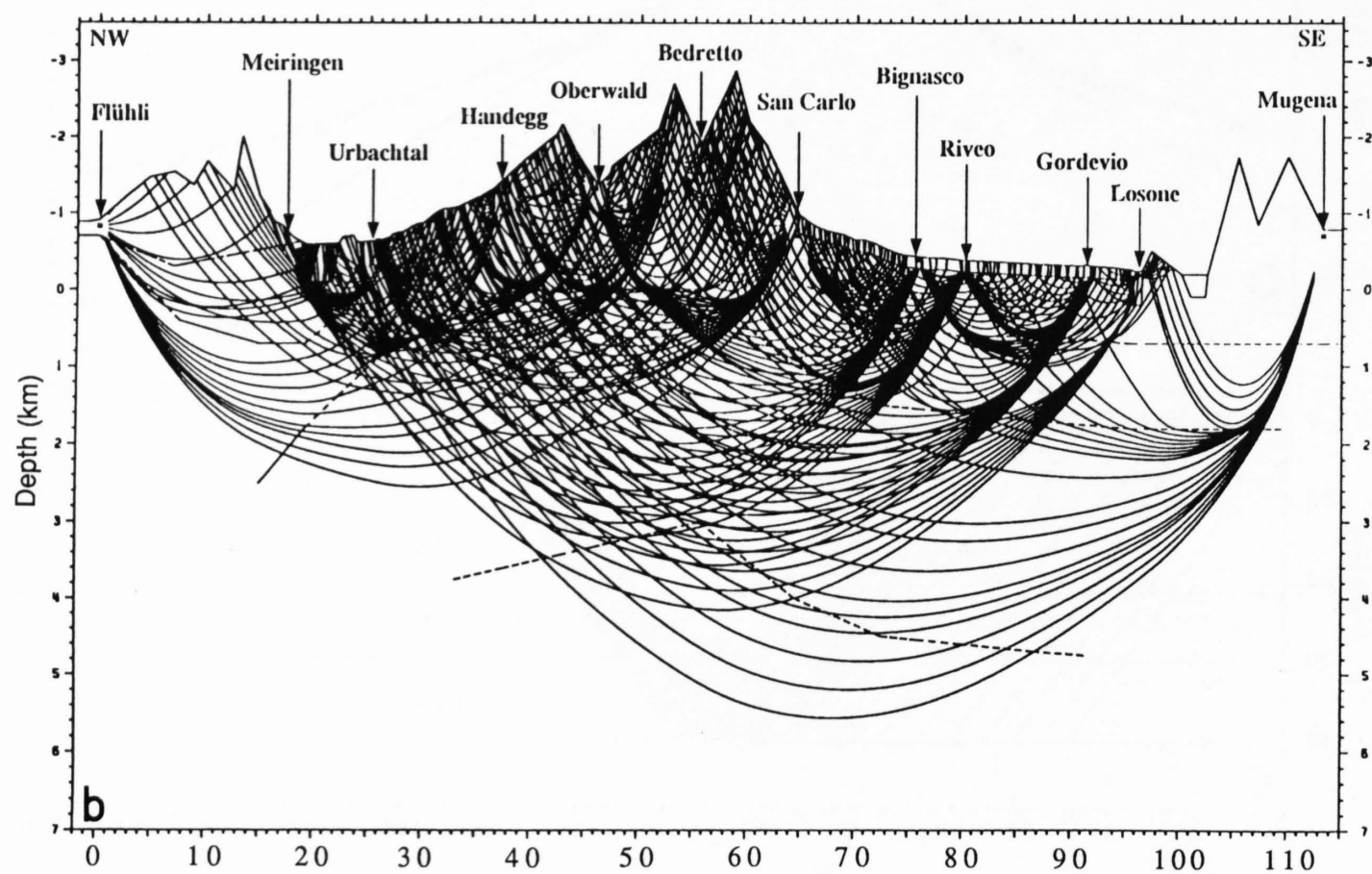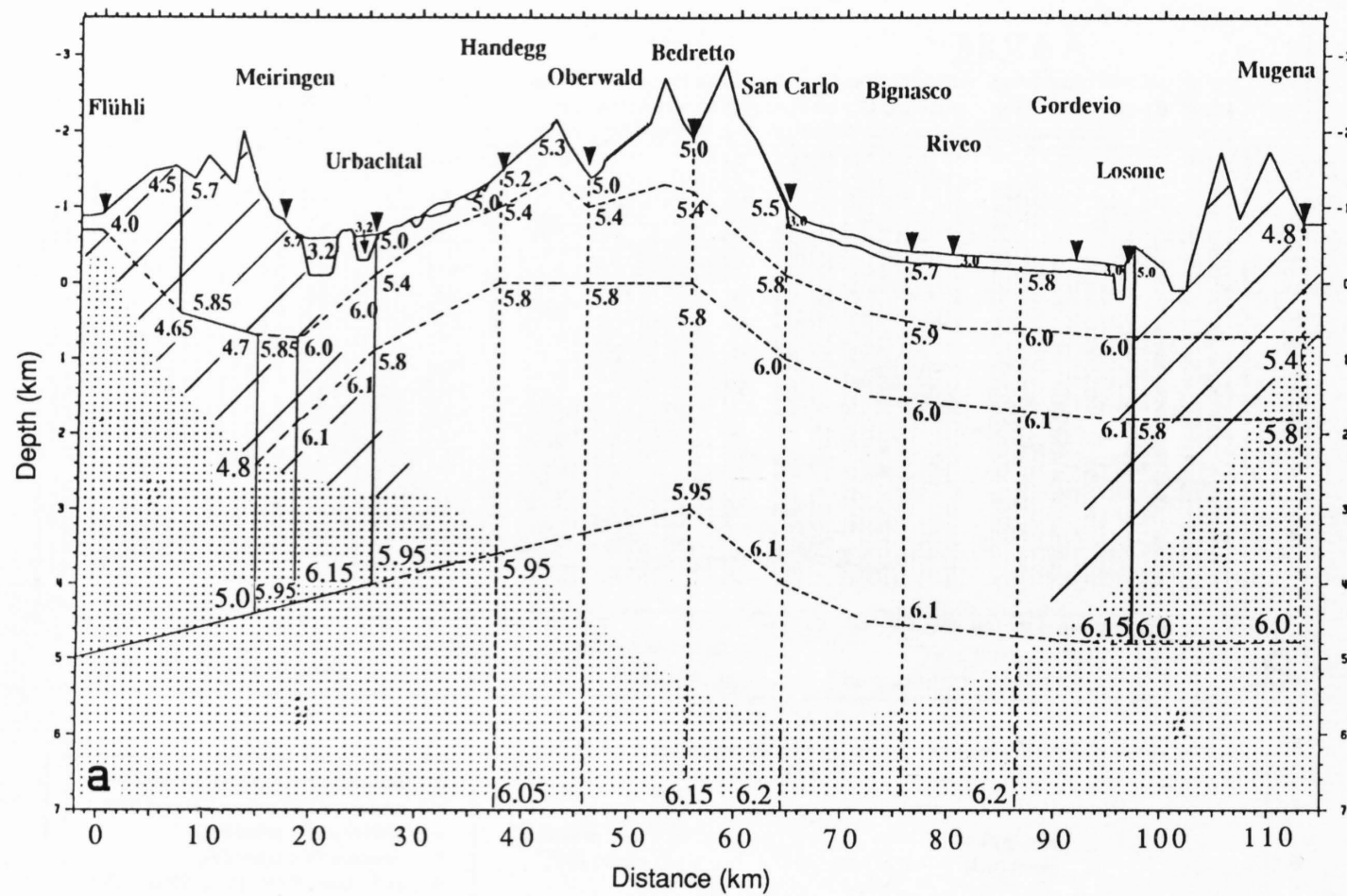
Figure 5.2-7
Velocity-depth structure along profile AAR 90 (see Figure 5.2-2) between Meiringen and Losone derived from first-break reflection and refraction data along reflection segments C1 and C2 (a). Velocities are unresolved in stippled area and very weakly controlled in hatched areas as indicated by the ray coverage (b) through the cross section from individual shotpoints (Kuhn, 1993). Depth scale is 7 times exaggerated; shotpoint localities are indicated by arrows.

– The strict separation into two regions – one with strong effect of the velocity field on the seismic signal and the other without any effect – is a simplification that may lead to unrealistic results.

– Fresnel volume calculations for 2-D seismic profiling assume ideal 2-D symmetry in the model structure. Thus, the lateral extension, i. e. perpendicular to the vertical plane beneath the profile, of the Fresnel volume depends on the 2-D structure and does not reflect any 3-D migration effect.

As a consequence, in our 3-D modeling concept for Alpine crustal structure we do not propose Fresnel volume calculations as a means to obtain 3-D uncertainty estimates. Rather, we use Fresnel calculations to define volumes of equal probability for the location of an imaged structural element. Within the vertical plane beneath the profile this area assumes the shape of the Fresnel volume (Figure 5.2-8a). In the direction perpendicular to this plane, however, the area of equal probability of the location of the reflector element takes on an arcuate shape (Figure 5.2-3) to account for out-of-plane migration effects (Figure 5.2-1).

The thus defined "3-D migration Fresnel volumes" apply to observations of seismic phases of highest-possible quality. To qualitatively account for lower quality observations we introduce an observation and interpretation weighting scheme (Kissling, 1993; Baumann, 1994; Waldhauser et al., 1994) that attributes a weighting factor to each structural element summarizing the quality with which it is known, relative to the highest possible quality for such a structure. As a first-order estimate the "3-D migration Fresnel volume" of a structural element of lower quality equals the volume of the highest possible quality multiplied by the inverse of the quality weighting factor.

In our 3-D seismic modeling concept we use the "3-D migration Fresnel volume" to control the 3-D migration process of corresponding structural elements illuminated by crossing profiles (Figure 5.2-1). By our definiton, the limits of resolution by 2-D seismic profiling are reached if the "3-D migration Fresnel volumes" overlap in parts large enough to fully accommodate the structural element imaged by the two profiles. Resolution of more details, such as, e. g., the exact length of the structural element within the "3-D migration Fresnel volume", requires usage of a seismic method capable to directly image 3-D structure, such as seismic tomography, and seismic sources in the vicinity of the structural element.
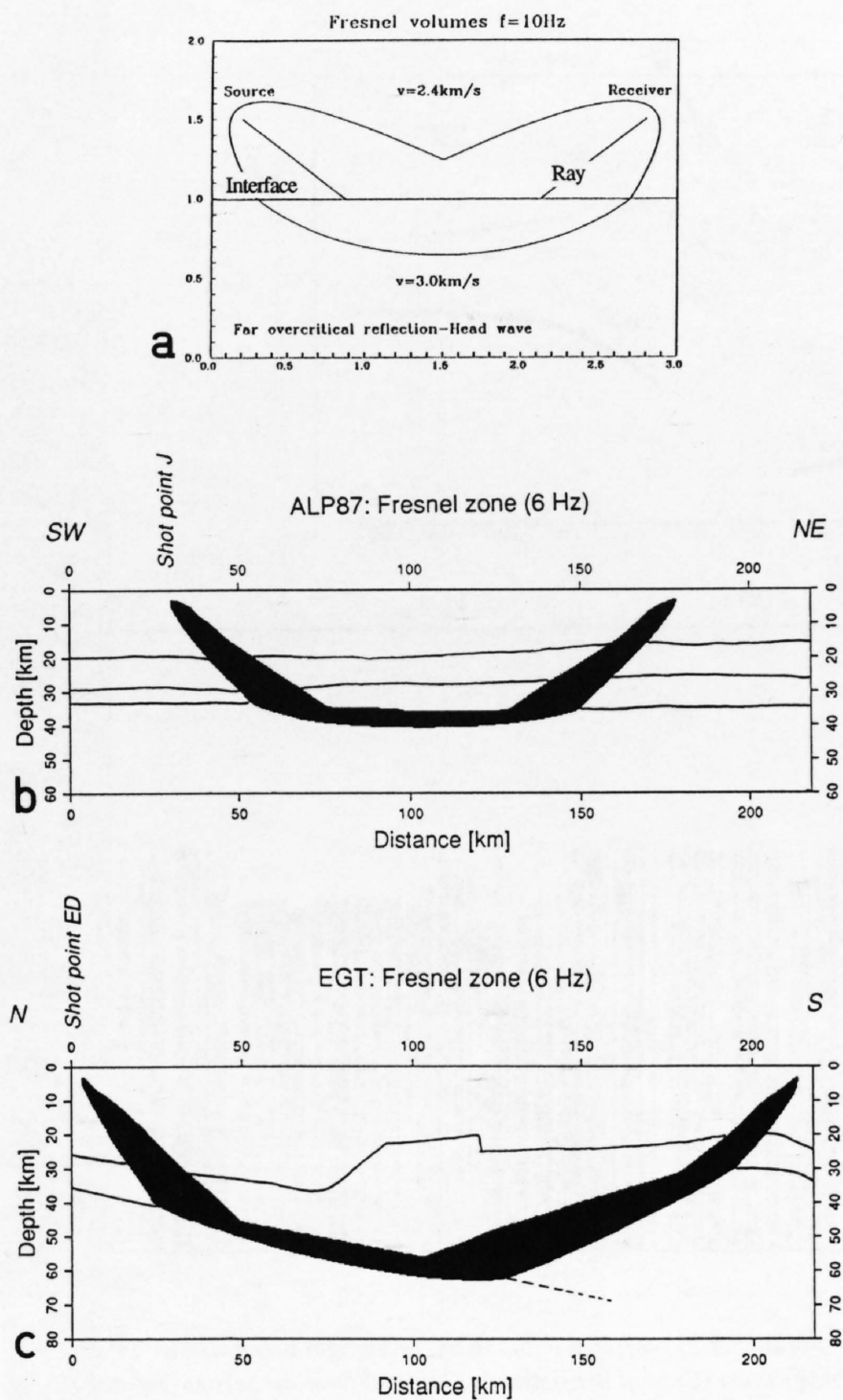
Figure 5.2-8

a: Fresnel volume for overcritically reflected and refracted waves with dominant frequency 10 Hz (after Klimes and Kvasnicka, 1994).

b: Fresnel volume display for 6 Hz first arrivals at 180 km offset through the lower crustal structure by Maurer and Ansorge (1992) of along-strike profile ALP 87.

c: Same as (b) for shot ED recorded southward through perpendicular to strike oriented EGT model by Ye (1992) (after Baumann, 1994).

5.2.5 Discussion and conclusion

Reflection and refraction seismic techniques measure two different physical rock parameters, the impedance contrast and the average layer velocity, respectively. This is of great advantage when both methods independently and reliably image the internal structure of the same subsurface volume. In this – obviously ideal – case, information in addition to geometry may be gained on fabric and possibly on geochemistry (e. g. Mueller, 1977) by combination of the two seismic methods. Within the Alpine region, however, it is possible to derive a unified acoustic (2-D) image of the crust only along the EGT (Holliger and Kissling, 1991). Based on seismic velocity, reflectivity pattern, and bulk density, Holliger and Kissling (1992) interpreted the indenter separating upper from lower European crust in the Central Alps (Valasek et al., 1991) as a "mélange" consisting mainly of lower crustal material.

Each (2-D) seismic technique has its specific strengths and weaknesses (Mooney and Brocher, 1987) when applied to deep 3-D crustal structure. Occasionally one seismic method may compensate local imaging problems encountered with the other method. For example, – again along the EGT – an intriguing gap in the reflectivity pattern from the central part of the near-vertical reflection seismic profile (Valasek, 1992) led to speculations about a possible gap in the Moho (Pfiffner et al., 1990) marking the central Alpine "Verschluckungszone" (Ampferer, 1906; Laubscher, 1990). Wide-angle reflections with NMO-correction along the EGT refraction profile (Valasek 1992) and along several longitudinal refraction profiles (Holliger and Kissling, 1991; Ye et al., 1995) on the other hand show a clear seismic Moho across this gap in the reflectivity pattern (Figure 5.2-9). The clearly identifyable seismic phases and the smooth trough-like shape of the Moho in this

region make it possible to reliably image this structure with only refraction seismic profiles. In general, however, refraction seismic profiles cannot replace reflection profiles – and vice versa –, without hampering the reliability of the assembled 3-D model. For a successful 3-D migration, a dense network of seismic profiles is a prerequisite. Therefore, to obtain highly reliable images of 3-D deep crustal structure by 2-D seismic profiling, networks of refraction and near-vertical reflection seismic profiles are necessary.

A refraction seismic profile network ideally consists of many longitudinal profiles parallel to the Bouguer gravity anomalies with a few transverse profiles placed above the bottoming points of the longitudinal lines. A deep seismic near-vertical reflection profile network designed to resolve the 3-D deep crustal structure beneath an orogen ideally consists of many transverse and a few longitudinal profiles. By combination of reflection and refraction seismic data, profile networks of these two types allow the constrained 3-D migration of structural information obtained along individual profiles to derive a highly reliable 3-D crustal model. In the Alps, one well-placed transverse refraction profile – the EGT – and many longitudinal refraction profiles exist. Several near-vertical reflection seismic profiles traverse fully or in large parts the Alpine orogen. Unfortunately, the only longitudinal reflection profile (in the eastern Swiss Alps) does not intersect with a transverse line. For this incomplete, although for an orogen worldwide unmatched data set, we designed our strategy to assemble a 3-D crustal model. Thus, projection of velocity information necessary for in-plane migration of near-vertical reflection data cannot be avoided. In many places seismic reflection and seismic refraction data rather than complementing each other must be used to replace one another. To avoid unjustified projection of structural elements, constrained 3-D migration is possible only for the crustal structure of the eastern Swiss Alps and for the crust-mantle boundary in large parts of the Central and Western Alps. For these structures a reliable 3-D model may be derived (Waldhauser et al., 1994). In all other areas, 3-D structural models depend more or less on assumptions that cannot be tested or justified by seismic data available today.

5.2.6 Summary

The large number of crossing seismic refraction and reflection profiles in the Alpine area brings us closer to assess a truely 3-D image of the crustal structure. By far most of these data were collected along profiles which implies for each one a 2-D interpretation. Under the given favourable circumstances in the Alps the validity of the 2-D interpretations can be controlled by means of crossing profiles and eventually extended to a 3-D structure. This requires a carefully controlled migration in space. In order to relate structural features from one profile to the other, seismic phases or waves have to be identified on individual profiles or sections as reflections or refractions from specific crustal elements. Fresnel volume calculations with dominant freqencies allow uncertainty estimates for specific structural elements. This value given for best-quality observations is modified by a weighting factor which includes data quality, orientation of profiles with respect to tectonic strike, and type of profile such as reversed or unreversed. The combination of properly oriented seismic refraction and near-vertical reflection profiles complement each other ideally with respect to geometry and imaging of reflectivity and seismic velocity. In the Alps ideal conditions for the development of a 3-D crustal model exist around the EGT and Eastern NRP 20 transect and for the Moho in the Central and Western Alps.

Figure 5.2-9

a: *Depth-migrated section of the eastern NRP 20 near-vertical reflection traverse (see Figure 5.2-2) projected onto the EGT (Holliger and Kissling, 1991). Solid line: Moho inferred mainly from seismic wide-angle data; wiggly line: top of the lower crust (Conrad discontinuity) inferred from the seismic refraction and reflection data (top of highly reflective lower crust).*

b: *Normal-incidence representation of wide-angle reflections from EGT refraction profiles (Valasek, 1992, Valasek et al., 1991). The gap in the reflection signal from the lower crust between 35 and 65 km profile distance in (a) is clearly covered by wide-angle reflection data, which is evidence for a smooth continuous European Moho beneath the Aar Massiv and the northern Penninic nappes. Note that all seismic data strongly indicate a vertical offset between the European and the Adriatic Moho beneath the Insubric line (see also Figure 5.2-4).*

6 Laboratory density and seismic properties of Alpine crustal rocks

J.-J. Wagner, R. Chessex, S. Sellami & F. Barblan

Contents

6.1 Introduction

Under the auspices of the NRP 20 "Study of the geological basement of Switzerland" several deep reflection seismic profiles were collected across the Swiss Alps. In order to determine petrological and geological models of the Alpine crust on the basis of such seismic or other geophysical methods, it is necessary to have a knowledge of the physical properties such as density and seismic velocity of the different lithologies. These properties vary with depth (pressure and temperature) and in the presence of fluids. This study discusses compressional wave velocities and densities which were acquired from samples from the major lithologies occurring within the seismic profiles, which were measured in the laboratory under dry conditions and at room temperature. The velocities were measured using confining pressures up to 400 MPa, which may correspond to a depth of approximately 12km. The aim of this laboratory research is to improve our understanding of crustal structure by taking advantage of the accessibility of a large variety of rocks exposed in the Alps.

The samples collected from the Swiss and N-Italian Alps are listed in Table 6-1. Although they are not representative of all the major tectonic units, they were selected to address problems associated with the NRP 20 Eastern and Western Traverses (see Pfiffner & Hitz, Chapter 9 and Steck et al., Chapter 12). Due to the dip of tectonic units in the Alps, rocks collected on outcrops can be projected down along the section plane of the seismic profiles. Some units have already been extensively sampled, for example the Ivrea Zone in the southern Alps (Fountain 1976, Burke and Fountain 1990, Barblan 1990). The other samples analyzed cover the Penninic and Helvetic zones of the Swiss Alps (Sellami et al. 1990, Sellami et al. 1993 and Sellami 1994).

To facilitate the presentation of the physical parameters, the rocks have been grouped here according to their origin as well as their mineralogical and chemical characteristics. The rocks have at least suffered the effects of low

grade metamorphism (laumontite-pumpellyite-prehnite facies) and most have been submitted to moderate to high-grade metamorphism.

The main rock types making up the different groups are:

Mafic group: gabbros, metagabbros, prasinites, amphibolites-amphiclasites, mafic granulites (granofels/pyriclasite/pyribolite).

Ultramafic group: peridotites, pyroxenites, hornblendites, serpentinites.

Metapelitic rocks: schists, kinzigitic gneisses, stronalites.

Carbonate rocks: limestones, dolomites, marbles, calcsilicates, calcschists.

Various: felsic granitoids and gneisses, felsic and intermediate volcanics (dacite, andesite, porphyry), metaclastics (sandstone, conglomerate).

There is reasonable agreement among Alpine geologists concerning the terminology of igneous and sedimentary rocks. This it is not so much the case with metamorphic rocks, including the mafic rocks of the Ivrea Zone which belong to the amphibolite-granulite facies. As far as possible, the recommendations of Schmid (1968), who has worked extensively in this key region, have been followed. For example in the case of the Ivrea metabasites of the Ossola Valley, Schmid (1968) uses the name of "granofels" for certain gabbros or amphibolites. In the case of metapelites, which were all sampled in the Ivrea Zone, the terms kinzigitic gneiss (amphibolite facies: biotite/garnet ratio greater than unity) and stronalite (granulite facies: biotite/garnet ratio lower than unity) are retained.

6.2 Experimental techniques

Sampling procedure

Whenever possible unweathered decimetric blocks were collected and any structural fabrics observed at the outcrop site were noted. The samples were always cored in the laboratory along three orthogonal directions X, Y and Z (Barblan 1990). The reference system for each sample is normally defined on the basis of macroscopic features such as sedimentary bedding, magmatic banding or a foliation (schistosity or cleavage) plane and lineation. The first core is always perpendicular to the major planar fabric (//Z), the second in the plane and perpendicular to the lineation if any (//Y), and the third core lies also in the plane but is parallel to the lineation (//X). The three specimens with a diameter of 2.5 cm. were cut to a length of 5 cm. The ends of each cylindrical section were polished to improve contact with the transmitter and receiver transducers used for the velocity measurement (see velocity measurements).

Density and porosity

The density of a rock is defined as the mass per unit volume, which in SI units is kg/m^3. It varies with the mineralogical composition and also with the porosity. We can distinguish the matrix density (also referred to as grain density) related to the mass and volume of the solid material (Olhoeft and Johnson 1989) from the apparent matrix density which takes into consideration the apparent matrix volume and which includes both grains and "isolated" pores. The dry bulk density accounts in the absence of fluids for the total volume of solid material and the voids (both isolated and connected).

The total porosity represents the total volume of all void spaces in the material, whether connected or isolated, and the effective porosity, used here, corresponds only to the volume of the interconnected pores.

Methods for determining density and porosity

All specimens were dried for 24 hours in a furnace at a constant temperature of 90 °C. Masses were measured with a Mettler model PM100 high-precision digital balance which has an accuracy of 10^{-5} kg. This balance is equiped to measure bulk volume using Archimedes' principle. To determine the dry bulk density, the specimen is weighed first in air and then a second time suspended in a liquid of known density, in this case water. As we deal with low porosity rocks, one can assume that the liquid does not penetrate the specimen provided one makes a rapid measurement. The reproducibility of the volume estimate is better than $10^{-7} m^3$.

By using gas volumetry, it is possible to calculate the matrix volume or the apparent matrix volume depending on whether or not the voids, pores and/or
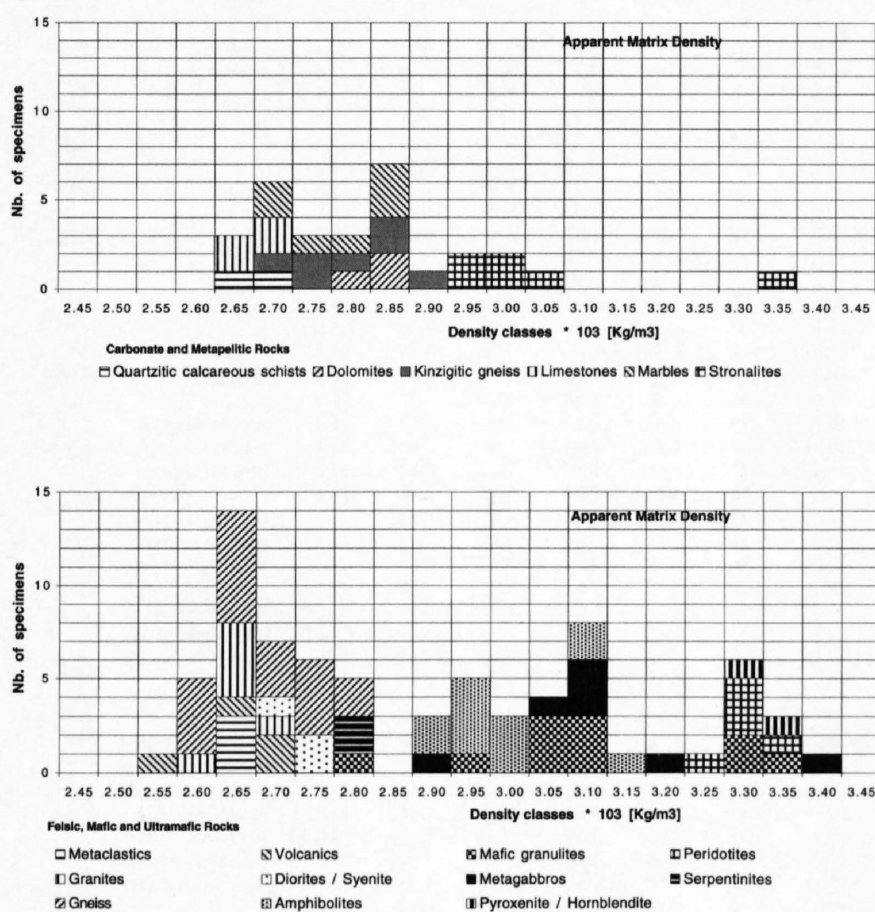

Figure 6-1
Histograms of apparent matrix densities of carbonates and metapelitic rocks (upper diagram) and felsic, mafic and ultramafic rocks (lower diagram).

Specimen No.	Rock Type (Geological unit)	Dry bulk density 10^3 [kg/m³]	V1//Z 20 MPa [km/s]	V2//Y 20 MPa [km/s]	V3//X 20 MPa [km/s]	VM 20 MPa [km/s]	Seismic impedance 20 MPa 10^6 [kg/m²s]	Apparent matrix density 10^3 [kg/m³]	V1//Z 400 MPa [km/s]	V2//Y 400 MPa [km/s]	V3//X 400 MPa [km/s]	VM 400 MPa [km/s]	Seismic impedance 400 MPa 10^6 [kg/m²s]	Sample locality
	Metapelites													
ST10	Black shale (Widhorn Nappe, Liassic)	2.76	3.20	–	5.36	4.28	11.8	2.76	5.72	–	6.53	6.13	16.9	
IV34	Kinzigitic gneiss	2.74	4.39	5.57	5.60	5.19	14.2	2.75	5.72	6.39	6.51	6.21	17.1	Porte Ochera
IV39	Kinzigitic gneiss	2.80	4.48	4.53	5.87	4.96	13.9	2.81	6.24	6.33	6.95	6.51	18.3	Grampi
IV48	Kinzigitic gneiss	2.78	4.70	5.00	6.19	5.30	14.7	2.79	5.84	6.17	6.91	6.31	17.6	Madonna del Boden
IV53	Kinzigitic gneiss	2.66	4.61	4.95	5.02	4.86	12.9	2.71	6.06	6.09	6.11	6.09	16.5	Grampi (river)
IV54	Kinzigitic gneiss	2.79	4.49	4.57	4.84	4.63	12.9	2.86	6.04	6.09	6.34	6.16	17.6	Grampe (rIver)
IV27A	Kinzigitic gneiss, mylonitic, retromorphosed	2.84	4.43	5.43	5.51	5.12	14.6	2.94	5.84	6.17	6.39	6.13	18.0	Loro (below church)
IV28	Kinzigitic gneiss, mylonitic, retromorphosed	2.75	3.58	4.81	5.89	4.76	13.1	2.85	5.47	6.11	6.56	6.05	17.2	Loro
IV43	Stronalite	2.97	5.54	5.61	5.70	5.62	16.7	3.01	6.35	6.40	6.56	6.44	19.4	Piano di Forno
IV44	Stronalite	3.33	5.59	6.30	7.38	6.42	21.4	3.35	7.13	7.30	8.40	7.61	25.5	Piano di Forno
IV52	Stronalite	3.04	5.62	5.80	6.62	6.01	18.3	3.05	6.63	6.83	7.34	6.93	21.1	Piano di Forno
IV32	Mylonitic stronalite	3.03	5.87	6.31	6.40	6.19	18.8	3.03	6.38	6.78	6.92	6.69	20.3	Anzola (quarry)
IV33	Mylonitic stronalite	2.91	5.59	6.06	6.16	5.94	17.3	2.96	6.34	6.85	6.86	6.68	19.8	Anzola (quarry)
IV46	Mylonitic stronalite	2.97	5.48	5.64	6.60	5.91	17.5	2.97	6.37	6.53	7.35	6.75	20.0	Forno (S of village)
	Carbonates													
ST9	Limestone	2.70	4.00	4.68	5.00	4.56	12.3	2.70	5.97	6.35	6.37	6.23	16.8	
PF5	Limestone (Tschep Nappe, Malm)	2.73	6.15	6.48	–	6.32	17.2	2.74	6.51	6.69	–	6.60	18.1	Felsberg (GR)
PF6	Limestone (Axen Nappe, Malm)	2.67	6.23	6.29	–	6.26	16.7	2.67	6.41	6.42	–	6.42	17.1	Mäls (FL)
CAL1	Limestone, (Barremian)	2.69	6.41	6.49	6.51	6.47	17.4	2.69	–	–	–	–	–	
ST12	Dolomite (Röti dolomite, Triassic)	2.81	5.91	6.26	6.90	6.36	17.9	2.84	6.62	6.86	7.18	6.88	19.6	
PF15	Dolomite (Tschepp Nappe, Triassic)	2.83	5.68	6.27	–	5.98	16.9	2.86	6.90	7.16	–	7.03	20.1	Reichenau/Tamins (GR)
ST20	Dolomitic marble, (Gornergrat Zone)	2.84	5.27	5.45	5.69	5.47	15.5	2.87	6.95	7.24	7.45	7.21	20.7	
ST21	Dolomitic marble, (Gornergrat Zone)	2.81	4.68	5.66	5.77	5.37	15.1	2.86	6.68	7.06	7.29	7.01	20.0	
ST22	Dolomitic marble, (Gornergrat Zone)	2.85	4.32	4.85	5.30	4.82	13.7	2.87	7.05	7.06	7.33	7.15	20.5	
PF13	Marble (Aul Nappe)	2.70	6.24	6.62	6.62	6.49	17.5	2.70	6.75	7.01	7.20	6.99	18.9	Vals (GR)
PF4	Marble (Splügen Zone)	2.69	5.11	6.09	6.14	5.78	15.5	2.70	5.94	6.43	6.50	6.29	17.0	Splügen Pass
PF8	Dolomitic marble, (Misox Zone)	2.83	5.91	6.15	6.51	6.19	17.5	2.86	6.76	7.01	7.27	7.01	20.1	San Bernardino
IV38	Calcsilicate rock	3.22	5.74	6.08	6.39	6.07	19.5	3.22	6.95	7.31	7.33	7.20	23.2	Road to Forno (pt. 113)
ST3	Sandy calcschist, (Lebendun Nappe)	2.69	4.17	5.38	5.59	5.05	13.6	2.71	5.60	6.07	6.22	5.96	16.2	
ST2	Sandy calcschist, (Lebendun Nappe)	2.65	4.85	5.07	5.32	5.08	13.5	2.67	5.80	5.90	5.97	5.89	15.7	
	Felsic rocks													
D5	Granite	2.65	4.69	4.86	5.26	4.94	13.1	2.65	6.24	6.40	6.40	6.35	16.8	Miéville (quarry)
PF12	Granite (Central Aar granite, Aar Massif)	2.62	4.79	4.82	4.84	4.82	12.6	2.62	6.35	6.79	–	6.57	17.2	Schöllenen (UR)
IV11	Leucogranite	2.63	5.07	5.15	5.26	5.16	13.6	2.65	6.47	6.51	6.68	6.55	17.4	Mte Orfano (quarry)
D4	Mylonitic granite	2.63	4.12	4.62	4.80	4.51	11.9	2.69	6.01	6.37	6.39	6.26	16.8	Miéville (quarry)
IV12	Aplite	2.70	5.27	5.94	–	5.61	15.1	2.70	6.24	6.39	–	6.32	17.1	Civiasco
IV13	Aplite, slightly foliated	2.67	4.76	4.93	5.01	4.90	13.1	2.67	6.29	6.32	6.34	6.32	16.9	Civiasco
SL1	Andesite	2.72	5.55	5.58	5.73	5.62	15.3	2.73	5.89	5.93	5.99	5.94	16.2	Bachetto Sessera
PF10	Porphyry (Rofna Porphyry, Suretta Nappe)	2.68	3.80	3.94	4.73	4.16	11.1	2.70	5.93	6.07	6.23	6.08	16.4	Ausserferrera (GR)
PF16	Mylonitic porphyry (Rofna Porphyry, base Suretta Nappe)	2.65	–	4.50	4.93	4.72	12.5	2.66	5.65	6.12	6.27	6.01	16.0	Splügenpass (GR/I)
SL3	Diorite	2.76	4.78	4.91	5.04	4.91	13.6	2.77	6.21	6.24	6.36	6.27	17.4	Bico (quarry)
SL4	Diorite	2.74	4.86	5.03	5.30	5.06	13.9	2.76	6.17	6.19	6.29	6.22	17.2	Traversella
D8	Sandstone (fine grained)	2.65	5.34	5.41	5.42	5.39	14.3	2.65	6.03	6.04	6.09	6.05	16.0	Dorénaz
D7	Sandstone (coarse grained)	2.67	5.32	5.44	5.54	5.43	14.5	2.67	5.96	6.06	6.12	6.05	16.1	Dorénaz
D6	Conglomerate (Lower Stephanian)	2.66	5.09	5.38	5.49	5.32	14.2	2.66	5.98	6.04	6.09	6.04	16.1	Dorénaz
ST23	Paragneiss (Upper Stalden Zone)	2.74	4.04	5.03	5.12	4.73	13.0	2.75	5.68	6.10	6.29	6.02	16.6	
IV35	Paragneiss (with biotite + plagioclase)	2.78	5.34	5.78	5.92	5.68	15.8	2.79	5.95	6.35	6.39	6.23	17.4	Strona (river)
SC1	Gneiss	2.67	–	–	–	–	–	2.71	5.84	6.26	6.28	6.13	16.6	Mergozzo
ST4	Gneiss (Lebendun Nappe, Meta–arkose)	2.63	3.84	4.07	4.84	4.25	11.2	2.64	5.69	6.14	6.19	6.01	15.9	
ST8	Gneiss (Monte Leone Nappe, Meta–arkose)	2.64	4.57	4.87	5.09	4.84	12.8	2.64	5.83	6.15	6.28	6.09	16.1	
D1	Gneiss, chloritic	2.66	4.99	5.34	5.55	5.29	14.1	2.66	5.93	6.13	6.17	6.08	16.2	Evionnaz
D1A	Gneiss, chloritic	2.67	5.12	5.52	5.60	5.41	14.5	2.68	6.03	6.20	6.23	6.15	16.5	Evionnaz
PF2	Gneiss (Adula Nappe)	2.64	3.95	4.74	5.08	4.59	12.1	2.64	5.83	6.14	6.17	6.05	16.0	Passo del San Bernardino (GR)
PF9	Paragneiss (Suretta Nappe)	2.78	3.74	5.50	5.53	4.92	13.7	2.78	5.65	6.38	6.54	6.19	17.2	Val Madris (GR)
PF17	Mylonitic gneiss (Gadriol unit/Misox Zone)	2.67	4.44	5.24	5.39	5.02	13.4	2.67	5.92	6.37	–	6.15	16.4	Mesocco (GR)
D2	Biotite-Gneiss	2.68	4.87	4.89	5.42	5.06	13.6	2.68	5.94	6.09	6.17	6.07	16.3	La Balmaz
D3	Biotite-Gneiss	2.75	4.76	5.06	5.37	5.06	13.9	2.75	5.85	6.00	6.08	5.98	16.4	La Balmaz
ST11	Augengneiss	2.67	3.80	4.12	5.35	4.42	11.8	2.68	6.00	6.07	6.30	6.12	16.4	
PF3	Mylonitic Augengneiss (Tambo Nappe)	2.82	3.77	4.90	5.51	4.73	13.3	2.82	5.68	6.04	6.32	6.01	17.0	Val Vignone (GR)
PF7	Augengneiss (Tambo Nappe)	2.71	4.19	4.76	5.10	4.68	12.7	2.72	5.94	5.96	6.17	6.02	16.4	Val Vignone (GR)
SS1	Schistose gneiss	2.66	4.05	–	4.66	4.36	11.6	2.68	5.76	6.04	–	5.90	15.8	Niederalp (Simplon)
ST1	Granodioritic Gneiss (Antigorio Nappe)	2.61	4.33	5.12	5.16	4.87	12.7	2.63	6.11	6.16	6.33	6.20	16.3	
IV25	Granulite	2.79	5.86	5.89	5.95	5.90	16.5	2.80	6.61	6.70	6.78	6.70	18.8	Monte Rubello
SS2	Blasto–mylonitic gneiss	2.68	5.05	4.56	4.98	5.05	13.5	2.71	5.97	6.15	6.29	6.14	16.6	Simplon Village
	Mafic rocks													
IV23	Gabbro	3.24	6.21	6.47	6.54	6.41	20.8	3.24	7.63	7.70	7.74	7.69	24.9	Balmuccia (Guaifola)
IV22	Leuco-gabbro	2.90	5.91	6.06	6.21	6.06	17.6	2.94	6.92	6.92	6.95	6.93	20.4	Balmuccia (Guaifola)
IV21	Fractured gabbro, retromorphosed	3.09	5.65	5.77	5.79	5.74	17.7	3.10	6.91	7.18	7.22	7.10	22.0	Balmuccia (river)
IV1	Gabbro, retromorphosed	3.05	6.06	6.07	6.11	6.08	18.5	3.06	6.81	6.89	6.95	6.88	21.1	Loro (church)
IV2	Gabbro, retromorphosed	3.11	5.66	5.98	6.59	6.08	18.9	3.12	6.93	7.22	7.70	7.28	22.7	Loro (church)
ST18	Metagabbro (Zermatt–Saas Zone)	3.10	5.27	5.27	5.41	5.32	16.5	3.07	7.18	7.35	7.35	7.29	22.4	
ST19	Eclogitic metagabbro (Zermatt–Saas Fee Zone)	3.43	7.10	7.13	7.18	7.14	24.5	3.43	7.92	7.94	8.06	7.97	27.3	
ST5	Biotite–Amphibolite (Lebendun Nappe)	2.98	4.19	5.21	5.51	4.97	14.8	2.98	5.90	6.71	6.80	6.47	19.3	
ST14	Garnet–amphibolite (Zermatt–Saas Fee Zone)	2.96	5.03	5.70	6.06	5.60	16.6	2.97	6.43	6.93	6.99	6.78	20.1	
ST7	Amphibolite (Berisal Unit)	2.97	4.78	5.28	6.10	5.39	16.0	2.98	6.08	6.32	6.93	6.44	19.2	
ST13	Amphibolite (Portjengrat Zone)	2.96	3.90	4.66	5.12	4.56	13.5	2.97	6.29	6.78	7.03	6.70	19.9	
IV36	Amphibolite	2.99	5.45	6.24	6.51	6.07	18.1	3.02	6.33	6.87	7.02	6.74	20.4	Strona
IV37	Amphibolite	3.14	4.63	5.44	5.93	5.33	16.7	3.17	6.85	7.09	7.35	7.10	22.5	Road to Forno (pt. 113)
IV29	Mylonitic amphibolite, retromorphosed	2.94	5.93	6.30	6.83	6.35	18.7	2.94	6.57	6.91	7.08	6.85	20.1	Loro
IV41	Mylonitic amphibolite	3.06	5.69	–	6.59	6.14	18.8	3.14	6.56	–	7.14	6.85	21.5	Rosarolo (river)
IV55	Mylonitic amphibolite	3.07	5.83	5.96	6.15	5.98	18.4	3.11	6.55	7.04	7.19	6.93	21.5	Grampi
ST17	Amphibolite, retromorphosed (Zermatt–Saas Fee Zone)	2.94	4.08	4.20	4.98	4.42	13.0	2.94	6.61	6.70	7.03	6.78	19.9	
IV50	Amphibolite	3.04	6.32	6.41	6.70	6.48	19.7	3.10	6.69	6.89	7.06	6.88	21.3	Anzola (quarry)
IV51	Amphibolite	3.01	6.44	6.49	6.55	6.49	19.5	3.05	6.97	6.99	7.04	7.00	21.4	Anzola (quarry)
IV49	Amphibolite	3.07	5.95	6.43	6.85	6.39	19.6	3.12	6.44	6.88	7.16	6.83	21.3	Anzola (quarry)
IV19	Mafic mylonite, retromorphosed	2.95	5.11	5.81	6.01	5.64	16.6	2.96	6.72	6.92	6.88	6.84	20.2	Chioso (near bridge)
IV20	Meta–basalt, highly deformeded, retromorphosed	2.84	6.06	6.16	6.35	6.19	17.6	2.84	6.58	6.62	6.65	6.62	18.8	Balmuccia (river)
IV7	Mafic granulite	3.34	6.64	6.85	6.88	6.79	22.7	3.34	7.22	7.34	7.45	7.34	24.5	Riale Arca (river)
IV3	Mafic granulite	3.05	6.43	6.64	6.76	6.61	20.2	3.06	7.13	7.26	7.42	7.27	22.2	Riale Arca (river)
IV5	Mafic granulite	3.07	6.21	–	6.77	6.49	19.9	3.08	7.47	–	7.70	7.59	23.4	Riale Arca (river)
IV45	Garnet–granulite	3.12	5.35	5.62	6.20	5.72	17.9	3.14	6.85	6.86	7.00	6.90	21.7	Piena di Forna
IV6	Garnet–granulite	3.36	5.68	6.36	5.37	5.80	19.5	3.37	7.42	7.51	7.53	7.49	25.2	Riale Arca (river)
IV8	Granulite	3.30	6.59	6.86	6.73	6.73	22.2	3.30	7.13	7.28	7.41	7.27	24.0	Riale Arca (river)
PF14	Metabasalt (Aul Nappe)	2.89	4.41	4.89	6.25	6.73	19.4	2.96	6.45	6.72	7.27	6.81	20.2	Vals (GR)
	Ultramafic rocks													
IV17	Peridotite	3.31	7.68	7.78	7.85	7.77	25.7	3.31	7.88	8.05	8.16	8.03	26.6	Balmuccia (quarry)
IV18	Peridotite	3.35	7.91	7.50	8.17	7.86	26.3	3.35	7.85	8.28	8.47	8.20	27.5	Balmuccia (quarry)
IV26	Peridotite	3.31	7.72	7.85	8.12	7.90	26.1	3.31	8.17	8.33	8.62	8.37	27.7	Baldissero (quarry)
IV31	Peridotite	3.29	7.70	7.88	8.16	7.91	26.0	3.29	7.90	8.80	8.32	8.34	27.4	Rio Inferno (river)
IV30	Peridotite	3.31	7.37	7.84	7.90	7.70	25.5	3.31	8.01	8.15	8.29	8.15	27.0	Rio Inferno (river)
IV24	Pyroxenite	3.32	7.16	7.40	–	7.28	24.2	3.36	7.58	7.80	–	7.69	25.8	Balmuccia (Guaifola)
IV4	Hornblendite	3.32	6.60	6.80	7.50	6.97	23.1	3.32	7.52	7.65	8.03	7.73	25.7	Riale Arca (river)
ST15	Serpentinite (Zermatt–Saas Fee Zone)	2.82	5.80	–	7.41	6.60	18.6	2.82	6.23	–	7.61	6.92	19.5	
ST16	Serpentinite (Zermatt–Saas Fee Zone)	2.81	6.17	–	6.54	6.36	17.9	2.82	6.37	–	6.72	6.54	18.5	

Table 6.1

fissures are all interconnected (Johnson 1979). The instrument employed was a Quantchrome Helium gas stereopycnometer; which allows a volume determination with an accuracy of 10^{-7} m^3.

The porosity or effective porosity is computed on the basis of the Archimedes and the pycnometric volumes.

Velocity measurements

The effect of confining pressure on P-wave velocities has been investigated by stepwise increases up to a maximum of 400 MPa. The rock sample is placed within a pressure vessel using a two step system comprising an air compressor and a high pressure hydraulic pump. A classical transit pulse technique (Birch 1960, Barblan 1990) is used. Lead-zirconate (PZT) transducers with 1-MHz resonant frequency serve for transmitting and receiving the compressional wave pulses, which are produced by a Velonex model 345 or Hewlett-Packard model 214 B generator. One transducer is mounted on each face of the cylindrical specimen, which is jacketed with retractable plastic tube to prevent hydraulic oil contamination. The transit time of the elastic wave is measured with a Gould 4072 digital dual-trace oscilloscope and then stored directly on a computer. All specimens are measured under dry conditions and at room temperature.

6.3 Density data

Apparent matrix densities

The apparent matrix densities of the rocks are directly related to their mineralogical composition (density of the rockforming minerals) and "isolated" voids of the specimens. The density data (mean of three specimens) are given in Table 6-1. The histograms of Figure 6-1 show statistical details of the apparent matrix densities for the previously defined rock types. The values range from 2.57×10^3 to 3.43×10^3 kg/m^3. The values for the carbonates range from 2.65×10^3 to 2.87×10^3 kg/m^3. The density of the carbonates (especially marbles) is very dependent on whether they contain calcite (2.71×10^3 kg/m^3) or dolomite (2.83×10^3 kg/m^3). The metapelitic rocks vary from 2.70×10^3 to 3.05×10^3 kg/m^3 with one exceptional value at 3.35×10^3 kg/m^3. In this group we can distinguish the gneisses, the densities of which are very dependent on the quartz-feldspar content (Sellami 1994). It is interesting to note that the major density difference between the metapelites occurs between the amphibolite-facies and the granulite-facies rocks (Fountain, 1996). Figure 6-1 (lower diagram) shows an apparently trimodal distribution for felsic, mafic and ultramafic rocks, with each of the rock groups dominating one peak. Felsics rocks vary between 2.55×10^3 and 2.80×10^3 kg/m^3, mafics between 2.90×10^3 and 3.20×10^3 kg/m^3 and ultra-
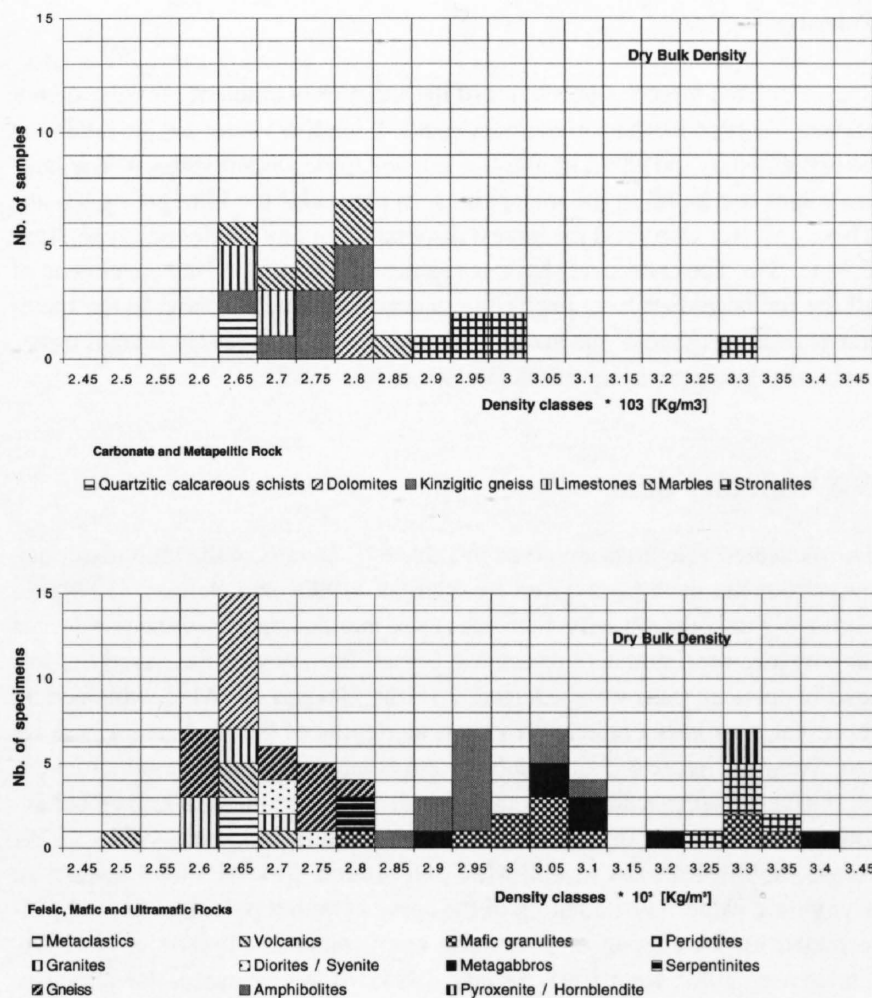
Figure 6-2
Histograms of dry bulk densities of carbonates and metapelitic rocks (upper diagram) and felsic, mafic and ultramafic rocks (lower diagram).

mafics between 3.25×10^3 and 3.35×10^3 kg/m^3. The main exception to this correlation is the ultramafic serpentinites, where the serpentinization process results in a decrease of the density (Christensen 1972, Kern and Tubia 1993, Sellami 1994).

Dry bulk densities

Statistics for the dry bulk densities are given in Figure 6-2. They are lower than the matrix densities, but because of the low porosity of the rocks included in this study, they are only slightly lower. Their broad ranges and distributions are similar to those described in the previous paragraph.
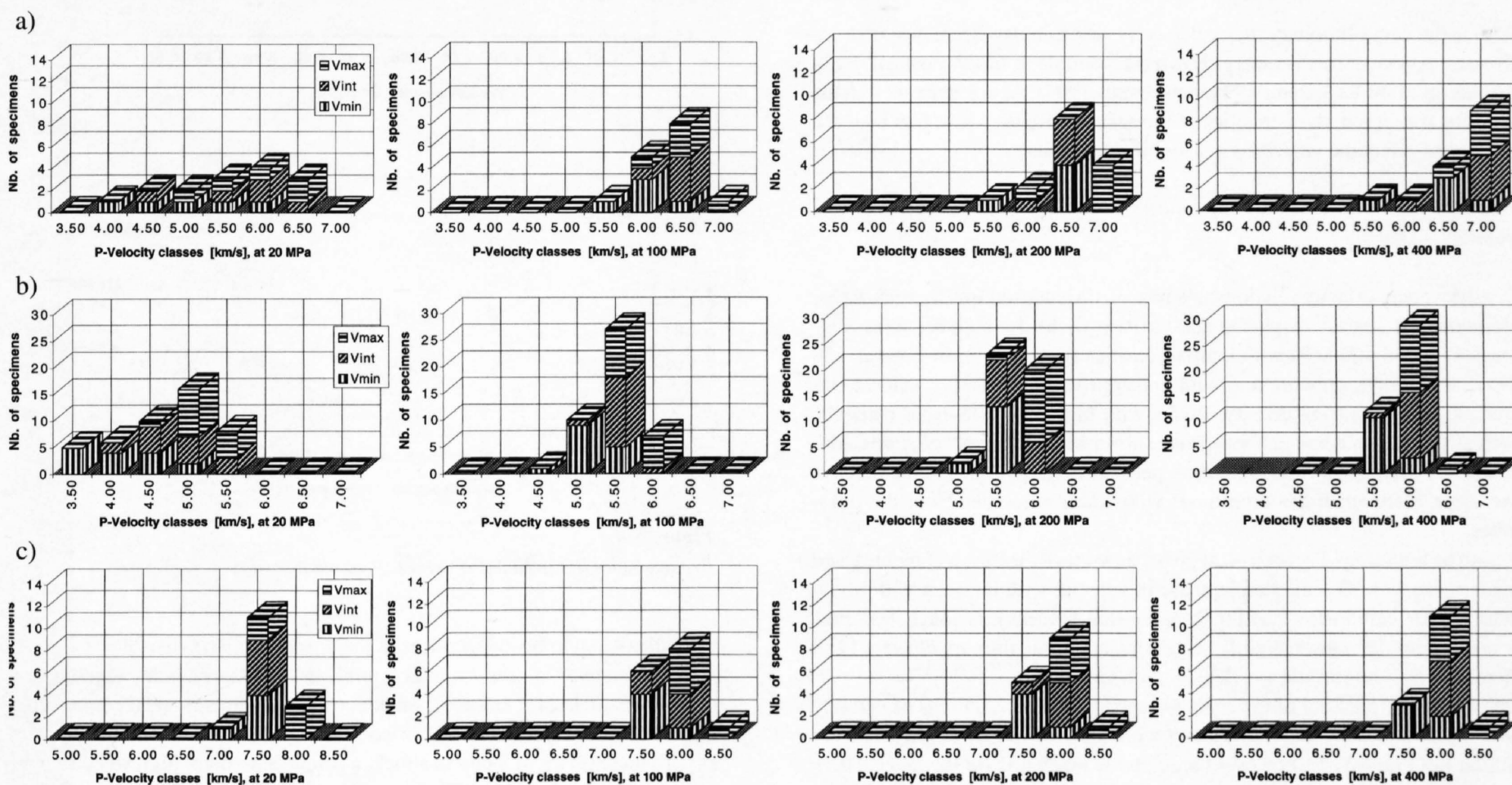
Figure 6-3
Histograms of the minimum, intermediate and maximum P-wave velocities for four pressure steps (20, 100, 200 and 400 MPa) with statistical parameters.
a) marbles, b) gneisses, c) peridotites.

Porosity

The calculated effective porosities of the samples at ambient pressure do not exceed 4% even for the sedimentary rocks. Such low values for the latter can be explained by the effect of the low grade Alpine metamorphism. The largest values are found in the metapelites, in particular the kinzigitic gneisses. These gneisses also yield the largest dispersion for any single rock type, from 0.3 to 3.5%. The carbonates have porosities up to 2.0%. Many specimens of all the rocks studied have negligible or zero effective porosity. In the metamorphosed or igneous specimens, some of the voids may, in certain cases, represent decompression cracks (Vernik & Nur 1992).

6.4 Velocity data

The measured velocities are given in Table 6-1. Details of the individual rock measurements have been given by Barblan (1990) and Sellami (1994). In Figure 6-3 only the velocity distributions of marbles, gneisses and peridotites are given as represantative examples. For all the samples measured the following pressure steps were selected: 20, 100, 200 and 400 MPa, which could represent, to a very crude approximation, depths of 0.6, 3, 6 and 12 km respectively. In Figure 6-3 maximum, intermediate and minimum velocities are plotted at the same scales. All rock types demonstrate the well known behaviour in which, under dry conditions and at room temperature, velocities increase rapidly from 20 to 100 MPa and around 300 MPa tend toward an asymptotic value. The flattening of the curve at higher pressures has to be interpreted as the closing of pores and microfractures (Toksöz et al. 1976, Christensen 1989, Kern 1991, Sellami 1994). At low pressures the velocities are strongly influenced by the voids, pores and/or fractures, but at high pressure the values are representative of the mineral composition and assemblage.

In general for each rock type the velocity range is larger at 20 MPa (larger standard deviation) than at higher pressures; the main exception to this observation is the peridotites (shown in Figure 6-3 c)). This can also be seen in some pyroxenite and peridotites measured by Burke & Fountain (1990). It could mean that the anisotropy of the minerals is more important than the anisotropy of the closure of pores and microcracks with increasing pressure (Sellami, 1994).

The velocity decreases with temperature (Christensen 1989, Kern 1982). This behaviour depends on rock type but is linear and amounts to less than a few percent for temperatures up to 400°C for most of the rock types except sandstones and dolomites (Sellami 1994).

6.5 Discussion

Velocity – Porosity

Within the same lithology, the velocity of dry samples decreases with increasing porosity. This is cleary shown for example in limestones whith porosities up to 40% (Sellami 1994, Anselmetti 1994). As we have seen in the previous paragraph, the porosities of the samples are very low, less than 4% and do not affect the velocities in a significant manner.

Velocity – Density

Density versus velocity relationships have been analyzed for dry rock measurements and they are displayed at 20 MPa with the dry bulk densities (Figure 6-4) and at 400 MPa with matrix densities (Figure 6-5). In general, and especially at high pressure and with apparent matrix densities, velocity increases with increasing density. Rocks with high quartz-feldspar contents, such as granites or some gneisses, have shown a low range of velocities. Mafic and ultramafic rocks (metagabbros, peridotites) have higher velocities. We can again distinguish the limestones with lower velocities from the dolomites.

As can be seen from Figure 6-4, at 20 MPa two rock classes, metapelites and mafic rocks, exhibit a marked increase in velocity with increase of dry bulk density. For carbonates and felsic rocks this tendency is much less pronounced, and the non-or slightly serpentinized ultramafics are clustered and there is almost no variation of density with velocity.

Due to the low porosity of the analyzed specimens the variations of velocity with dry bulk density and the velocity with apparent matrix density data are similar (cf Figure 6-5), however the scatter is much less for the latter. There is a much better correlation between bulk density and velocity for the metapelites and the mafic rocks, and linear relation can be determined in the case of the carbonates.

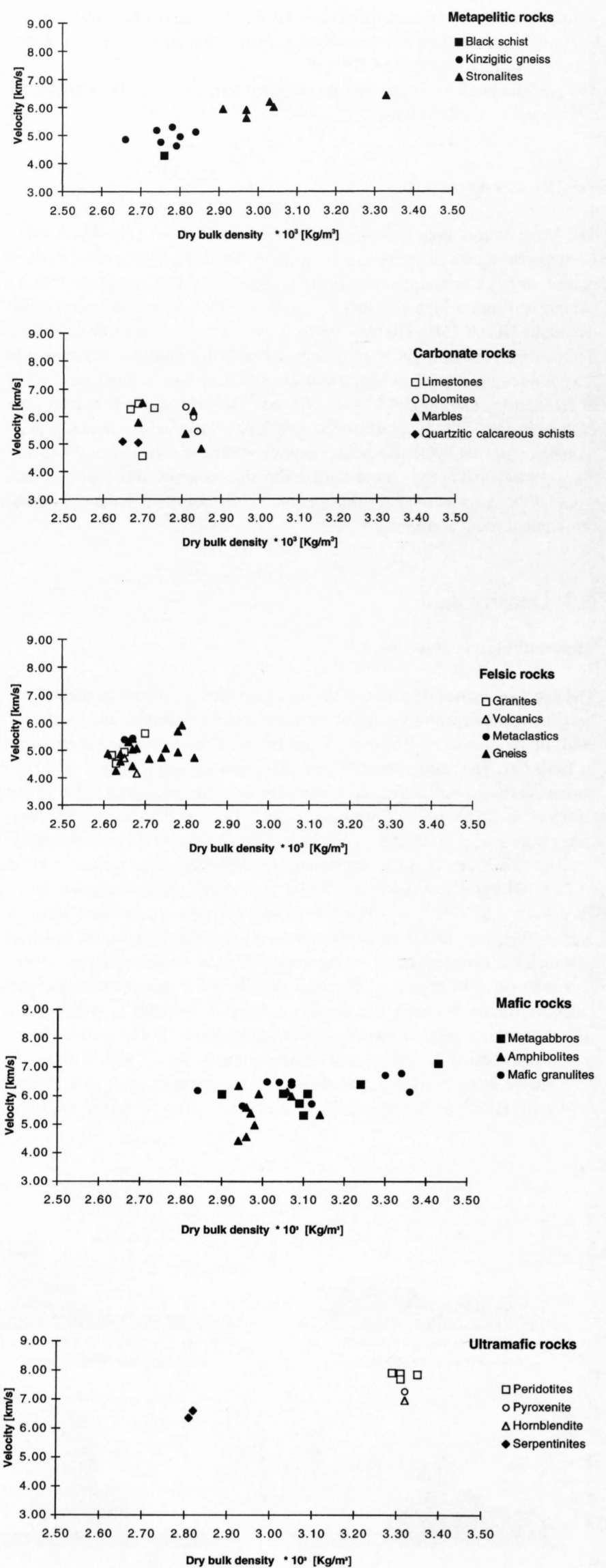In the case of the felsic rocks (with a high felspar content) in Figure 6-5, the

Figure 6-4
P-wave velocity at 20 MPa versus dry bulk density.

velocities seem to be independent of the apparent matrix densities. Comparing the content of high velocity minerals like amphibole, epidote and opaques in gneiss, for example, we notice that the mineralogical composition does not affect the velocity in the same straightforward manner as the density. To increase the velocity in a rock, a certain amount of high velocity minerals in the rock is needed. The assemblage and distribution the minerals in the rock also have a big influence on this increase (Sellami 1994).
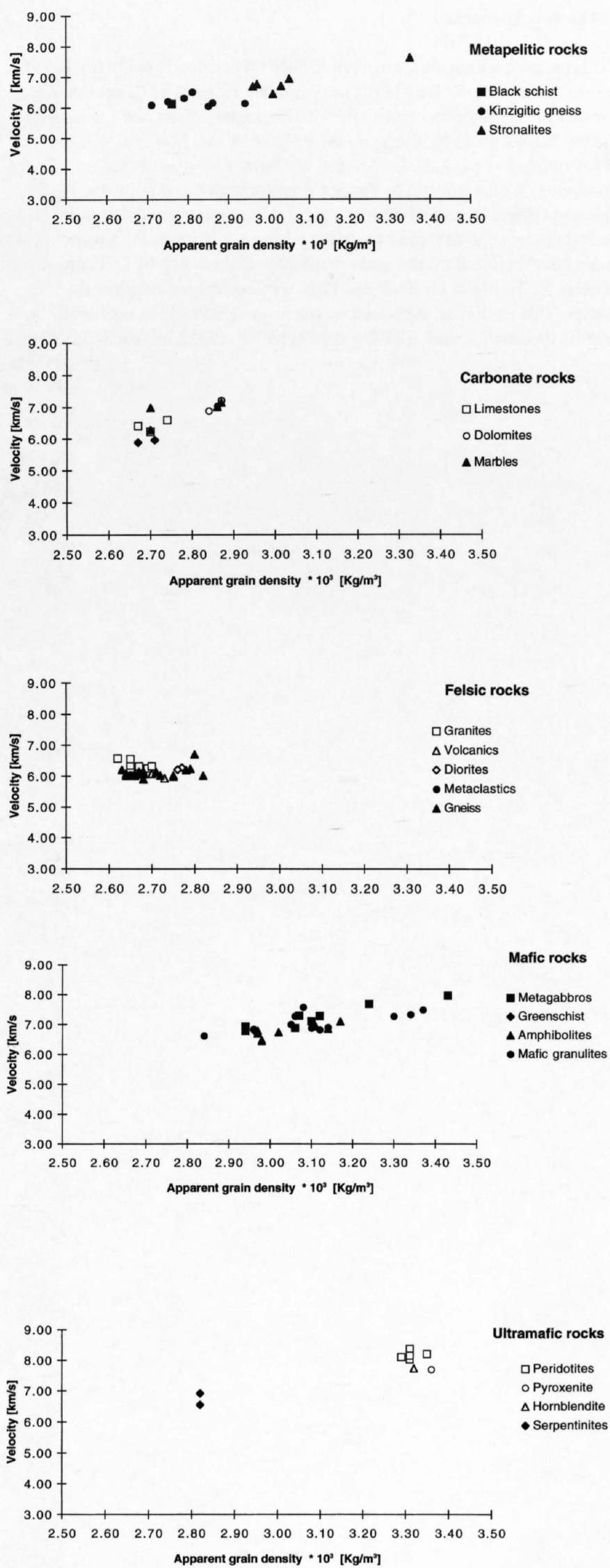
Figure 6-5
P-wave velocity at 400 MPa versus apparent grain (matrix) density.
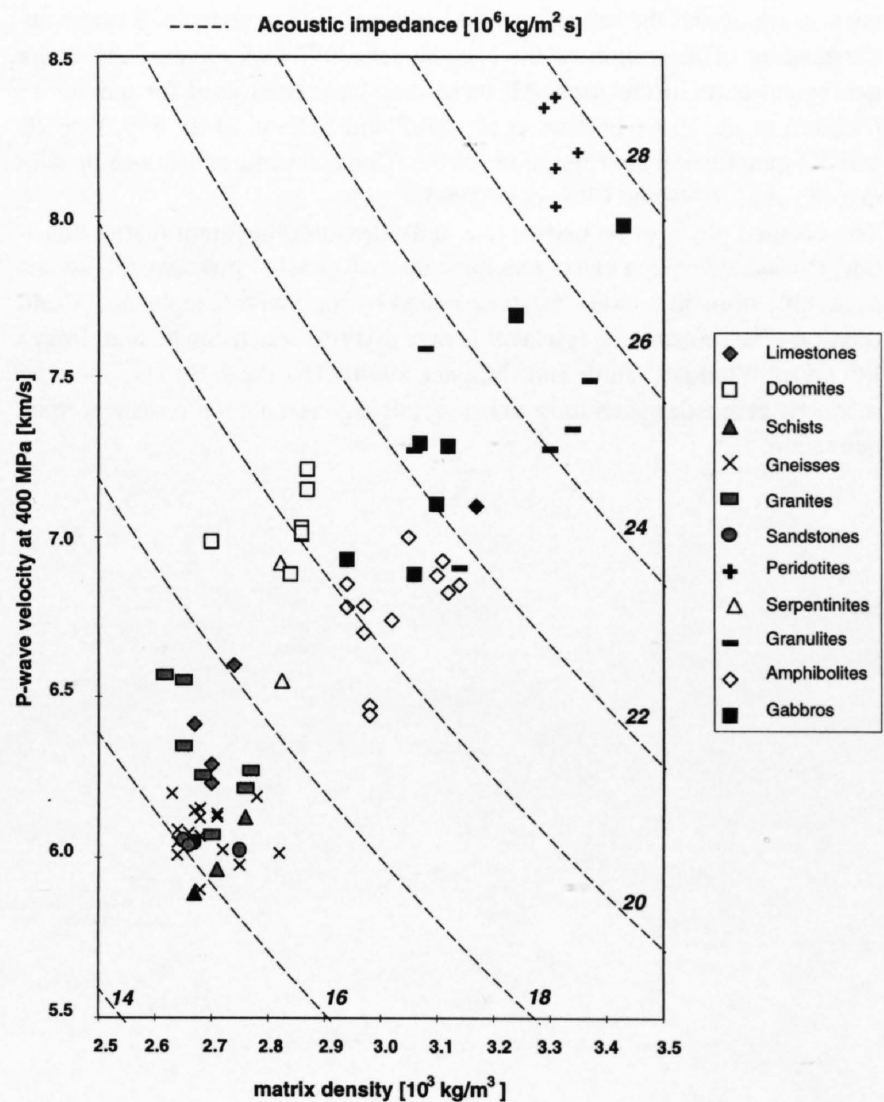

Figure 6-6
Average P-wave velocity at 400 Mpa versus apparent matrix density of samples from the NRP 20. The dotted curves are isolines of acoustic impedance.

Acoustic impedance

Acoustic impedance, which is the product of velocity and density, is an important parameter in reflectivity analyses. Under the acquisition conditions of NRP 20 seismic profiles, a reflection coefficient of 0.05 is considered sufficient to record a reflection between different geological units (Jones & Nur, 1982, Hurich & Smithson, 1987). This in turn implies a minimum acoustic impedance contrast of 2×10^6 kg/m²s (Sellami 1994). These data can be applied to the study of geological units from the upper crust down to the cover-basement interface. The range of pressure up to 400 MPa corresponds to depths up to 12 km. At these depths, considering that the temperature should not exceed 400°C and the fact that we compare adjacent units, the velocity variations due to the temperature should not have a significant influence.

The ultramafic rocks show very little change of acoustic impedance with depth. For all other rock classes, we can take into account the increase of impedance with depth by looking at the data at 400 MPa (see Table 6-1). The granitoids have low values, and the carbonate rocks have the least well-grouped impedance values, and naturally the highest values are obtained from the ultramafics. The values of iso-acoustic impedance have been superposed on a graph showing velocity versus density (see Figure 6-6). This graph enables one to read off the acoustic impedance of the different lithologies on the graph and to compare them directly with values of other lithologies. Thus impedance contrasts between juxtaposed geologic units can be evaluated readily. Using these graphs and by a careful study of the NRP 20 seismic profiles and the rock property data base, reflections from contacts between or within geological units have been analyzed and lead in some instances to a refinement of the geological interpretation of the seismic data (Sellami et al. 1990, Sellami et al. 1993, Sellami 1994, Pfiffner et al. 1992 and Levato et al. 1994)

6.6 Conclusions

Due to outcrop conditions in the Alps, the NRP 20 project has provided a unique opportunity to carry out petrophysical studies in parallel with reflection seismic campaigns. The laboratory measurements have allowed the determination of dry bulk and apparent matrix densities, which lead to the evaluation of effective porosities. From the density estimates, effective porosities were determined and lie between 0 and 4%. The P-wave velocities, for pressures up to 400 MPa and under dry conditions, not only permit the analysis of velocity changes with depth, but also an estimation of velocity anisotropy. The mean velocities range from 4.90 to 7.83 km/s at 20 MPa and from 6.09 to 8.17 km/s at 400 MPa. Relationships between densities and velocities enable the evaluation of the acoustic impedance. By studying the geological

43

cross sections and the seismic profiles it is possible to arrive at a better understanding of the origin of the seismic reflectivity of some of the major geological units in the Alps. All these data have been used for qualitative (Sellami et al. 1990, Pfiffner et al. 1992 and Sellami et al. 1993) or 2D and 3D quantitative interpretations of the Alpine seismic reflections profiles (Levato et al. 1994 and Litak et al. 1993).

The detailed physical properties (i. e. bulk densities, apparent matrix densities, P-wave velocities under pressures up to 400 MPa) mentioned here, are accessible through a larger database edited by the Swiss Geophysical Commission. The information is available on a diskette which can be read from a PC under Windows (Jordi and Wagner 1994). The database also includes magnetic properties such as initial susceptibility and natural remanent magnetization.

7 Jura Mountains

7.1   Interpretation of seismic lines across the rhomb shaped Val de Ruz basin (internal Folded Jura)

A. Sommaruga & M. Burkhard

Contents

7.1.1   Introduction

In 1988, British Petroleum conducted a seismic survey in the canton Neuchâtel where a total of about 300 km of vibro-seismic (and dynamite in rugged topography) profiles were acquired (compare approximate seismic plan published by Swisspetrol 1992). In an agreement between BP, the canton Neuchâtel and the Swiss National Science Foundation, part of this seismic survey from the Val de Ruz area has been obtained for research. These lines permit to extend our knowledge of the local stratigraphy, particularly for thicknesses of layers older than Dogger. Furthermore, for the first time in the central Jura, seismic data permit to constrain the geometry of this fold and thrust belt at depth.

The Val de Ruz is located within the internal part of the central Jura fold and thrust belt (Figure 7.1-1). Among the various cross sections studied by the NRP 20 project, these sections represent the most external parts of the Alpine thrust system. In this context it has to be mentioned that the overall tectonic picture of a cross section through the Alps in Western Switzerland is quite different from Eastern Switzerland, where the "alpine deformation front" is located within the internal part of the Molasse Basin, crossed by an industry section obtained in exchange with the NRP 20 program (Stäuble & Pfiffner 1991). In comparison with this eastern transsect, the "alpine deformation front" in central and western Switzerland is located in a much more external position, beyond the folded and thrust Jura chains (Laubscher 1972; Burkhard 1990). The transition from "undeformed foreland" to shortened cover is located mostly in France and has not been crossed by any of the NRP 20 lines. The French ECORS line from the southwestern termination of the Jura (Damotte et al. 1990; Guellec et al. 1990) is one of the few published seismic sections across the entire Jura. Other seismic profiles from the Jura have become available through NAGRA studies (Laubscher 1985; Noack 1989; Naef & Diebold 1990; Diebold et al. 1991) and small sections published by Bitterli (1972), Suter (1978) and Jordi (1990).

The study area (see Figure 7.1-1) is bordered to the south by lake Neuchâtel, representing the transition between the rather strongly folded Jura chain to the NNW and the very weakly folded/ faulted Molasse Basin to the SSE. Surface geology is quite well known from a series of published 1:25'000 maps of the Geological Atlas of Switzerland and innumerable original 1:5'000 map sheets deposited at the Institut de Géologie at Neuchâtel. Outcropping Mesozoic strata range from uppermost Liassic (strongly tectonized in the Vue des Alpes strike slip zone) to middle Cretaceous. The Mesozoic series are dominated by interlayered marls and limestones. The structural backbone of the characteristic Jura folds is formed by up to 400 m pure gray Malm limestones. This is the major competent formation within the Mesozoic se-
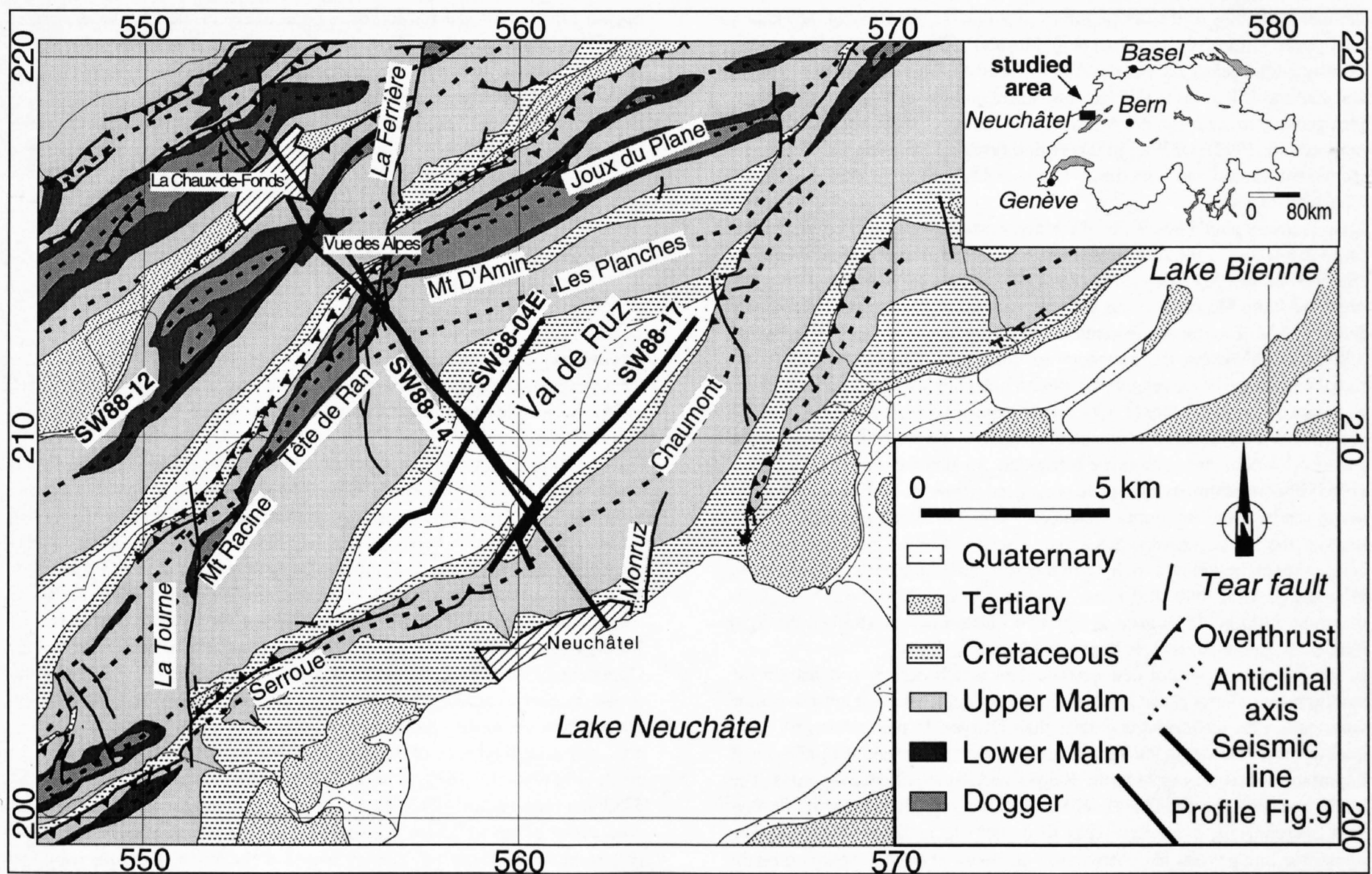

Figure 7.1-1
Structural map of the Val de Ruz area, according to geologic maps 1:25'000 Val de Ruz (Bourquin et al. 1968), Neuchâtel (Frei et al. 1974) and Bienne (Schär et al. 1971). Thick lines represent the approximate position of seismic lines. Major structural elements are labeled. Coordinates are according to the Swiss reference grid.